USE OF THE MARS ATMOSPHERE TO IMPROVE THE PERFORMANCE OF SUPERSONIC RETROPROPULSION

A Thesis
Presented to
The Academic Faculty

by

Keir Gonyea

In Partial Fulfillment
of the Requirements for the Degree
Doctor of Philosophy in the
Daniel Guggenheim School of Aerospace Engineering

Georgia Institute of Technology
August 2017

USE OF THE MARS ATMOSPHERE TO IMPROVE THE PERFORMANCE OF SUPERSONIC RETROPROPULSION

Approved by:

Dr. Robert D. Braun, Advisor
Daniel Guggenheim School of
Aerospace Engineering
Georgia Institute of Technology

Dr. Jechiel I. Jagoda
Daniel Guggenheim School of
Aerospace Engineering
Georgia Institute of Technology

Dr. Brian J. German
Daniel Guggenheim School of
Aerospace Engineering
Georgia Institute of Technology

Dr. Jerry M. Seitzman
Daniel Guggenheim School of
Aerospace Engineering
Georgia Institute of Technology

Dr. Aaron H. Auslender
Hypersonic Airbreathing Propulsion
Branch
NASA Langley Research Center

Date Approved: May 8, 2017

ACKNOWLEDGEMENTS

TABLE OF CONTENTS

LIST OF TABLES

LIST OF FIGURES

NOMENCLATURE

SYMBOLS

α	Temperature preheat ratio	
β	Ballistic coefficient	$[kg/m^2]$
ϵ	Emissivity	
η	Burning rate exponent	
γ	Specific heat ratio	
A	Area	$[m^2]$
A_{inlet}	Inlet area	$[m^2]$
C_D	Coefficient of drag	
c_p	Specific heat at constant pressure	$[J/molK]$
c_T	Coefficient of thrust	
D	Vehicle diameter	[m]
d	Droplet initial diameter	[mm]
ER	Expansion ratio	
F_T	Thrust	$[N]$
G	Gibbs free energy	$[J/mol]$
h	Enthalpy	$[J/mol]$
I_{SP}	Specific impulse	$[s]$

K	Constant	
M	3rd body specie	
m	Mass	[kg]
MR	Mach ratio	
n	Number of moles	
OF	Oxidizer-to-fuel ratio (by mass)	
P	Pressure	$[atm]$
P_i	Partial pressure (for gasses) or fugacity (for condensed species	
PR	Pressure ratio	
Q	Integrated heat load	$[J/cm^2]$
q	Dynamic pressure	$[N/m^2]$
R	Universal gas constant	[J/molK]
S	Entropy	[J/molK]
T	Temperature	$[K]$
t	Burning time of a solid droplet	$[s]$
t	Time	[s]
T_{ratio}	Amount of fuel preheating	
TR	Temperature ratio	
V	Volume	$[m^3]$
X	Specie concentration	$[mol/m^3]$

C	Carbon
CO	Carbon monoxide
CO_2	Carbon dioxide
Mg	Magnesium
MgO	Magnesium oxide

SUPERSCRIPTS AND SUBSCRIPTS

0	Property at standard pressure
∞	Property of the freestream flow
c	Condensed phase specie
D	Drag
f	Property of the fuel
g	Gaseous phase specie
i	Property of individual specie
T	Property at a given temperature
a,b,c	Stoichiometric coefficient of constituent atomic gas
$comb$	Property at the engine combustor
eff	Scaled by the oxidizer-to-fuel ratio
eq	Property at equilibrium
$exit$	Property at the nozzle exit
$final$	Property and the end of the simulation

induction	Property at the induction point
initial	Property at the beginning of the simulation
inlet	Property at the engine inlet
ox	Property of the oxidizer
PS	Property of the post-shock region
ref	Property at reference conditions
stag	Property of the post-stagnation region
tot	Total property over all species
X,Y,Z	Constituent atomic gas
b	Property of burning droplet
e	Property on the Earth
prop	Property of the propellant

ACRONYMS

ABSRP	Atmospheric-breathing supersonic retropropulsion
CFD	Computational fluid dynamics
DGB	Disk-gap band parachute
DRA5	Design reference architecture 5.0
EDL	Entry, descent, and landing
EDL:SA	Entry, descent, and landing systems analysis
MDO	Multidisciplinary design optimization

MER Mars exploration rovers

MSL Mars science laboratory

NASA National Aeronautics and Space Administration

NASP National Aerospace Plane

POST Program to Optimize Simulated Trajectories

RCS Reaction control system

SRP Supersonic retropropulsion

SSTO Single stage to orbit

SUMMARY

NASA has landed seven vehicles on the surface of Mars using parachutes for supersonic descent. These parachutes are unsuited to future high mass missions due to inflation, drag, and aerothermodynamic complications. Supersonic retropropulsion, or thrusting in opposition to the vehicle velocity, is a candidate technology to replace supersonic parachutes, but is hindered by its large associated propellant mass. Atmospheric-breathing propulsion systems may reduce this mass constraint by ingesting oxidizer from the surrounding atmosphere. However, the Martian atmosphere, which is composed of primarily carbon dioxide, necessitates that metal fuels be used in order to combust the available oxidizer.

This thesis advances the state of the art of atmospheric-breathing supersonic retropropulsion (ABSRP) by providing the first exploration into the feasibility and potential performance of ABSRP as a technology solution for high-mass Mars missions. Specific advancements include the development of modeling methods and tools, the evaluation of conceptual ABSRP performance and sensitivities, and the formulation of vehicle concepts. Model development targeted components and subsystems most relevant to ABSRP in order to capture the necessary physics and provide a preliminary integrated vehicle simulation for future conceptual design efforts.

Models were developed to assess metal - CO_2 combustion performance and sensitivity to both the engine design and operating regime. These models include an equilibrium combustion simulation to evaluate engine efficiency, a finite-rate kinetics simulation to investigate the time-dependent phenomena, and a particle burning simulation to assess diffusion effects. Case studies are presented for ABSRP relevant

mixtures and conditions to predict propulsion performance of the ABSRP engine across a range of conditions and verify that reasonably sized combustion chambers can provide nearly complete combustion of the propellant.

The propulsion system results are integrated in an ABSRP vehicle model, which accounts for the variable engine thrust and efficiency across different flight regimes. Mass capture of the atmospheric oxidizer is also considered. This model is used to search the design space and determine the performance and sensitivity of multiple proposed ABSRP vehicle concepts relative to competing propulsive solutions. The investigation includes an assessment of feasible and unfeasible regions of the design space in addition to design trends for optimal configurations. Mass favorable vehicles of multiple architectures are compared to understand their relative performance in order to ultimately determine the potential applicability of atmospheric-breathing propulsion for Mars descent.

CHAPTER I

INTRODUCTION

1.1 Entry, Descent, and Landing

Entry, Descent, and Landing (EDL) is the sequence of events starting from when a spacecraft enters a planet's atmosphere and ending when it lands safely on the surface. The EDL sequence composes a small fraction of the total mission time-line but poses unique technical challenges that drive the mission requirements and design. Such requirements include sufficiently decelerating the spacecraft in order to land safely, dissipating the heat generated during entry, and landing within a desired target area. The combination of these constraints has led to a complex symphony of engineering technologies that, when combined, successfully execute the EDL sequence.

1.1.1 Mars Mission Architectures

Landing on Mars presents many unique challenges. The Martian atmosphere is much "thinner" than that of Earth, having a density of approximately one one-hundredth of the Earth's at sea level, yet is still "thick" enough to cause significant aerodynamic heating upon entry [1, 2, 3]. The EDL heating rates necessitate using a thermal protection system in the hypersonic flight regime, while the low atmospheric density requires large drag devices for sufficient deceleration during the supersonic and sub-sonic flight regimes. No single technology has been developed that simultaneously satisfies all of these requirements. As a result, a novel mission architecture has been created.

The United States has successfully landed seven vehicles on the surface of Mars: the Viking I and II landers (1976), Mars Pathfinder (1997), Mars Exploration Rovers

(MER) Spirit and Opportunity (2004), Phoenix (2008), and the Mars Science Laboratory (MSL) Curiosity Rover (2012). Technology development for the Viking mission spanned seven years and included an extensive ground and flight test program [4]. This program culminated in the design and qualification of a rigid, blunt-body aeroshell for hypersonic deceleration; a parachute for supersonic, transonic, and subsonic deceleration; and a subsonic retropropulsion system for terminal descent and landing. An artistic rendering of the system architecture is shown in Figure 1. The aeroshell dissipated the majority of the vehicle kinetic energy and was fitted with a thermal protection system to mitigate the aerothermal heating. Given the low density on Mars, the aeroshell diameter was not large enough to meet the required terminal descent initiation conditions. Therefore, a parachute was deployed supersonically to increase the vehicle drag area and aid in deceleration. The parachute deployment Mach number was limited by the combination of increasing dynamic pressure, more severe aerothermal heating, and complex inflation characteristics. Since parachutes of reasonable scale were unable to achieve sufficiently low touchdown velocities, the vehicle transitioned to a propulsive, terminal descent phase. This also allowed for greater control during landing.

Successive missions heavily leveraged the Viking heritage and made incremental improvements on the architecture [1]. The Mars Pathfinder mission added retrorockets to the end of the parachute phase as well as an airbag landing system that could tolerate much higher velocities at touchdown [6]. Mars Exploration Rovers improved upon Pathfinder by including horizontal velocity sensing and control during terminal descent and a strengthened airbag system [7]. Finally, the Mars Science Laboratory mission added a guided, lifting hypersonic entry in addition to the Sky Crane propulsive terminal descent system [8].

These missions contributed substantial improvements to the terminal descent, or subsonic, phases of flight while MSL also added significant capabilities to hypersonic

2

Figure 1: The Viking EDL sequence including rigid, blunt body aeroshell, supersonic parachute, and terminal retropropulsion [5].

entry. Incremental improvements of the supersonic decelerator system have also been made during the parachute development and qualification programs of successive missions [9, 10, 11, 12, 13]. However, all US Mars landers have continued to rely on the Viking disk-gap band parachute flown within the operational regime established by the initial qualification program.

1.1.2 High Mass Mars Missions

As the exploration of Mars progresses, further scientific progress will most likely require larger, higher fidelity instruments. This has been the case with all of the recent US missions. As illustrated in Table 1, with the exception of Phoenix, lander masses of the recent US Mars missions have been increasing dramatically. The National Aeronautics and Space Administration's (NASA) long term goals of sending humans to Mars will require at least another order of magnitude increase in landing capability with payloads of more than 10 metric tons (t).

Landing payloads heavier than 1 t poses a significant challenge since the EDL technologies required for these vehicles easily surpass their Viking-qualified limits. One

Table 1: Comparison of the EDL architectures for recent US Mars missions. (Adapted from [1] and updated using [8, 14])

	Pathfinder	MER	Phoenix	MSL
Lander Mass (t)	0.092	0.173	0.167	0.900
Entry Mass (t)	0.58	0.83	0.60	3.15
Ballistic Coefficient (kg/m^2)	63	94	70	145
Aeroshell Diameter (m)	2.65	2.65	2.65	4.50
Parachute Diameter (m)	12.5	14.0	11.7	21.3
Parachute Deployment Mach	1.6	1.8	1.6	1.8
Parachute Deployment Mach Limit	2.1	2.1	2.1	2.1

significant problem is that landing heavier payloads requires a drastic increase in the diameter of the supersonic parachute. Forces on this large of a canopy may exceed the capabilities of current materials. In addition, as the parachute size increases so does the required inflation time. For human class missions, inflation times for parachutes of relevant scale may not allow for sufficient deceleration prior to landing. Any attempt to increase the timeline for supersonic deceleration by increasing the parachute deployment Mach number is also limited by poor parachute drag performance, and even poorer inflation characteristics along with aerothermodynamic complications at high Mach numbers [15].

High mass missions are also plagued by the unfavorable scaling of mass to drag. This effect is captured by the ballistic coefficient, β. Presented in Eq. 1, the ballistic coefficient is defined by the vehicle mass, m, divided by the drag coefficient, C_D, and drag area, A_D.

$$\beta = \frac{m}{C_D A_D} \qquad (1)$$

Vehicles with larger payloads typically have larger ballistic coefficients. This is generally the case for the US Mars missions as seen in Table 1. Higher ballistic coefficient vehicles are less favorable, since they decelerate lower in the atmosphere

and allow for less timeline to execute the EDL sequence. As evidenced by Figure 2, MSL ($\beta = 145 \ kg/m^2$) is already close to the limit of supersonic parachute deployment conditions. High mass missions with substantially larger ballistic coefficients will have difficulty reaching this operational window which will require additional capabilities from the supersonic decelerator. Since the supersonic parachute deployment window is limited by material, drag, and inflation restrictions, it is necessary to investigate novel supersonic deceleration techniques in order to enable future high mass and human class missions to Mars.
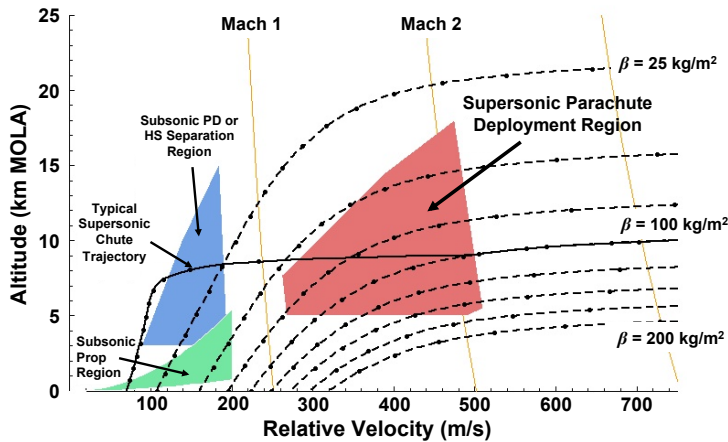
Figure 2: Graph of Mars entry trajectories for different ballistic coefficient vehicles along with limits for parachute and subsonic propulsion initiation. (Originally from [1], adapted in [16])

1.2 Supersonic Retropropulsion

One candidate technology to replace supersonic, aerodynamic deceleration (via parachutes or other deployable devices) is supersonic retropropulsion (SRP). SRP involves using thrust directed in opposition to the oncoming airflow in order to decelerate an entry vehicle while it is traveling at supersonic speeds. While SRP is affected by the scaling requirements that come with increasing payload masses, supersonic retropropulsion is attractive as a Mars descent solution because it is a technology solution that conceptually scales across a wide range of vehicle systems. A notional depiction of an

entry vehicle utilizing SRP is shown in Figure 3.
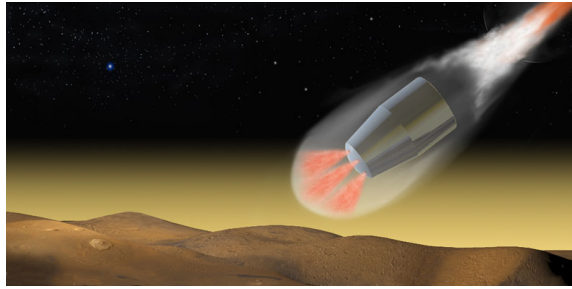
Figure 3: Notional picture of an entry vehicle utilizing SRP [17].

The presence of an SRP jet flowing into a supersonic freestream gives rise to a number of complicated phenomena [18]. For single jets with large thrust coefficients, the plume ends abruptly with a terminal shock, seen in Figure 4 [19, 20, 21]. SRP configurations with multiple nozzles will likely be required on future missions due to practical engine size constraints. Multiple nozzle configurations interact with the oncoming flow differently, "flattening out" the bow shock and even creating a larger effective vehicle area. The resulting structure of the SRP flowfield is, therefore, a function of the nozzle configuration and jet plume(s), and is also affected by the freestream velocity, composition, and jet pressure. Understanding these parameters and how they affect the overall vehicle performance is critical for the development of SRP and has been the subject of both experimental and numerical studies.
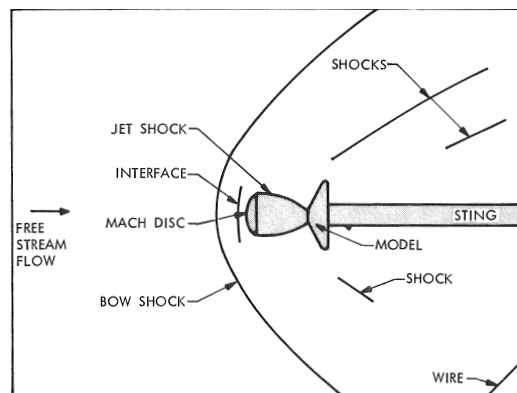
Figure 4: Diagram of a single-nozzle, high thrust SRP plume structure [22]

1.2.1 Supersonic Retropropulsion Experimental Testing and Performance Trends

SRP has been studied since the 1950's. During this time, subsonic and supersonic wind tunnel tests were conducted to understand how a counterflow jet would alter blunt body aerodynamics, surface pressure distribution, and flowfield stability [23, 24]. Overall results showed that the surface pressure and, as a result, aerodynamic drag on the vehicle tended to decrease with increasing jet pressure [25, 26, 27]. Testing continued throughout the 1960's and 1970's, since SRP, along with parachutes and inflatable aerodynamic decelerators, was one of the supersonic technology solutions considered for use on the Viking mission [28]. These test series explored a greater range of conditions, including freestream Mach numbers up to 6, both low and high levels of thrust, and the introduction of peripheral nozzles (shown in Figure 5) [22, 29]. The expanded test conditions and models allowed for an enhanced study of SRP drag preservation, flowfield structure and stability, and configurational effects.
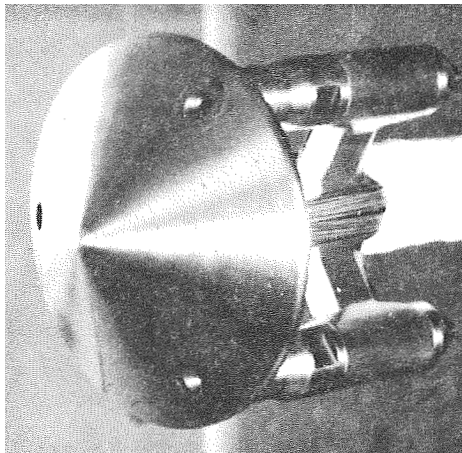
Figure 5: SRP test article with peripheral nozzle configuration [22]

It was determined during testing that many parameters were highly dependent on the nozzle thrust and freestream conditions. As a result, these parameters were non-dimensionalized into the thrust coefficient, c_T, defined in Eq. 2. In the equation F_T is the force due to thrust, q_∞ is the freestream dynamic pressure and A is the

drag reference area.

$$c_T = \frac{F_T}{q_\infty A_{ref}} \tag{2}$$

It was observed that the thrust coefficient was the dominant parameter governing drag preservation for SRP vehicles. For $c_T < 1$, a fraction of the no-jet drag was preserved, dependent on the c_T value [22, 30]. However, as c_T approached and exceeded 1, the vehicle deceleration was dominated by engine thrust, with little to no drag contribution [31, 22, 30].

Testing also revealed that the SRP nozzle configuration, including the number of nozzles, their location, and size, also had strong affect on the aerodynamic interactions. While all configurations experienced some amount of drag loss with increasing thrust coefficient, the magnitude of that loss varied significantly with the configuration. For vehicles with a single, central nozzle, the nozzle jet acted as a shield from the freestream flow, reducing drag. As seen in Figure 6(a), as the thrust was increased, this shielding effect likewise increased, resulting in no appreciable drag above $c_T = 0.8$ [32, 22, 30, 31]. This trend is substantially different for peripheral nozzle configurations, as evidenced in Figure 6(b). It was observed that the jet flow for these set-ups was swept outboard and aft of the entry vehicle and, as a result, low thrust coefficient tests preserved aerodynamic pressure inboard of the nozzles, resulting in a significant improvement in the drag coefficient [22, 30]. However, as the thrust was increased, the jet flow moved inward, decreasing the aerodynamic drag and, in some cases, even coalescing to mimic the single nozzle configuration [33].

The development work conducted during this time was foundational in maturing SRP and developed the fundamental understanding of supersonic retropropulsion flowfields and performance trends. In addition, these air-in-air wind tunnel tests also constituted a large dataset of SRP performance and characteristics covering a wide range of parameters. Once supersonic parachutes were chosen as the Viking decelerator system, research into supersonic retropropulsion halted and was largely
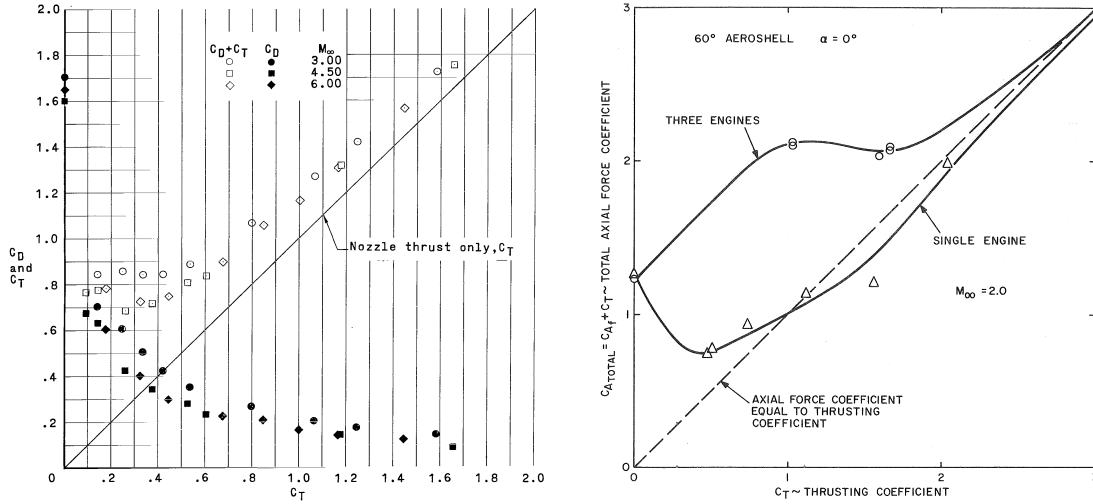
(a) Drag and total axial force as a function of thrust coefficient for an SRP configuration with a single, central nozzle [32]

(b) Total axial force coefficient as a function of thrust coefficient for an SRP configuration with three peripheral nozzles [22]

Figure 6: Comparison of drag preservation for one and three nozzle SRP configurations

abandoned throughout the next few decades.

SRP was revisited in the mid-2000's as a potential solution for high mass Mars missions. This involved an extensive test series to study the performance under relevant flight conditions with multiple configurations. The test article for this study, shown in Figure 7(a), featured the single, central nozzle and 3 peripheral nozzle configurations used during the pre-Viking testing along with an additional four nozzle configuration, a combination of the one and three nozzle models, also being investigated. Since a primary goal of the test series was also to provide data for numerical model validation, a number of test instrumentation methodologies were employed [34, 35]. This included high speed schlieren imaging, shown in Figure 7(b), along with static-pressure ports and high frequency pressure transducers.

Schlieren images from testing provided qualitative insights into the SRP flow structure and how it varied with nozzle configuration, thrust coefficient, pitch, and roll [37, 36, 35]. Central nozzle vehicles experienced the aforementioned reduction in aerodynamic pressure, with three nozzle configurations also confirming previous results.

9

(a) Picture of SRP test article and rig [36]
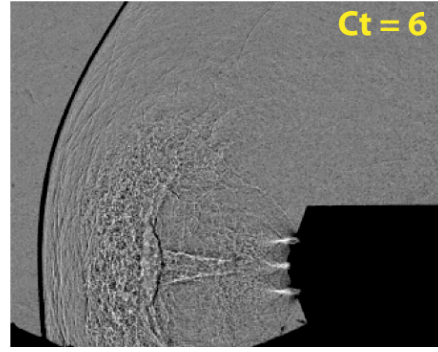
(b) High speed schlieren images of the SRP test [35]

Figure 7: SRP test article and instrumentation

The fourth nozzle was observed to improve flowfield stability at low thrust levels but also induced an abrupt transition to a highly unsteady flowfield at higher thrusts [37, 35]. These tests provided further insight into the impact of vehicle configuration and operating regime on SRP performance and stability.

1.2.2 Supersonic Retropropulsion Numerical Flowfield Modeling

Recent efforts have also supplemented experimental tests with numerical simulation. These simulations are valuable since, unlike experimentation where the conditions and model size are limited by the test facility, numerical studies can theoretically characterize any scale model at any desired condition, allowing for performance predictions at mission-relevant conditions and sizes. The majority of the recent numerical studies of SRP vehicles have involved computational fluid dynamics (CFD). In a CFD simulation, equations describing the fluid flow around a vehicle are discretized and solved to produce approximations of the flow conditions at each point. While early CFD simulations required significant approximation of the underlying physics, advances in computational performance have allowed for almost direct simulation of the governing Navier-Stokes equations, albeit at very modest Reynolds numbers.

Many early CFD simulations were performed assuming inviscid flow. Qualitative comparisons were made between the computational results and the Schlieren images

10

from testing to determine how well the inviscid CFD could predict the SRP flowfields. Overall, as shown in Figure 8, the simulations had success at capturing the locations of primary flow features including the bow and jet terminal shocks, the surface pressure distribution, and integrated force coefficients [38, 39, 18].
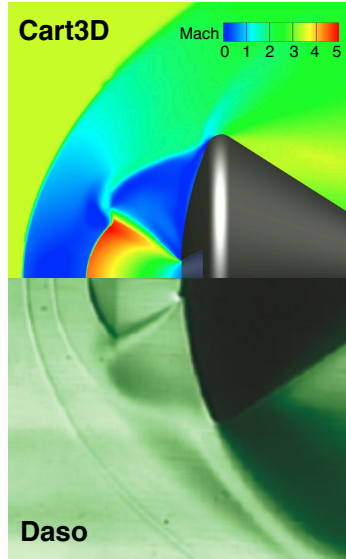
Figure 8: Comparison of CFD simulations (top) with test data (bottom) [39]

More recent studies have employed higher fidelity, viscous simulations in order to improve the prediction of SRP performance. Steady, or time averaged, simulations were able to better predict the flow structure and pressure trends across a range of configurations but estimated that a significant amount of unsteady behavior was likely being lost [18, 40, 41]. Time accurate solutions were also observed to successfully resolve the aerodynamic performance trends, in addition to highlighting the limitations of time-averaged solutions [42, 43]. However, the results of these solutions were found to be sensitive to the turbulence model assumptions. As a result, various simulations have been successful at capturing different aspects of the SRP flowfield but prediction of certain phenomena, such as the level of unsteadiness, has varied based on the selection and implementation of the turbulence model [44].

Overall, it was determined that CFD simulations were useful in predicting qualitative flow features such as the bow shock and plume structure, along with trends of axial and drag force as they varied with thrust coefficient and Mach number. Further work is continuing to be performed to improve the fidelity of the models in order to improve the prediction of SRP performance across the range of relevant conditions. Nevertheless, despite the discrepancies in the different CFD models, simulations have already been utilized to improve SRP wind tunnel test programs. Prior to the 2010 and 2011 experiments, CFD simulations were performed to inform the test designers about potential tunnel blockage and unstart conditions [45, 46]. Based on the simulation results, modifications were made to the test article in order to better simulate relevant conditions with minimal error due to the test facilities.

Analytical work has also been performed to aid in numerical simulation. Unlike CFD codes, which can take on the order of days to compute a single solution, analytical approximations can be computed exceedingly fast. Such methods have been developed to rapidly determine SRP plume shapes and can be used in conjunction with CFD simulations to help inform designers where to use coarse and fine gridding [47]. Implementation of both the analytical and numerical methods significantly reduce the design effort.

1.2.3   Novel Supersonic Retropropulsion Configuration Development

Numerical simulations have provide significant benefits by allowing for greater exploration of the entire design space at modest cost in order to find designs with favorable performance. In this spirit, preliminary exploration has been performed by conducting CFD analysis on a series of SRP designs with canted nozzles on the fore- or aftbody of the vehicle in order to determine whether or not they had the potential to decrease overall vehicle mass [48]. While SRP has been observed during testing to reduce entry vehicle drag for axially oriented nozzles (both central and peripheral, to

different extents), canted nozzles configurations were shown to retain more pressure on the vehicle forebody and, in some instances, achieve higher drag than vehicles without SRP.

(a) Effects of nozzle cant angle on the total axial force coefficient for forebody located nozzles

(b) Effects of nozzle cant angle on the total axial force coefficient for aftbody located nozzles
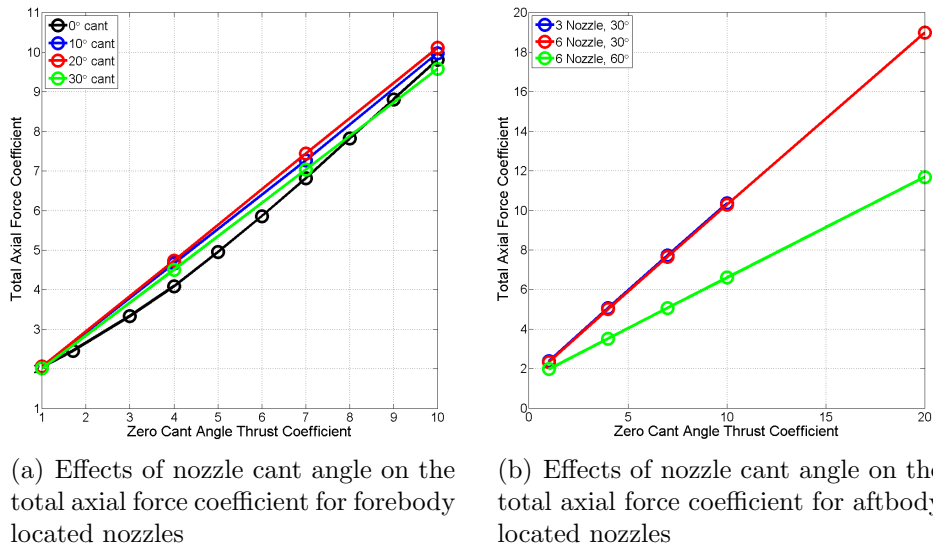
Figure 9: Effects of nozzle cant angle on the vehicle total axial force coefficients for fore- and aftbody nozzle configurations [48]

Vehicles employing low thrust, canted nozzles on the forebody yielded improved drag performance for cant angles up to 30°, in addition to improved stability characteristics. At higher thrust levels, larger cant angles preserved the majority of the surface pressure but experienced a net reduction in deceleration due to thrust vector cosine losses. Overall, as evidenced in Figure 9(a), nozzle configurations with moderate cant angles and thrust coefficients were seen to provide advantageous deceleration performance.

Aftbody nozzles at a 30° cant had a minimal effect on the bowshock and, as a result, improved forebody pressure, with the drag coefficient increasing slightly with higher thrust. Nozzles canted at 60° had no effect on the bowshock and improved stability but, because of the significant thrust vector cosine losses, had worse net deceleration performance than the 30° cant configurations. This effect is shownj in Figure 9(b).

13

The results of these studies demonstrate the potential for improved supersonic retropropulsion performance through novel configurations and designs. Further improvement is likely possible through continued exploration.

1.2.4 Supersonic Retropropulsion Technology Development Efforts

While the experimental and computational studies have contributed significantly to the maturation of SRP, further work is still necessary before it can be considered as a future supersonic deceleration solution. The importance of SRP's development was highlighted by its inclusion in the NASA Entry, Descent, and Landing roadmap, which discussed and prioritized NASA's various space technology activities [49].

SRP has been investigated in conjunction with various hypersonic decelerator technologies to land human and human-precursor scale payloads [50]. NASA has also been collaborating with SpaceX to collect data during the supersonic propulsive maneuver performed when recovering the launch vehicle first stage. SpaceX's previous recovery attempts were the first demonstrations of a rocket engine relight in an opposing supersonic freestream, answering a number of concerns regarding SRP's feasibility. The flight regime of the propulsive maneuver matches the supersonic conditions expected during a high-mass Mars SRP trajectory and provides valuable data for SRP performance characterization. Analysis of this dataset has significantly advanced SRP's technology readiness level [51, 52, 53, 54].

1.2.5 Supersonic Retropropulsion Integrated Performance Predictions

The attractiveness of supersonic retropropulsion lies in its potential applicability to a wide range of missions classes and, in particular, to human-scale payloads. Prior to conducting ambitious and costly development programs, conducting systems studies are an invaluable way to explore the utility of SRP technology for different missions and to determine what, if any, improvements are necessary, along with identifying new applications of this technology to improve current EDL capabilities.

A preliminary study conducted by NASA on human mission architectures, the human exploration of Mars Design Reference Architecture 5.0 (DRA5), proposed the use of SRP for supersonic and subsonic deceleration [55]. This architecture employed a mid lift-to-drag aeroshell for aerocapture and hypersonic deceleration followed by SRP initiation at approximately Mach 2 for both supersonic deceleration and landing. While a fully propulsive entry required too much propellant mass, supersonic propulsive initiation was considered to be more feasible than relying on aerodynamic deceleration.

The follow-on study to DRA5, the Entry Descent and Landing Systems Analysis (EDL:SA), reiterated the importance of SRP for enabling high-mass Mars missions [15]. As seen in Figure 10, half of the architectures considered involved the use of SRP (architectures 1 - 4), with all of the vehicles employing retropropulsion for terminal descent. Of the eight architectures, the configurations involving SRP were estimated to have higher expected safety and low complexity; however, they were generally found to be less mass efficient. Similar architecture studies also confirmed SRP configurations to generally require more mass, but provide favorable reliability [56, 57]. The EDL:SA study was extended to investigate the technological requirements to successfully land a precursor-size payload of 2-4 t [58, 59]. SRP was found to be a critical enabler of both the exploration and precursor missions. As a result, the study emphasized the definition of SRP performance requirements and the development of a reference SRP configuration.

Additional research has been performed to investigate supplemental benefits and applications of SRP:

- Extending divert capabilities of subsonic propulsion systems into the supersonic regime for improved performance and reduced mass penalty [60, 61]

- Modulating drag to account for atmospheric or other uncertainties [62]
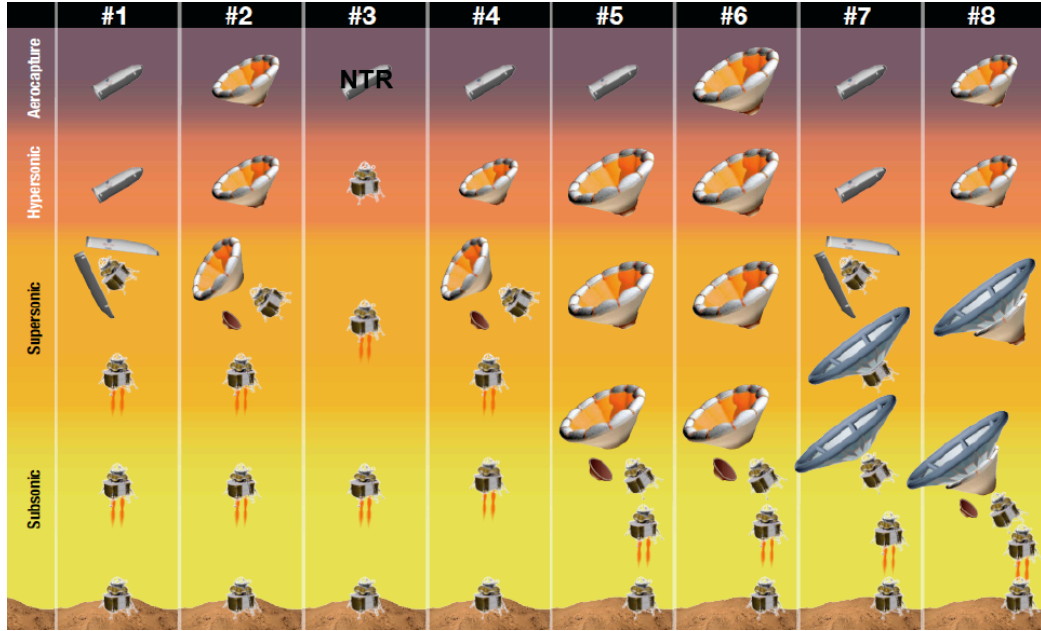
Figure 10: EDL:SA high-mass mission architectures. Systems 1 - 4 employ supersonic retropropulsion. (From [15])

- Exhausting into the freestream to mitigate aerodynamic heating [62]

- Recovering launch vehicle stages [63]

The simulation methodologies and assumptions used in SRP-related studies are also valuable and are extensible for predicting the performance and applicability of other propulsive vehicles, as is subsequently performed in this thesis. Two such investigations, one extending heritage Viking and Apollo technologies and the other evaluating SRP-exclusive architectures, performed trade-studies to estimate SRP performance for large-mass missions [64, 65]. In these studies, the SRP propulsion system sizing accounted for both engine and propellant mass. The engine mass was parametrically defined based on the SRP thrust and the propellant usage was calculated assuming a gravity turn descent. Optimization of the propulsion initiation was performed to minimize the total propulsion system mass, balancing an early initiation, which required a longer duration burn and higher propellant usage with a late initiation, which required higher decelerative thrust and a heavier engine. The studies also

added additional constraints, such as aerodynamic heating limits, to mimic realistic mission considerations. Overall, SRP was observed to scale favorably with larger mass vehicles, compensating for reduced aerodynamic deceleration, and also offered more control over the trajectory to satisfy the external constraints.

Other SRP specific studies have been conducted that have evaluated the technology for both human and MSL-class payload applications [66, 16]. Simulations utilized parametric models for the vehicle mass and volume, and included an additional drag model to account for forebody pressure reduction due to the propulsive interactions. The study was composed of two main efforts. The first component calculated the maximum allowable thrust, which was determined from multi-objective optimization designed to reduce both the propulsion system mass and volume. The second determined mass optimal SRP trajectories. These trajectories were found to decelerate at as low an altitude as possible and initiate SRP as late as possible, constrained by the maximum engine thrust. In this way, the trajectories were best able to maximize the benefits of both aerodynamic and propulsive deceleration. In all cases, attempts to preserve drag proved negligible as the thrust levels were well beyond drag preservation limits.

Supersonic retropropulsion clearly shows promise as a candidate technology for high mass Mars missions. Most designs, however, suffer from propellant masses that severely limit overall performance, with practical constraints such as g-loading and thrust-to-weight considerations further restrict their capabilities. Technical solutions that are able to reduce the required propellant mass and exploit thrusting earlier in the timeline have the potential to significantly improve SRP's applicability to high mass missions.

1.3   Airbreathing Propulsion

A possible approach to reduce SRP propellant mass is the use of an "air-breathing" (or in this case atmospheric-breathing) propulsion system. An atmospheric-breathing propulsion system, unlike a conventional rocket propulsion system, does not carry the oxidizer within the craft. It instead ingests the oxidizer from the surrounding atmosphere and combines it with the fuel carried onboard to create thrust. Because the oxidizer is not carried within the vehicle, this significantly reduces the mass requirements of the entry system. This efficiency is illustrated in the significantly higher I_{SP} of atmospheric-breathing propulsion systems relative to rocket propulsion systems over the range of applicable Mach numbers, shown in Figure 11. In the case of a Mars lander, this oxidizer would have to be carried throughout the entirety of the mission (from launch or Earth departure until Mars descent); as such, its elimination from the vehicle results in a significant performance advantage.
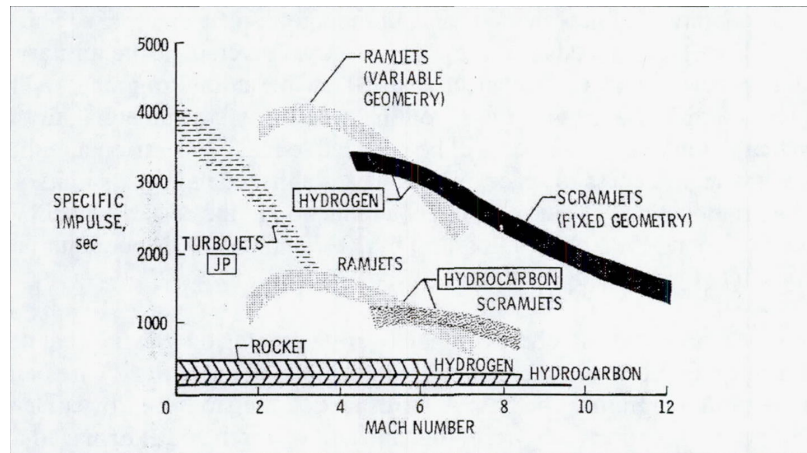
Figure 11: I_{SP} values of various propulsion systems with respect to Mach number (from [67]).

1.3.1   Airbreathing Propulsion Cycles

Airbreathing retropropulsion vehicles will be expected to operate over a wide range of flight regimes, decelerating from high-supersonic velocities to subsonic or even terminal conditions. This wide range of Mach number and altitude environments

present significant challenges for propulsion system design since the efficiency of the different propulsion cycles is highly dependent on the vehicle operating regime.

As shown in Figure 11, efficient flight in the relevant SRP environment (at rest through approximately Mach 3) is best achieved with a turbojet. The primary components of a turbojet are shown in Figure 12(a), composed of an inlet, compressor, combustion chamber, turbine, and exhaust. Space vehicles, which are extremely mass constrained, cannot afford to integrate heavy rotating machinery such as a multi-stage compressor or turbine. Also, high mach number initiation, which is beneficial for a retropropulsion system, presents significant complications for axial compressors due to the severe aeroheating.
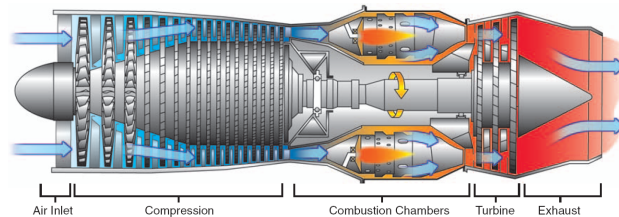
(a) Diagram of a turbojet engine with primary components [68]
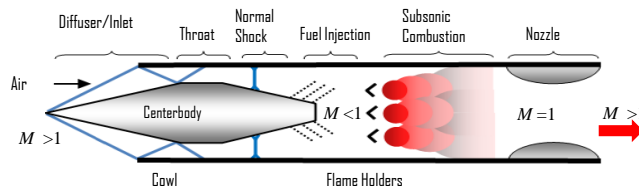
(b) Diagram of a ramjet engine (from [69])

Figure 12: Propulsion system diagrams for turbojet and ramjet engines.

For these reasons, the retropropulsion system will likely utilize many aspects of high-speed ramjet engines, shown in Figure 12(b) [70]. Unlike low-speed propulsion cycles, ramjets have no (or minimal) moving parts and instead compress the supersonic freestream air through the use of oblique shocks and inlet compression. The differences in propulsion flowpath allow ramjets to effectively operate up to approximately $M = 6$.
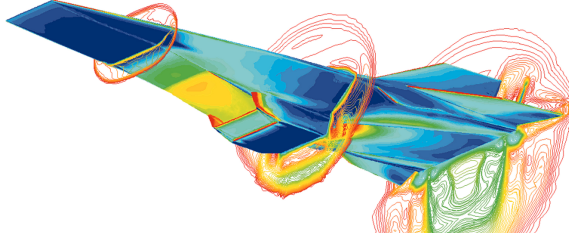
Figure 13: Depiction of a high-speed propulsion vehicle with an air-frame integrated engine [71]

Engine integration is also a significant problem for high-speed propulsion systems in order to satisfy drag, shock heating, and oxidizer mass capture requirements. As a result, modern vehicles utilize an airframe-integrated engine design where the entire under surface of the vehicle provides both an aerodynamic and a propulsive function. As shown in Figure 13, the underside of the vehicle prior to the engine doubles as the propulsion system inlet, compressing air and allowing for more air capture, while the aftbody surface acts as a propulsion system nozzle, expanding the flow to produce thrust. Due to packaging and heating constraints, airframe-integrated engines will be critical components of an atmospheric-breathing supersonic retropropulsion system. The additional requirements of low subsonic to high supersonic performance, low mass, and complex flowpaths mean that a viable engine will likely integrate a number of other concepts such as combined inlet and on-board compression, and subsonic combustion.

1.3.2   Airframe-Integrated Engine Development

Airframe-integrated propulsion systems have been studied for over three decades and are a part of the NASA Space Technology Roadmap [70, 72]. Most early vehicle development was achieved through analytical and experimental studies with recent advances in computation allowing for the proliferation of higher fidelity numerical models [73, 74]. Given the considerable expense and technical challenges, only a limited number of flight tests have been performed. Nevertheless, the ensemble of

airframe-integrated propulsion system development efforts has significantly advanced the understanding of the technology in addition to elucidated future challenges that need to be overcome.

1.3.2.1 Airframe-Integrated Engine Development Programs

An early airframe-integrated engine vehicle development was with the joint NASA and Department of Defense National Aerospace Plane (NASP) program, lasting from 1984 through 1995. The NASP program envisioned an airbreathing launch vehicle, shown in Figure 14, with single-stage-to-orbit (SSTO) capabilities and commercial aircraft cost and flexibility [75]. As depicted in the drawing, the NASP vehicle was designed to incorporate an airframe integrated engine, which would use the forbody of the vehicle as a compression ramp, allowing for enhanced air capture and potentially avoiding the significant problems of engine drag and shock interactions. Simultaneously, research into many other critical technologies was conducted. These included high temperature materials, active cooling of the vehicle leading edges, high-speed propulsion performance, and engine integration [76]. Despite the large combined effort and significant advancement of a wide range of technologies, due to cost requirements and unresolved technical challenges, the X-30 flight vehicle was never realized [70].

Figure 14: The NASP launch vehicle concept (from [70]).

The NASP follow-on effort in 1996, the Hyper-X program, proposed a scaled-down airframe integrated dual-mode scramjet vehicle (the X-43, shown in Figure 15) that was successfully flight tested in 2004 [77]. Prior to the flight tests, the Hyper-X team

employed a variety of analysis tools including CFD and analytical methods to predict the system performance [78]. An extensive wind tunnel test campaign was also conducted to investigate the engine integration, vehicle aerodynamic, propulsion system fuel sequencing, and thrust performance using hydrogen fuel. The flight test portion of the Hyper-X program was intended to demonstrate high-speed combustion with an engine integrated propulsion system. The flight test sequence involved dropping the X-43 vehicle from a B-52, boosting it to the test point by a Pegasus rocket 1st stage, separating the flight vehicle and the launch vehicle stack, and finally operating in autonomous flight [77]. While the vehicle combusted hydrogen fuel, a pyrophoric silane mixture was first used for reliable ignition. The first test in 2001 failed due to a problem with the Pegasus booster rocket. However, the 2004 second and third tests at $M = 7$ and $M = 10$ were successful. The Hyper-X program was the first successful flight of an airframe integrated scramjet with a realistic flightpath and provided valuable flight data on high-speed propulsive, aerodynamic, thermal, and structural performance.
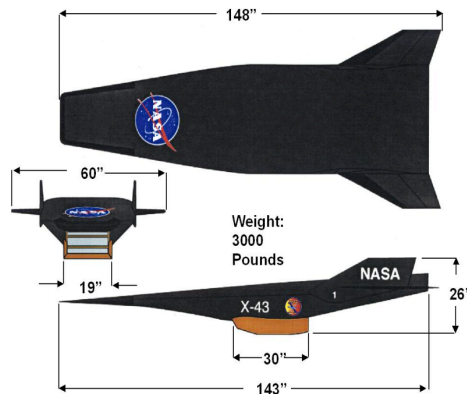
Figure 15: Diagram of X-43 flight test vehicle geometry (from [77]).

Recently, the X-51 WaveRider program demonstrated sustained, accelerating flight [79, 80, 81]. Like the X-43 vehicle, the X-51 (depicted in Figure 16) featured an airframe integrated engine but instead combusted endothermic hydrocarbon fuel. Preflight testing was conducted at a number of wind tunnel facilities to assess the vehicle

integrated performance. Wind tunnel testing was supported by structural ground testing along with conceptual and detailed CFD and finite element analysis studies [81]. The flight test profile was similar to that of the X-43, with the vehicle dropped from a B-52 and boosted to the test point [80]. The X-51 flights were notable in that they achieved sustained propulsion lasting almost 4 minutes while accelerating. In addition, the X-51 was ignited with an ethylene mixture and powered by hydrocarbon JP-7 fuel, which may be more applicable to future vehicles. Of the four flight tests, the first (2010), second (2011), and third (2012) tests experienced vehicle anomalies and were only partially successful or unsuccessful. The fourth test (2013) was a complete success, achieving combustion for 210 seconds and accelerating from $M = 4.8$ to $M = 5.1$ [82].
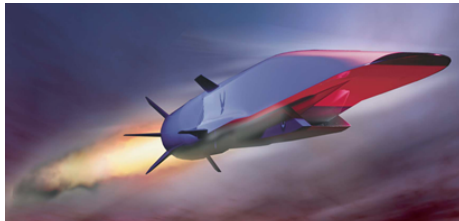
Figure 16: The X-51 WaveRider flight vehicle (from [82]).

Despite the program successes, there are a number of remaining challenges with airframe-integrated propulsion systems, including improved design methodologies for engine-airframe integration and 3-dimensional flowpath design [70]. Most importantly, however, these propulsion technologies require more flight tests to fully explore and mature the systems.

1.3.2.2 Airframe-Integrated Engine Computational Development Methods

CFD has emerged as a powerful tool for propulsion analysis since it can perform large parametric studies with a short response time. However, CFD also has applications well beyond early-stage conceptual studies, being involved in both component and integrated vehicle design [83]. Computational modeling of airframe-integrated

propulsion systems presents many challenges because, in addition to accounting for the complex aerodynamic phenomena such as turbulence and transition, simulations need to also model gas reaction kinetics with several orders of magnitude variation in time scales [84, 85]. Directly simulating all of the phenomena is computationally intractable, with research still being performed on turbulence and kinetics modeling. As a result, CFD codes trade off simulation fidelity with computational time in order to best compliment the different phases of design. Early conceptual modeling has involved Euler or Reynolds Averaged Navier-Stokes simulations, while later-stage detailed analysis may involve the more accurate Large Eddy Simulation codes [74]. In each of these models, various assumptions are made regarding the gas thermodynamics, kinetics, and reaction mechanism models either to reduce computational expense or improve fidelity.

Multidisciplinary design optimization (MDO) is also becoming increasingly important for airframe-integrated propulsion vehicle design. Given the highly integrated nature of these vehicles, the structural, aerodynamic, and propulsive performance are all sensitive to design decisions made by the other disciplines. As a result, optimization is difficult and requires an integrated design process. A number of MDO tools have been developed to aid in vehicle design by coordinating coupled aerodynamic, structural, thermal, and propulsive design tools [86]. In addition, since many vehicle surfaces have dual aerodynamic and propulsive applications, integrated propulsion system vehicles also require careful accounting of performance characteristics during the different operational modes [87].

1.4 Metal - CO_2 Combustion

One significant issue with airbreathing propulsion on Mars is that the Mars atmosphere consists primarily of carbon dioxide (CO_2) and does not contain high levels of

oxygen like on Earth. As a result, traditional oxygen based combustion is not possible. Instead, innovative propulsion techniques need to be assessed and developed that allow for combustion using CO_2 as the oxidizer.

1.4.1 Fuel Selection

Despite the fact that carbon dioxide has a very low enthalpy compared to traditional oxidizers, and thus has a correspondingly low oxidizer potential, it has been known to combust with certain metal fuels; namely, beryllium, magnesium, aluminum, and lithium. In these cases, the condensed metal oxide has a lower enthalpy than the carbon dioxide, allowing for positive net heat release. A number of potential combustion mixtures have been identified in the literature and theoretical and experimental studies have been conducted to evaluate their overall feasibility for propulsion.

1.4.1.1 Equilibrium

One of the most important characteristics of a propellant mixture is its specific impulse, or I_{SP}. The specific impulse is a measure of the combustion system's propulsive efficiency relating the thrust produced to the propellant consumed, as defined in Eq. 3. In this equation, F_T denotes the thrust, $\dot{m}_{prop}$ denotes the propellant mass flowrate, and g_e denotes the acceleration due to gravity at the Earth's surface.

$$I_{SP} = \frac{F_T}{\dot{m}_{prop}g_e} \tag{3}$$

Literature studies typically calculate the I_{SP} values of different propellants as a function of the oxidizer to fuel, or OF, ratio. While high I_{SP} values are important, the OF value at peak I_{SP} (approximately corresponding to the stoichiometric mixture point) can also be used to differentiate between fuel candidates since higher OF mixtures leverage more of the atmospheric oxidizer and, as a result, require less propellant.

Theoretical I_{SP} calculations, shown in Figure 17, yield that beryllium is the highest performing fuel when combined with CO_2 as the oxidizer, having an I_{SP} of 260 s,
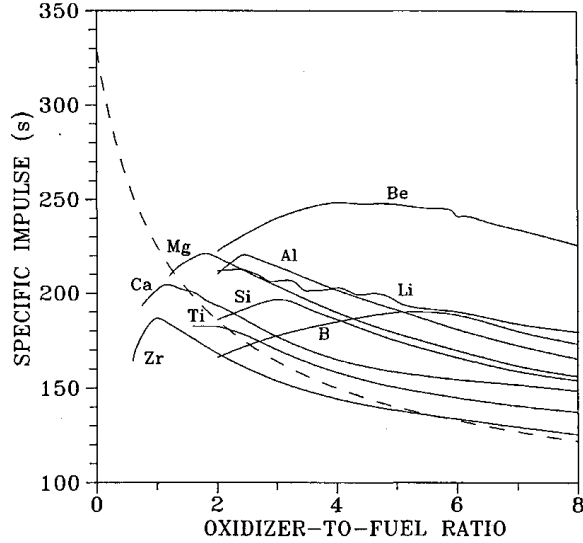
Figure 17: Specific impulse of a carbon dioxide - metal fuel engine as a function of the oxidizer-to-fuel ratio, by mass [88].

with lithium, magnesium, aluminum, and silicon second best, each having I_{SP} values around 200 s [88].

Of those four fuels, lithium had a lower overall peak I_{SP}, but better performance at high OF ratios. Other studies found silane and boron to also be attractive fuels [89, 90]. Attempts to increase performance by adding metal hydrides have had mixed results, beryllium hydride experienced improved I_{SP} over pure beryllium but with decreasing gains for higher OF ratios; whereas, all magnesium hydrides decreased I_{SP} performance. Despite its superior maximum I_{SP}, none of the investigations recommended the use of beryllium, in part due to its high toxicity. Also, lithium, aluminum, magnesium, and silicon have been shown to have better combustion temperatures and condensed phase mass fractions, both important systems considerations for actual engine application [88].

1.4.1.2 Kinetics

Specific impulse isn't the only parameter that defines a favorable fuel mixture. Theoretical I_{SP} calculations typically assume that the combustion system is in equilibrium, a state that requires infinite time to reach. The validity of this assumption varies

26

among different mixtures based on their kinetics, or how fast they approach equilibrium. As a result, the mixture combustion kinetics are another important factor in their propulsion potential, with poor kinetics nullifying any desirable I_{SP} properties.

Early experiments investigated the kinetics of various fuel candidates by heating a metal fuel specimen to a designated temperature and then exposing the sample to a carbon dioxide stream to observe burning [90]. Of the four candidate fuels, magnesium was shown to have superior kinetics, rapidly burning at many different initial temperatures. Lithium also exhibited combustion, but at much slower rates. Of the remaining two fuels, aluminum was able to react when preheated above 2000 °C and boron would not ignite. In all successful cases, the primary products were the metal oxide condensate and carbon monoxide.

Later studies investigated the combustion kinetics of magnesium and aluminum fuels by injecting metal particles into a carbon dioxide stream. It was observed that magnesium particles would ignite in carbon dioxide at 1000-1100 K while aluminum particles required ignition temperatures to be upwards of 2000-2500 K [89]. In these cases, the high aluminum temperatures caused a surface condensate to form, hindering further reactions. Experiments on lithium and silicon likewise demonstrated that they have poor ignition and combustion kinetics [88]. Aluminum combustion could be significantly improved however, by the addition of nickel or iron coatings on the particles. The coatings reduced ignition temperatures to 1600-1700 K and also prevented the formation of an aluminum oxide coating.

1.4.1.3   Recommendations

As a result of its favorable equilibrium and superior kinetics performance, magnesium was recommended by the majority of studies as the most promising fuel for burning with carbon dioxide. At OF ratios by mass of 4-6, it achieved an I_{SP} of 190-170 s, combustion temperatures of 2388-1845 K, and equilibrium condensed phase mass

fractions of 0.33-0.24 [88]. In addition, with the possible exception of aluminum, magnesium is by far the most tested carbon dioxide fuel and has the largest available open-literature database [89].

1.4.2 Metal - CO_2 Burning Rates

Achieving the maximum obtainable theoretical equilibrium I_{SP} performance requires, in part, that complete combustion is achieved. The early kinetics tests investigated the ignitability of different fuels in carbon dioxide, but usually did not present specific information on combustion rates. Since chemical reaction data is typically provided for molecules in the gaseous state, of particular importance for mixtures involving solid particles is the droplet burning rate, or how fast is a solid particle completely consumed. This rate is typically represented by the time required for the solid droplet diameter to shrink from its initial diameter to zero, described by Eq. 4. In this equation, t_b is the burning time, K_b is the burning rate constant (typically determined experimentally), d is the initial droplet diameter, and η is the burning rate exponent (η is 2 for most systems).

$$t_b = K_b d^\eta \tag{4}$$

The droplet burning process and corresponding burning rate law involve complex interactions between the fuel and oxidizer thermodynamics, chemical kinetics, and transport properties. As a result, experimental studies are one of the most reliable measurements since they simultaneously capture all relevant phenomena. Note that numerical simulations which simplify the governing physics have also had success in predicting the burning rate [91].

1.4.2.1 Experimental Studies

A number of experimental investigations have been conducted to study the detailed phenomena of solid metal fuels burning in carbon dioxide. A simple way to isolate the droplet burning process is to levitate a single metal particle and ignite it with a laser.

Such experiments have been performed using magnesium and aluminum particles to determine their burning time, ignition delay, and ignition temperature [92]. Confirming the qualitative results of previous studies, the ignition delay of magnesium was determined to be around two orders of magnitude faster than that of aluminum, and the magnesium burning time was also five to eight times faster for equally sized particles. Burning rate law exponents were calculated at $\eta = 0.6$ for magnesium and $\eta = 1.5$ for aluminum. Burning of magnesium particles in a spherical bomb has provided insight into the rate discrepancies. It was observed that, unlike aluminum, the gas phase reactions of magnesium particles produced a positive pressure gradient which broke apart the formation of any solid oxide shell that would hinder combustion [88]. The absence of the oxide shell also allowed for complete combustion of the particles, which helped magnesium better achieve theoretical efficiency. Burning rates calculated during the experiments observed that $t_b = 0.25d^{2.7}$ (in mm and s).

Other experiments conducted on magnesium droplets in a reduced gravity, carbon dioxide environment observed a rate law exponent $\eta = 2$, better correlating with theoretical predictions [93]. Burning rates for experiments repeated in normal gravity were twice as fast, demonstrating that the reactions were likely diffusion controlled. The diffusion limiting was also observed in levitated particle burning studies conducted at various pressures [94]. This study also calculated a burning rate law of the form $t_b = K_b d^2$ with a burning rate constant of $K_b = 0.5$ s/mm^2. Magnesium - carbon dioxide kinetics were observed to be insensitive to pressure variation and various other studies have demonstrated the ability to sustain combustion even at low pressures, similar to what would be expected on Mars [89].

While single particle experiments are important for understanding the underlying phenomena of metal - carbon dioxide combustion, they simplify many of the complications involved with metal-fuel propulsion. In particular, sustained burning in a cloud of particles introduces the challenges of fuel-oxidizer mixing and temperature

diffusion. Studies attempting to propagate a flame in a cloud of magnesium particles had varying degrees of success [95]. Flame propagation through a flame tube was successful for slightly lean mixtures, with flame speed estimates approaching 1 m/s, demonstrating that combustion with metal particles is possible. However, flames were not observed to propagate for moderately lean mixtures. The lean limit for the flame tube experiment was observed to be restricted by settling and non-ideal suspension effects. Alternate experiments that attempted to stabilize a powdered magnesium - carbon dioxide flame above a Bunsen burner were also unsuccessful, with the flame exhibiting blow-off in every trial. Theoretical calculations of the Mg - CO_2 mixtures predicted a flame speed of 30 cm/s, which was within the requirements for flame stabilization with the Bunsen burner. It was expected that settling and mixing effects near the Bunsen burner exit caused locally lean pockets that disrupted propagation and caused blow-off.

1.4.2.2   Numerical Studies

Numerical simulations, while relying on simplified models, present a valuable way to study combustion performance across a range of conditions and understand the sensitivities to various parameters. Based on observations from previous experimentation, a two-part reaction mechanism involving magnesium (Mg), carbon dioxide (CO_2), magnesium oxide (MgO), carbon monoxide (CO), and carbon (C) was proposed [88]. Eq. 5a was assumed to occur away from the droplet with the CO mass transfer to the particle surface fueling the surface reaction Eq. 5b. In the equations, a subscript g denotes a gaseous specie while a subscript c denotes a condensed phase.

$$Mg_g + CO_{2,g} \leftrightarrow MgO_c + CO_g \tag{5a}$$

$$Mg_c + CO_g \leftrightarrow MgO_c + C_c \tag{5b}$$
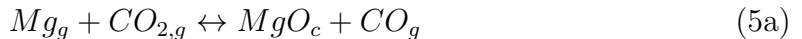
The proposed mechanism simulated diffusion (of CO to the surface) limited burning, which was justified based on observations from previous experiments. However,

30

droplet burning dynamics are likely to be bounded by purely diffusion and purely kinetics limits. To understand this issue, a model was developed which could simulate the full range of diffusion limited to kinetics limited cases [91]. The variation was achieved by parametrically varying the rate of the surface reaction (Eq. 5b) between the previous model value (transport limited) to 0 (kinetics limited). Burning rates for the limiting cases were determine to be $t_b = 0.83d^2$ for transport limited surface reactions and $t_b = 3.08d^2$ for no surface reactions (in s, mm). Quasi-steady and transient models of magnesium droplet burning have also been developed, which detail the temperature and species profiles as a function of time and radial distance [96].

1.4.3 Engine Design and Testing

Following validation of the theoretical fuel and oxidizer performance through both equilibrium and kinetics evaluations, the final step in determining the actual mixture performance is through realistic engine and subsystem design. Similar to the previous steps, this can be carried out using both numerical and experimental models. Many of the early problems with metal - carbon dioxide combustion were identified through numerical investigations. Proposed ideas were evaluated through experimental subsystem testing followed by full engine testing to verify overall system performance.

1.4.3.1 Numerical Studies

The applications of metal - carbon dioxide combustion have always been directed towards propulsion on Mars, which has a predominantly carbon dioxide atmosphere. However, propulsion in the Mars atmosphere present additional challenges since it is also exceedingly "thin", having a density and pressure orders of magnitude lower than on Earth. The low density means that engines are starved for oxidizer, producing less thrust, while the low pressure forces nozzles to incorporate excessive expansion ratios to maximize efficiency. The combination of these factors mean that any engine design will need to balance high thrust performance with high fuel consumption and

large inlets and nozzles [89]. Trade-offs between the thrust and fuel consumption can also be achieved by varying engine parameters such as the combustion pressure and temperature [90].

Additional challenges with metal combustion is the formation of condensed phase products, which can drastically reduce engine performance. This can occur either through the formation of large particles, which induce non-equilibrium effects in the expanding nozzle, or by product condensation on the walls, which can disrupt engine flow and potentially cause clogging [95]. The use of small fuel particles and homogenous combustion can deter the formation of larger products and the injection of a CO_2 stream along the nozzle has been proposed to mitigate against wall condensation.

1.4.3.2 Subsystem Testing

The majority of subsystem testing has involved developing reliable injection and mixing mechanisms. An initial injection design involved flowing inert nitrogen gas through fine magnesium powder in order to transport the fuel to the combustion chamber [97]. The addition of the inert gas degraded the combustion performance but was able to reliably deliver the fuel against gravity and through 90° angles in the feed pipes. The inert gas carrier also provided flow control through variation of the gas feed pressure.

The injection mechanism involved an axially flowing carbon dioxide stream with the magnesium fuel being added from the side into a cross flow. This system was found to produce sufficient mixing with minimal clogging and significant heat release within the combustor. Other injection designs have been discussed such as the use of a similar carrier gas setup with the addition of a pneumatic porous piston [89]. Instead of modulating the flow with the gas pressure, the piston could potentially offer greater control over the fuel feed rate. An additional ball valve was also proposed to enable restart and throttling.

1.4.3.3 Full Engine Testing

Full engine tests, shown in Figure 18, have successfully demonstrated the operation of a magnesium - carbon dioxide fueled rocket engine [97]. Using the nitrogen carrier gas and crossflow injection method discussion in section 1.4.3.2, the Mg - CO_2 engine was able to light and thrust for a duration of 3 s. However, attempts to relight the engine failed due to carbon formation that developed on the ignitor electrode. While the engine did not achieve mission relevant thrust levels, producing an average of 180 N, it demonstrated the reliable and sustained operation of a metal fuel combustion system.

Other efforts have also successfully achieved sustained Mg - CO_2 combustion [98]. This engine used an alternative injection mechanism in which powdered magnesium was forced by a piston into a carbon dioxide stream flowing above the fuel tank. Combustion was sustained for a duration of 10 s and produced 35 N force. Operation was also demonstrated across a range of oxidizer-to-fuel ratios from 0.7:1 (CO_2 to Mg, by mass) up to 4:1, in the regime of interest of a Mars propulsion system. Post testing inspection found residual condensed phase particles in the engine but the higher mixture ratio, mission applicable test cases found fewer solid particles. An injection mechanism involving a co-flow of both fuel and oxidizer was proposed to further reduce condensed phase buildup. Overall, the results were positive, with the majority of problems arising due to the solid fuel injection mechanism jamming.

Carbon dioxide engines using other fuels were also explored [98]. A liquid silane - liquid carbon dioxide engine was developed which produced 90 - 165 N thrust during 3 different 10 s firings. Sustained combustion was not achieved in a pure CO_2 environments, but was possible if the carbon dioxide was saturated with 5% oxygen. The largest problem with the liquid bi-propellant engine was the significant formation of condensed phase products, with buildup completely blocking the engine after the three test runs. Solid lithium fuel, which was melted prior to injection, was also
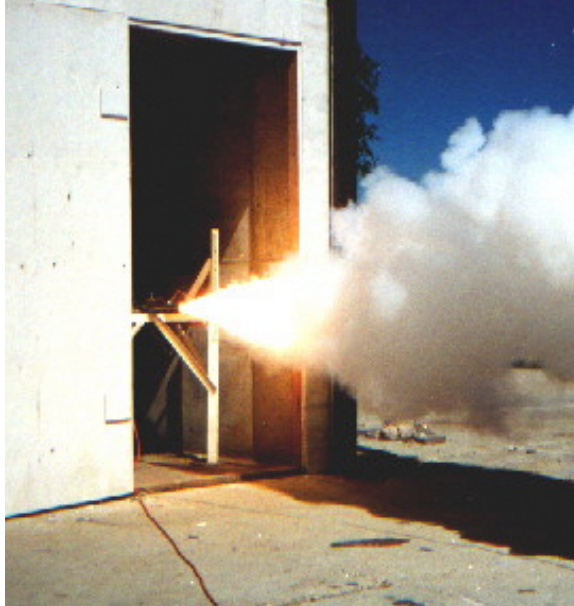
Figure 18: Test of a rocket engine using powdered magnesium fuel and carbon dioxide oxidizer [97].

successfully combusted. Like silane, the lithium - carbon dioxide engine experienced large amounts of condensed phase buildup. Lithium aluminum hydride was also considered due to its promising theoretical performance, which is much higher than that of magnesium. During simplified burning tests in a carbon dioxide environment, the lithium aluminum hydride demonstrated favorable ignition and heat release, but limitations in budget and schedule prevented full engine testing.

1.4.4 Observations

Overall, it can be seen that magnesium is one of the more promising fuels for burning in carbon dioxide and is supported by a significant amount of past work. Other fuels also show some promise. Aluminum and silane have both demonstrated favorable equilibrium performance but aluminum suffers from poor kinetics while silane has less available literature information.

Production of thrust in a metal - carbon dioxide rocket engine has also been shown to be feasible. These demonstrations have developed practical powdered fuel feed and injection systems, as well as overall engine designs and implementation

strategies. The primary issues observed included poor injector reliability and the formation of condensed phase products which impeded engine performance and long-duration testing.

1.5 Research Goals

1.5.1 Motivation

It is evident that future high mass robotic and human-class missions will require significant improvements in EDL capabilities which are not attainable with incremental advances of Viking heritage technology. Supersonic deceleration, in particular, requires significant advancement. Large ballistic coefficient vehicles will be unable to meet the required inflation conditions for supersonic parachutes and will not provide sufficient timeline for subsequent events.

Supersonic retropropulsion is a candidate technology to replace supersonic, aerodynamic deceleration via parachutes for high-mass missions. SRP conceptually scales across a wide range of mission classes, but large propellant mass requirements limit its overall performance. One possible solution to the propellant mass problem is the use of an atmospheric-breathing propulsion system. Atmospheric-breathing vehicles do not carry the oxidizer on-board and, as such, significantly reduce the mass requirements of the entry system. A significant issue with ingesting the oxidizer, however, is that the Martian atmosphere is primarily composed of carbon dioxide. As a result, innovative techniques need to be developed to allow for combustion using carbon dioxide.

The literature review reveals that atmospheric-breathing supersonic retropropulsion (ABSRP) vehicles have potential application to high-mass Mars missions. An ABSRP system would effectively integrate three technologies: supersonic retropropulsion, airframe-integrated atmospheric-breathing propulsion, and carbon-dioxide combustion. Given that no previous studies have attempted to combine the three areas,

a performance evaluation of a potential vehicle is unavailable. This includes propulsion performance in a relevant flight regime as well as system performance during the EDL sequence. These studies are critical in order to fully characterize EDL architectures utilizing atmospheric-breathing supersonic retropropulsion. Future maturation of the technology will also require understanding of the ABSRP design space, relevant constraints on the design parameters, and favorable vehicle characteristics.

1.5.2 Summary of Contributions

This thesis advances the state of the art of atmospheric-breathing supersonic retropropulsion by providing a set of conceptual design tools and analyses for the evaluation of ABSRP performance. Specific contributions are made in the following areas.

Evaluation of solid magnesium - carbon dioxide combustion performance across a range of relevant flight conditions and engine designs. A number of studies have investigated Mg - CO_2 performance with applications to Mars surface vehicles. However, performance data for propulsion systems in the wide range of ABSRP-relevant environments is noticeably lacking. Problems have also been observed with the ability of commercially available software to simulate mixtures containing condensed phase species, often exhibiting poor and inconsistent convergence. As a result, there is a deficiency of tools available to assess Mg - CO_2 combustion performance under varying environmental or combustion conditions. Such a methodology would have use in propellant comparison studies or as a contributing analysis to multidisciplinary system evaluations. Evaluations of the time dependent performance of the Mg - CO_2 mixtures is likewise lacking, with limited data available studying significantly different ambient environments. This thesis develops a suite of tools and analyses in order to assess Mg - CO_2 propulsion system performance and sensitivity to both the engine design and flight regime. These tools include an equilibrium combustion simulation to evaluate engine efficiency, which features improved convergence

algorithms for condensed phase species, and a finite-rate kinetics simulation to evaluate the time-dependent performance of solid magnesium - carbon dioxide mixtures. Case studies are presented for solid magnesium - carbon dioxide mixtures in environments relevant to atmospheric-breathing propulsion on Mars. A particle burning simulation is also adapted to relevant combustion conditions in order to assess the effects of the kinetic and diffusive timescales on the burning process. The combination of these tools allow for the evaluation of thrust performance of an ABSRP engine across a range of conditions and the analyses verify that reasonably sized combustion chambers can provide complete combustion of the propellant.

Development of conceptual analysis methodologies to evaluate vehicle performance for ABSRP architectures and assessment of the ABSRP vehicle design space. Vehicle trajectory simulations exist for analyzing planetary entry and descent, involving deceleration via a rigid aeroshell, supersonic parachute or retropropulsion, and subsonic terminal descent. The majority of these simulations assume a constant engine efficiency because traditional rocket propulsion is only weakly influenced by atmospheric conditions. This is not the case for atmospheric-breathing systems, the cycle efficiency and thrust performance of which are a strong function of external conditions. This thesis develops the methodology for a full EDL simulation, which accounts for the unique aspects of atmospheric-breathing propulsion vehicles, such as variable engine thrust and efficiency across different flight regimes, in order to analyze atmospheric-breathing propulsion vehicle performance. Mass capture of the atmospheric oxidizer is also considered. Multiple architectures are assessed with varying degrees of reliance on atmospheric-breathing propulsion to allow for vehicle design trades. A reference architecture simulation utilizing traditional rocket engines is also developed to serve as a comparison. The methodology and resulting simulations enable assessment of ABSRP vehicle performance over a wide range of vehicle designs and across multiple architectures.

Until the writing of this thesis, no conceptual analysis of ABSRP vehicles for Mars has been conducted. In this thesis, investigations are conducted to determine relevant constraints on the multidimensional vehicle design space and to understand the required performance of various subsystems in order to enable a closed system design. In a similar manner, the performance of different configurations are analyzed to understand the sensitivity to design decisions and to infer the characteristics of optimal vehicles. The mass characteristics of each vehicle are assessed to determine trends, enabling an understanding of the dominant components and characteristic mass fractions. Finally, comparisons are made between architectures in order to determine whether or not the application of atmospheric-breathing propulsion presents vehicle performance benefits and the degree of the improvement. This contribution ultimately allows for the assessment of ABSRP viability as a technology solution for human-class Mars missions.

CHAPTER II

PROPULSION SYSTEM PERFORMANCE CHARACTERIZATION

2.1 Introduction

As mentioned in Section 1.4, one of the main challenges with using an atmospheric-breathing supersonic retropropulsion system on Mars is that the Martian atmosphere consists largely of carbon dioxide, not air. Thus, traditional oxygen combustion is not possible. Instead, innovative combustion techniques need to be assessed and developed that allow for combustion using CO_2 as an oxidizer. Magnesium is the most popular fuel for burning in CO_2 due to its high I_{SP} at high oxidizer-to-fuel ratios, allowing Mg - CO_2 engines to reduce on-board propellant mass [88, 89]. In addition, Mg combusts readily in CO_2 flows and has low proportions of condensed phase products, both of which are favorable for a reliable engine [90]. The initial feasibility of such propulsion systems have been demonstrated by the Wickman Spacecraft & Propulsion Company and Pioneer Aerospace, each having shown the production of thrust in a rocket engine that combusts solid magnesium powder with CO_2 [97, 98].

The capabilities of ABSRP engines and their potential for use as an EDL solution are investigated further in this section. This includes the characterization of Mg - CO_2 engine performance and an understanding of the combustion timescales in relevant flight environments and within a range of pertinent operating conditions.

2.2 Propulsion System Overview

A notional diagram of the ABSRP propulsion system is shown in Figure 19. In Stage 1 the post-shock atmospheric oxidizer is ingested by the reentry vehicle. The oxidizer

is then compressed in Stage 2 via inlet compression and, potentially, is augmented by an on-board compression system. The fuel (stored as a powdered solid in the fuel tank, item A) is mixed with the oxidizer in Stage 3. For this analysis, it is assumed that mixing is instantaneous and that a specific oxidizer-to-fuel ratio is maintained. The reactant mixture is combusted in Stage 4 and exhausts to the post-shock region in Stage 5. Item B defines the outer mold line of the reentry vehicle and is dependent on the propulsion system integration. Finally, it is assumed that the engine will run in steady state, combusting all of the oxidizer as soon as it is ingested. Subsequent analyses will consider whether or not it is advantageous to store the oxidizer before the ABSRP operation.
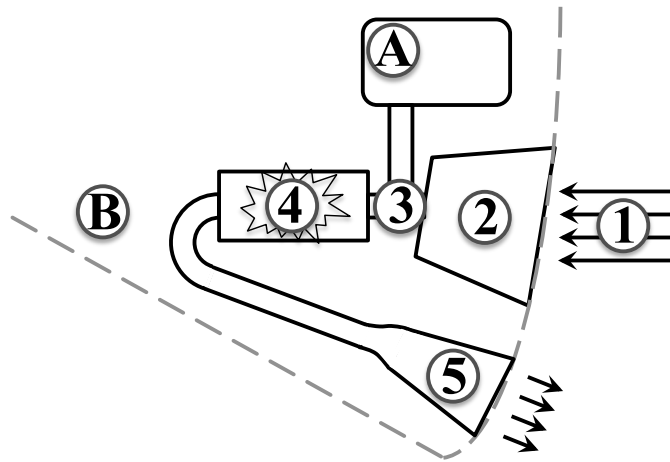
Figure 19: Diagram of the atmospheric-breathing supersonic retropropulsion system

2.3   Equilibrium Combustion Simulation

An equilibrium combustion simulation was written to calculate the ideal I_{SP} of a Mg - CO_2 engine. The I_{SP} values are an important metric to compare different engines and combustion parameters as well as to calculate the vehicle thrust in trajectory simulations.

2.3.1 Methodology

The I_{SP} of a rocket-class engine is defined by Eq. 6, where v_{exit} is the gas exit velocity and g_e is the acceleration due to gravity on Earth. The exit velocity can be calculated via Eq. 7 with h being the enthalpy of the mixture. Since the ABSRP engine is an atmospheric breathing engine, the I_{SP} value can be rescaled by the fuel-oxidizer ratio as in Eq. 8 to determine the effective I_{SP}, which accounts for the fact that the ABSRP vehicle does not carry its own oxidizer. $I_{SP,eff}$ values are a better metric to use when comparing against traditional approaches because they are solely based on the propellant carried onboard the vehicle.

$$I_{SP} = \frac{v_{exit}}{g_e} \tag{6}$$

$$v_{exit} = \sqrt{2(h_{T,mix} - h_{exit})} \tag{7}$$

$$I_{SP,eff} = I_{SP}(1 + OF) \tag{8}$$

The enthalpy values in Eq. 7 are obtained from the equilibrium combustion simulation, which models the propulsion system as a two-part process. Reactant species first flow through the combustor, which is modeled as an adiabatic, constant pressure process, before being exhausted out the engine nozzle, modeled as an isentropic expansion to the nozzle exit pressure. The inlet enthalpy is the mixture enthalpy prior to combustion (assuming zero mixture velocity), i.e. $h_{T,mix}$, and the exit enthalpy is the mixture enthalpy following expansion.

The equilibrium combustion simulation is a variant of the method developed by Huff, Gordon, and Morrell and is able to calculate the equilibrium composition and temperature of gas and condensed phase mixtures [99]. The method iteratively converges on the solution by enforcing the conservation equations. The gas phase species are assumed to behave according to the idea gas law, defined by Eq. 9, and the condensed phase species are assumed to have partial pressures of 0 and fugacity of 1.

In the subsequent equations P is pressure, n is number of moles, V is volume, R is the gas constant, and T is temperature.

$$P_{i,gas} = n_i \frac{RT}{V} \tag{9}$$

The modeling of a given reaction product created from its associated constituent gases is governed by Eq. 10 and the equilibrium condition for the partial pressures of the species is given by Eq. 11. For condensed phase species the P_i in Eq. 11 refers to its associated fugacity, which is 1. The equilibrium constant is obtained using Eq. 12. In these equations a and b are both the number of moles of constituent gases Z and Y, respectively, as well as the number of Z and Y atoms in the product molecule. Note that K_{eq} denotes the equilibrium constant and ΔG_T^0 is the difference in the Gibbs free energy between the product molecules and constituent gasses at the given temperature and standard pressure.

$$a_i Z + b_i Y + \ldots \rightarrow Z_{a_i} Y_{b_i} \ldots \tag{10}$$
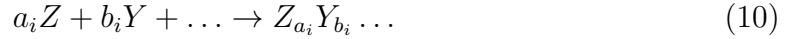
$$K_{eq,i} = \frac{P_i}{P_Z^{a_i} P_Y^{b_i} \ldots} \tag{11}$$

$$K_{eq,i} = e^{\frac{-\Delta G_T^0}{RT}} \tag{12}$$

The remaining constraints on the solution conserve mass, defined by Eq. 13, constrain the static pressure, defined by Eq. 14, and satisfy energy conservation, defined by Eq. 15. Equation 15 is replaced by a constant entropy condition for calculations modeling an isentropic expansion process, shown in Eq. 16. In these equations T_{ref} is a reference temperature, c_p is the specific heat at constant pressure, $h_{T_{ref}}$ is the enthalpy of formation, and S_T^0 is the entropy at standard pressure.

$$a_{prod} = \sum_{reac} a_i n_i \tag{13}$$

$$P = \sum P_i \tag{14}$$

$$\sum_{reac} n_i \left(\int_{T_{ref}}^{T} c_P dT + h_{T_{ref}} \right) = \sum_{prod} n_i \left(\int_{T_{ref}}^{T} c_P dT + h_{T_{ref}} \right) \tag{15}$$

$$\sum_{reac} n_i \left(S_T^0 - R \log(P_i) \right) = \sum_{prod} n_i \left(S_T^0 - R \log(P_i) \right) \tag{16}$$

Data for the thermodynamic properties of each species were obtained from NASA SP-3001 [100].

The presence of condensed phase species made the system of equations stiff and caused significant convergence problems. The original literature algorithm attempted to simultaneously converge upon the species, pressure, and enthalpy conditions (or entropy, in the case of the isentropic expansion simulation). For this study, to improve convergence, the system of equations was decomposed into two separate steps, initially fixing the temperature and then converging upon the mixture composition, and subsequently varying the temperature while holding the mixture composition constant. The composition is a unique function of the pressure and temperature, which enabled reliable convergence for the first step. In addition, the enthalpy is monotonic in temperature, so evaluations of the temperature in the later step could be bounded. In this manner, robust convergence was achieved for mixtures involving condensed phase species.

2.3.2 Validation

Previous studies have calculated the I_{SP} values of a Mg - CO_2 rocket-class engine to be used on Mars for a range of oxidizer-to-fuel ratios and serve as validation test cases [88, 89, 101]. These studies assumed combustion chamber and expansion pressures of 10 bar and 10 mbar, respectively, consistent with values for a Mars hopper or another surface vehicle. The reports do not mention the initial gas temperature for the calculations, which affects the I_{SP} results. An equilibrium simulation was developed to calculate the I_{SP} values for the specified pressures and a range of initial gas temperatures to evaluate which temperature best correlated with the literature

values. The results of the simulation, shown in Figure 20, present the calculated I_{SP} values for an initial temperature of 200 K. Of all the temperature values tested, 200 K best compares with the data reported in the literature. Note that the data generated in this study also compare well with those of past Mg - CO_2 engine studies.
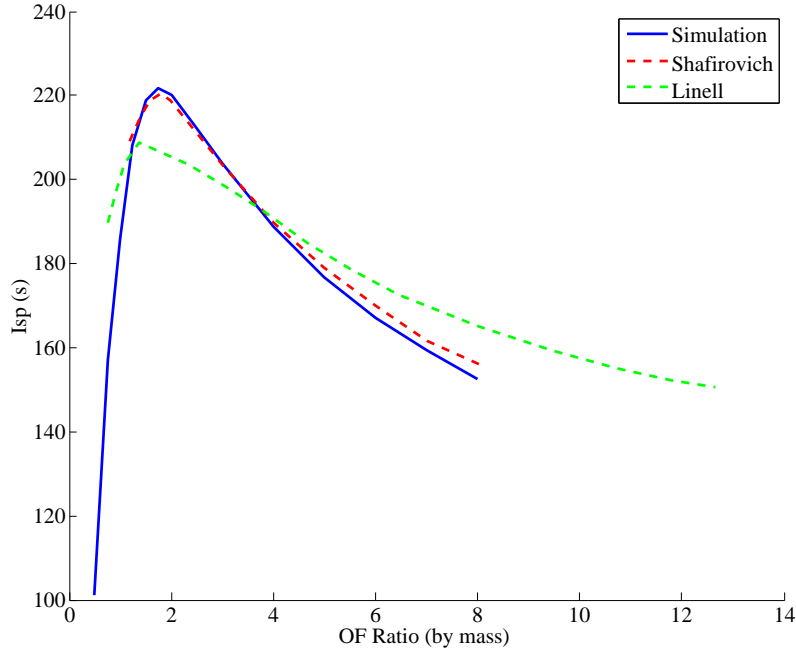
Figure 20: Validation of I_{SP} calculations with literature results. Curve shown for simulation using initial temperature of 200 K

2.3.3 Results

The atmospheric conditions from the literature, which focused primarily on surface vehicles, are significantly different to the conditions for an entry vehicle. Therefore, the equilibrium simulation was run for a range of pressures and temperatures to calculate the I_{SP} values in a relevant flight regime and to investigate where the AB-SRP engine would be effective. These results will serve as a comparison to traditional approaches and will be used in conjunction with trajectory simulations to design a propulsion system that minimizes the entry vehicle mass while still landing safely.

Two points were chosen on the Mars Science Laboratory trajectory (payload mass of 1 t) at M = 1 and M = 4 [102]. It was assumed that the freestream flow at these

points passed through a normal shock before being isentropically compressed on board [103, 104, 105]. Combustion occurred at the post-compression pressure and the mixture was expanded to the post-shock pressure. Two parameters were varied during the simulation, the isentropic compression pressure ratio and the fuel temperature preheating ratio. The pressure ratio, defined as $\frac{P_{comb}}{P_{inlet}}$, denotes the amount of compression and was varied from 1 to 100. The temperature ratio, defined as $\alpha = \frac{T_{f,2} - T_{f,1}}{T_{ax} - T_{f,1}}$, scales the temperature of the preheated fuel ($T_{f,2}$) between its storage temperature ($T_{f,1}$) when $\alpha = 0$ and the compressed oxidizer temperature (T_{ox}) when $\alpha = 1$. The composition was fixed at $OF = 4$ since the literature indicates this would balance the large heat release of a near-stoichiometric mixture with the reduced fuel consumption of a large oxidizer-to-fuel ratio mixture [88]. Oxidizer freestream and pre-ingestion states for the two trajectory points are shown in Table 2 and I_{SP} results are shown in Figure 21. A specific heat ratio of 1.3 was used for CO_2 in the normal shock calculations.

Table 2: Oxidizer state prior to isentropic compression for both trajectory points

	Trajectory Point 1 (M = 1)		Trajectory Point 2 (M = 4)	
	Freestream	Pre-Ingestion	Freestream	Pre-Ingestion
Altitude (km)	5.4		12.8	
Static Pressure (kPa)	0.43	0.43	0.22	3.96
Temperature (K)	236.7	236.7	221.3	751
Density (kg/m^3)	0.0094	0.0094	0.0051	0.0271
Velocity (m/s)	257	257	800	174

The reactants for the simulation were chosen to be pure Mg and CO_2. At altitudes relevant for a retropropulsion system, the Martian atmosphere is composed of 95% CO_2, 3% N_2, and 2% Ar [106, 2]. Therefore, at low vehicle velocities, the pure CO_2 assumption is reasonable. However, as the vehicle velocity increases, significant dissociation will occur behind the vehicle bow shock potentially leaving little to no CO_2 in the reactant species [107]. Dissociation effects are not modeled in this effort but can be added in future, higher fidelity analyses to understand sensitivities to

reactant composition.

As shown in Figure 21, the I_{SP} values are not sensitive to fuel preheating over the majority of the design space. As a result, complex systems to preheat the fuel are not necessary to improve the engine thrust. However, since the magnesium will be stored on board as a powdered solid, another reason for preheating the fuel would be to vaporize the particles. This would improve the combustion kinetics and drastically decrease the induction time before burning. The boiling point of magnesium is 1363 K. Assuming isentropic compression and perfect fuel preheating, this requires pressure ratios of 1633 and 12.5 for the M = 1 and M = 4 trajectory points, respectively. Other sources of heat may be available since the adiabatic flame temperature of representative Mg - CO_2 flames approaches 3000 K and the surface temperatures of entry vehicles will be in the 1000s of Kelvin.

The I_{SP} sensitivity to the compression ratio is expected because the difference in pressure between the combustion chamber and exit drives the increase in gas velocity. As displayed in both Figures 21(a) and 21(b), a pressure ratio of 5 is required before any appreciable I_{SP} is generated; whereas, a pressure ratio of 10 is required to achieve I_{SP} values that are significant. For the M = 1 trajectory point, the total pressure (maximum possible pressure from inlet compression) corresponds to a 1.8 compression ratio. For the M = 4 trajectory point, the freestream total pressure corresponds to a 10.8 pressure ratio and the post-shock total pressure corresponds to a 1.1 pressure ratio. This indicates that additional on-board compression will be required since inlet compression alone is not expected to provide a sufficient pressure rise. However, compression ratios above 10-to-1 result in a diminishing return on I_{SP}, with only 40% increase in I_{SP} for 900% increase in pressure ratio. The amount of compression necessary will be investigated later in this thesis.

The advantage of an airbreathing engine is shown in Figures 21(c) and 21(d). For an engine with an OF ratio of 4, the $I_{SP,eff}$ (based on fuel consumption) is 5 times
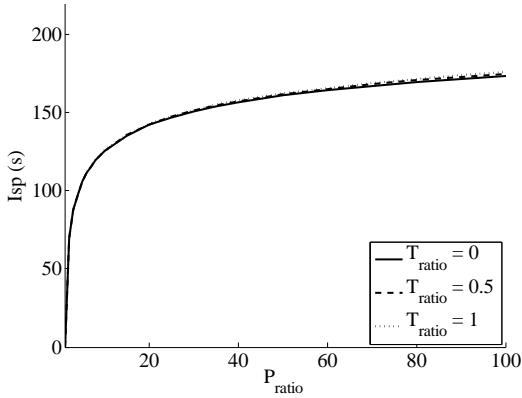
(a) I_{SP} values for the M = 1 trajectory point (s)
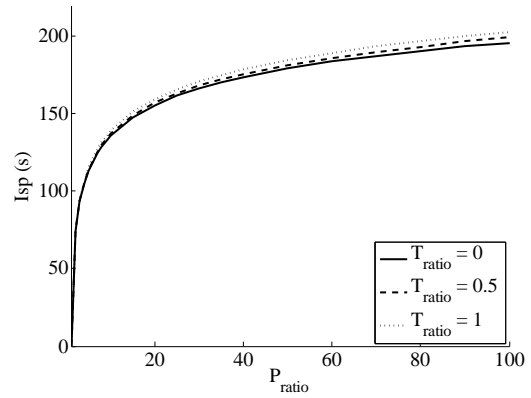
(b) I_{SP} values for the M = 4 trajectory point (s)
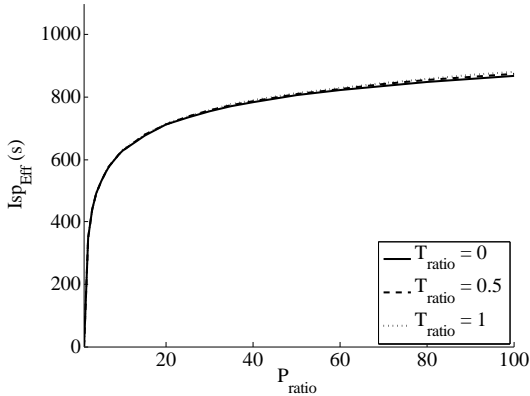
(c) I_{SP},eff values for the M = 1 trajectory point (s)
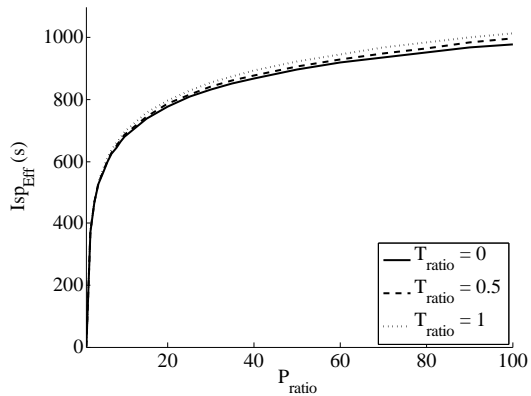
(d) $I_{SP,eff}$ values for the M = 4 trajectory point (s)

Figure 21: I_{SP} values (in seconds) for the M = 1 and 4 trajectory points as a function of isentropic compression pressure ratio and fuel temperature preheating ratio

greater than the I_{SP} value (based on total propellant usage). Therefore, while the I_{SP} of an ABSRP engine may only be 120 s, one third that of a typical SRP engine (I_{SP} of 370 s for a liquid oxygen, liquid methane engine), its I_{SP} based off of propellant consumption is 600 s, over one and a half times that of the SRP engine [108]. These results demonstrate that ABSRP has the potential to be a feasible component for large mass Mars missions.

The heat release from the magnesium oxide condensation is a significant contributor to the ideal propulsive efficiency of the engine calculated in the equilibrium combustion results. Excessive amounts of condensed phases can also contribute to

reduced engine performance, due to slag buildup and clogging concerns. Representative mixtures simulated at an OF ratio of 4 resulted in product compositions of 20-30% condensed phases. Literature studies have calculated condensed phase fractions ranging from 19% to 55% for OF ratios of 8 to 2, respectively. The impact of accommodating the condensed phase products, while outside the scope of the present work, will need to be addressed.

2.4 Finite-Rate Kinetics Simulation

A finite-rate kinetics simulation was developed to assess the kinetic timescales of the combusting mixture. This was necessary to inform the length of the propulsion system and determine the affects of pressure and temperature on the kinetics.

2.4.1 Methodology

The finite-rate kinetics simulation assumed that the fuel and oxidizer would enter the combustor perfectly mixed and at the same temperature based on the total enthalpy of the reactants. The intermediate reactions, shown in Eq. 17, and their corresponding rate constants were obtained from the literature [93]. In these equations, M denotes a 3rd body specie. Thermodynamic tables do not typically differentiate between condensed phases of magnesium oxide [100]. Therefore, this study ignored Eq. 17f and interpreted MgO(l) as a condensed phase in Eq. 17e. Note that the inclusion of carbon in Eqs. 17b and 17j made the integration scheme numerically ill-conditioned. Therefore, Eq. 17j was ignored and carbon was introduced into the system in partial equilibrium according to Eq. 17b, which was the faster of the two reactions. Sensitivity studies demonstrated that the partial equilibrium assumption had a minor affect on the kinetics.

$$Mg + CO_2 \leftrightarrow MgO + CO \tag{17a}$$

$$Mg + CO \leftrightarrow MgO + C \tag{17b}$$

$$Mg + O_2 \leftrightarrow MgO + O \tag{17c}$$

$$Mg + O + M \leftrightarrow MgO + M \tag{17d}$$

$$MgO \leftrightarrow MgO(l) \tag{17e}$$

$$MgO \leftrightarrow MgO(s) \tag{17f}$$

$$Mg + CO_2 \leftrightarrow MgO + CO \tag{17g}$$

$$2O + M \leftrightarrow O_2 + M \tag{17h}$$

$$CO + O + M \leftrightarrow CO_2 + M \tag{17i}$$

$$C + O_2 \leftrightarrow CO + O \tag{17j}$$
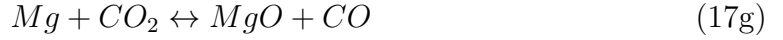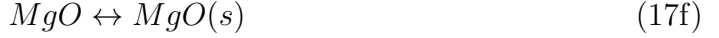
From the elementary reaction equations it was possible to set up a first-order system of ordinary differential equations of the form of Eq. 18. In this equation, $\mathbf{X}$ is the vector of all of species concentrations and A is a square matrix. A is specific to a given set of elementary equations and is a function of the forward and backward rate constants of those equations and the current specie concentrations. A Runge-Kutta 4th order method was used to integrate Eq. 18 forward in time.

$$\frac{d\mathbf{X}}{dt} = A\mathbf{X} \tag{18}$$

The temperature and volume of the mixture were calculated by enforcing conservation of mass and energy at each iteration using Eqs. 19 and 20. In these equations a_{tot} is the total number of moles of a given atom and h_{tot} is the total enthalpy of the system. V is the total volume of gas.

$$a_{tot} = V \sum X_i a_i \tag{19}$$

$$h_{tot} = V \sum X_i h_{T,i} \tag{20}$$

49

The finite rate kinetics simulation was validated by checking the conservation of mass and energy at each iteration and comparing the steady state solution to that obtained from the equilibrium combustion simulation.

2.4.2 Ignition Results

A study was performed to calculate the ignition delay of Mg - CO_2 mixtures for an ABSRP vehicle. Four points were chosen on the MSL trajectory at M = 1, 2, 3, and 4. As in the equilibrium combustion simulation, the freestream carbon dioxide at these points passed through a normal shock and was isentropically compressed with pressure ratios varying between 1 and 100. The magnesium fuel was preheated up to the oxidizer temperature with ratios varying between 0 and 1. Both reactants were assumed to enter the combustion chamber at a single temperature based on the mixture total enthalpy, but the time required to equilibrate temperatures was considered to be instantaneous. This simulation analyzed the case of $OF = 4$.

The simulation was run for a total of 0.1 s because ignition delays beyond that limit were expected to require an excessively long combustion chamber. If the mixture had not reached steady state in that time it was recorded as having not combusted. The ignition point was chosen to be where the temperature had undergone ninety percent of its total increase, defined by Eq. 21. In Eq. 21, $T_{induction}$ is the temperature at ignition, $T_{initial}$ is the temperature at the beginning of the simulation, and T_{final} is the maximum temperature.

$$T_{induction} = 0.9T_{final} + 0.1T_{initial} \tag{21}$$

Because an actual propulsion system would combust gaseous carbon dioxide with solid magnesium particles, these two species were chosen as the reactants. However, because kinetics data were only available for gas-phase reactions of Mg (no kinetics

data were available on the burning, melting, or vaporization of the Mg(s)), the simulation was initialized with both gaseous carbon dioxide and gaseous magnesium at a temperature equating the total enthalpy of the mixture to that of an equivalent Mg(s) reactant. The time required to convert the Mg(s) to Mg(g) was not considered the calculations. Across all of the trajectory points, compression ratios, and preheat amounts, no Mg(s) - CO_2 mixture combusted prior to 0.1 s. Therefore, it will be necessary to either vaporize the magnesium particles prior to combustion or include an igniter to start the engine.

A second study was performed that combusted gaseous magnesium and carbon dioxide reactants. Reactant pressures and temperatures were the same as for the Mg(s) - CO_2 simulations. None of the mixtures combusted within 0.1 s for the $M = 1$ and 2 trajectory points. Therefore, if the engine were to be ignited for a terminal burn the system would require an external ignition device. Induction delays for the $M = 3$ and 4 trajectory points are shown in Figure 22 with the induction delay (in seconds) plotted as a function of the compression pressure ratio and preheat temperature ratio. The values of both graphs are clipped at 0.1 s to indicate that combustion did not occur within the require time.

(a) Induction time for the $M = 3$ trajectory point

(b) Induction time for the $M = 4$ trajectory point
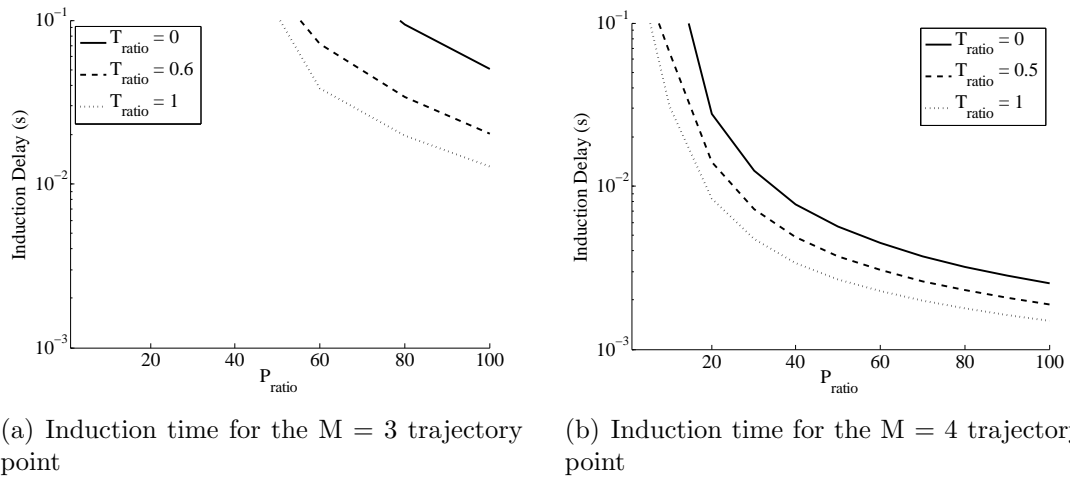
Figure 22: Induction delay times for a Mg(g)-CO_2 mixture as a function of isentropic compression pressure ratio and fuel temperature preheating ratio

As shown in Figure 22, the induction times are more sensitive to the compression pressure ratio than the preheat temperature ratio. This is a similar result to what was seen in the equilibrium combustion simulations. From Figure 22(a), a significant amount of compression is needed in order to ignite the mixture at M = 3. Depending on the flowpath and residence time of the combustion chamber an igniter may still be required. As shown in Figure 22(b), igniting at a higher Mach number allows for reasonably fast induction delays at lower compression ratios. The higher Mach number initiation provides both higher pressure and temperature conditions within the combustor, as evidenced in Table 2. Both the increased pressure and temperature improve the combustion kinetics and reduce the ignition delay time. If the engine is able to start at higher Mach numbers or if higher compression ratios are attainable then the propulsion system could be self-starting.

Experimental studies in the literature used fuel preheating or external ignition sources in order to reliably ignite $Mg(s)$ - CO_2 mixtures. Three experiments successfully ignited Mg - CO_2 mixtures through preheating: 2 mm $Mg(s)$ particles were observed to ignite in a CO_2 stream if the ambient temperature was above the Mg melting point (923 K) [89]; lean Mg - CO_2 mixtures at low pressure (8 to 48 kPa) ignited when the Mg particles were heated to above their melting temperature prior to the experiment [109]; and 10 mm Mg pucks ignited in a stagnated CO_2 stream at atmospheric pressure after being heated by an external heater [90]. External ignition sources were another way to induce ignition: small Mg particles (250 mesh) ignited readily with CO_2 via electric spark or hot wire; low pressure tests (0.21 bar) of similar samples ignited using electric spark ignition [97]; and lean mixtures of a powdered Mg - CO_2 Bunsen burner were successfully ignited using a propane torch [95]. However, these techniques do not ensure that $Mg(s)$ - CO_2 mixtures will always ignite: small, levitated Mg particles would not ignite using a CO_2 laser in an ambient temperature of 300 K and high pressure but larger particles in the same experiment did ignite

reliably [94]; and lean mixtures of powdered Mg and CO_2 did not ignite via propane torch or hot wire, requiring the addition of a small amount of O_2 to induce ignition [95].

2.4.3 Burning Time Results

After analyzing the propulsion system ignition characteristics, an additional study was performed to investigate the burning time of an existing Mg - CO_2 flame. For this study, solid magnesium and gaseous carbon dioxide entered the combustion chamber and were assumed to be heated as they approached the flame. A range of initial temperatures were considered, from 2029 K, an approximate combustion temperature corresponding to a high mach trajectory state, up to 3000 K, a representative adiabatic flame temperature for a Mg - CO_2 flame. The simulation was run for pressures ranging between $4x10^{-3}$ atm and 4 atm, encompassing the range of pressures expected during the trajectory for reasonable compression ratios and preheat ratios. For the current study, the mixture ratio was set at $OF = 4$. Burning times are presented in Figure 23 with the burning times calculated via Eq. 21.
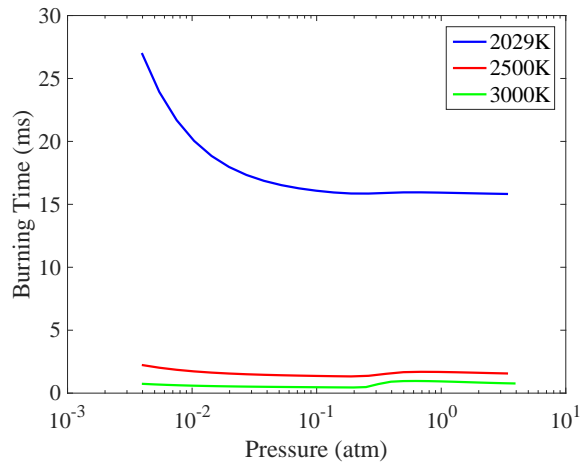
Figure 23: Mg - CO_2 burning times for various pressures expected during the trajectory

As seen in Figure 23, if particles are able to heat up to temperatures approaching the adiabatic flame temperature, burning times across all combustion pressures are

less than 1 ms. As temperature decreases, the mixture takes longer to combust. Burning times for mixtures heated to 2500 K require under 2 ms for nearly all pressures, with burning times increasing to between 15 and 25 ms for propellants combusting at a high mach trajectory state but with no heat diffusion from the flame. The longer burning times of the lower initial temperature cases are exacerbated by the conservative modeling assumptions. Like the ignition analysis in Section 2.4.2, due to the lack of information on solid magnesium kinetics, this simulation assumed that the solid magnesium was vaporized prior to combustion, adjusting the temperature to equate the total enthalpy of the mixture to that of an equivalent Mg(s) reactant. The resulting temperature loss was more conservative for the low initial temperature cases due to the lower total enthalpy of the reactants and the larger discrepancy in the gaseous and condensed phase specific heat values. In an actual engine, the energy required to vaporize the magnesium would be supplied by both the reactant enthalpy and the heat of combustion, corresponding to higher mixture temperatures than those simulated and, as a result, faster burning times.

These results demonstrate that the Mg - CO_2 mixtures will likely burn within a reasonably sized combustion chamber. The burning times were expected to decrease with increasing pressure. However, Figure 23 shows that burning times increase for the 3000 K mixture for pressures between 0.2 and 0.6 atm. By analyzing the temperature profiles versus time for each case, it was discovered that the temperature asymptotically approached its steady state value for pressures above 0.6 atm. For pressures below 0.2 atm the temperature rapidly overshot steady state and slowly relaxed to the final temperature. For these cases, since the peak temperature corresponded to the maximum heat release and since the relaxation to steady state was sufficiently slow, the maximum temperature was chosen as the burning point. Simulations conducted at pressures between 0.2 and 0.6 atm transitioned between the two temperature profiles.

Experimental results from other efforts confirm that sustained Mg - CO_2 flames are possible. Sustained Mg - CO_2 combustion was achieved with small Mg particles being transported by an N_2 carrier gas into the combustion chamber. After ignition via electric arc, a steady flame was observed at relevant flow-rates. The follow-on experiment validated the feasibility of a Mg - CO_2 rocket engine, demonstrating reliable ignition and sustained combustion [97]. Other studies also had success with propagate a flame in a mixture of Mg power and CO_2 at near stoichiometric mixtures. Flames would not propagate, however, for lean mixtures. In addition, despite its high theoretical flame speed, lean mixtures of powdered Mg - CO_2 were not observed to stabilize on a Bunsen burner [95].

2.5 Burning Particle Simulation

A notable assumption of the kinetics simulation was that it did not account for the effects of reactant distribution and diffusion, instead modeling the fuel and oxidizer as a homogeneously distributed mixture. In an actual engine, the solid magnesium will likely be injected into the combustion chamber as a suspension of solid particles in the oxidizer stream. In this case, complete combustion of the magnesium will require sustained heat transport and oxidizer diffusion to the particle in order for the solid magnesium to vaporize and react. The energy and species diffusion phenomena were assessed in a particle burning simulation, which calculated the time dependent droplet burning process.

2.5.1 Methodology

The full droplet burning process is described by a partial differential equation with three sets of boundary conditions: at the particle surface, at the far-field, and at the flame. Brute-force computation of the burning process is therefore considerably expensive. Instead, the model was simplified in order to enable decomposition of the problem into a set of conservation equations, which could be numerically solved

much more rapidly [91]. The first assumption drastically reduced the complexity of the full kinetics model by partitioning the simulation into two zones, an outer reaction zone off of the particle surface and the interface of the gas and condensed-phase on the surface. Two reactions were hypothesized to occur in these regions based on the analysis of magnesium particle burning experiments [88]. The first reaction was a modified version of the main elementary reaction for the full kinetics model, with gaseous magnesium combusting with carbon dioxide in the flame region away from the surface, producing carbon monoxide and magnesium oxide. The magnesium oxide product was then allowed to condense, contributing to the primary source of heat release of the mechanism. The second reaction was proposed based on interesting behavior observed during experimentation of burning magnesium droplets. Carbon monoxide was predicted to diffuse from the flame to the particle surface and react with condensed-phase magnesium to produce condensed-phase magnesium oxide and carbon. This reaction was more likely to occur on the particle surface due to it being favored in lower temperature regimes.

The method also assumed thin reaction zones separated by a diffusion zone, which did not allow for changes in chemistry. This geometry, shown in Figure 24, was qualitatively observed during experimentation and is mathematically described by infinitely fast reactions in the flame region. The ratio of kinetic and diffusive timescales was allowed to vary parametrically for the surface reaction through adjustment of the reaction activation energy. The model accounted for energy transport through convection and conduction between the flame sheet, the particle surface, and the far-field, and also included radiation between the regions. The use of constant values for the density-diffusivity product (ρD), thermal conductivity, and heat capacity also enabled the use of algebraic equations to describe the burning process.

The set of conservation equations described the quasi-steady burning characteristics of a particle of a specified diameter under a specified set of atmospheric conditions.
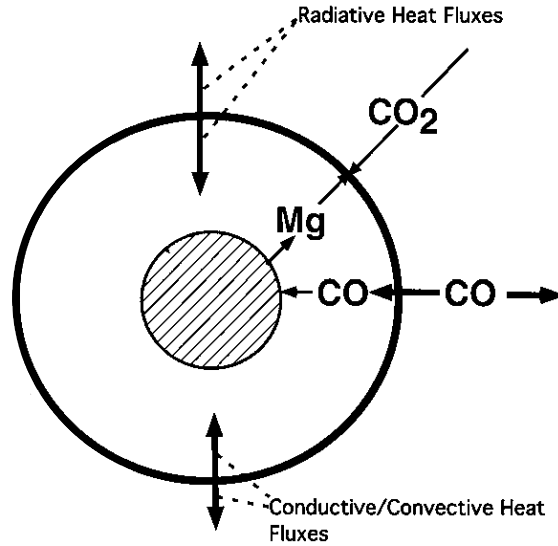
Figure 24: Diagram of the particle burning geometry, discussing the two reaction zones and intermediate diffusion zone [91]

The equations were numerically solved using an iterative method to determine the temperature values and mass consumption rates of the species. The rate of change of the particle radius was determined from the magnesium mass consumption rate and the mass deposition rates of the condensed-phase carbon and magnesium oxide on the particle surface. The rate of change of the radius and the total mass of magnesium were then integrated from the initial size and mass, progressing to no remaining magnesium, converging on the instantaneous quasi-steady burning characteristics and mass consumption values during each time step.

One noted weakness of the method is with the treatment of the condensed-phase magnesium oxide and carbon that are generate on the surface. These products are assume to aggregate near the surface, mixing with the local species but not participating or hindering reactions or vaporization. This assumption is most valid near the onset of burning but becomes decreasingly so as combustion progresses.

The particle burning model is based on the methodology developed by King, which describes the full assumptions and relevant conservation equations [91]. The implementation in this study differs slightly, by assuming that all of the magnesium

oxide condenses following reaction in the flame region; whereas, the original paper incorporated the effects of the gaseous and condensed-phase equilibrium in the heat release (but not diffusion) calculations. This discrepancy was seen to have negligible effect on the results over the full range of conditions considered, as is subsequently discussed.

2.5.2 Validation

Multiple validation checks were performed to ensure accuracy of the model. The first of which was to compare against the results from the original paper to ensure correct implementation of the equations and assumptions. Accuracy of the converged solution to the conservation equations was checked by comparing the heat balance terms for a given radius, as listed in Table 3. It is evident from the table that the results are reasonable and discrepancies are attributable to slight changes in the implementation or convergence algorithm, with the exception of the $\epsilon = 0$ case, where this model significantly overpredicts the flame region temperature. The reason for this discrepancy is due to the modeling of the flame-region reaction in this simulation, which assumes that all of the magnesium oxide product will condense following the reaction. The King model, conversely, allows for phase equilibrium of the gaseous and condensed-phase magnesium oxide, which lowers the temperature due to the higher enthalpy of the gas phase product. This occurs primarily for the zero emissivity case due to the effective removal of the term for radiating heat away from the body, which would counteract any increase in temperature in the flame region. Nevertheless, despite the large temperature difference, the total error in heat balance is small due to the compensating effects of the increased conductive and convective heat feedback from the flame region to the surface and the corresponding reduction in heat from the surface reaction due to the adverse temperature conditions. Indeed, it is observed that the net effect of the modeling differences for the flame-region reaction is small

over all cases, due to balance and feedback of the energy transport mechanisms.

Table 3: Surface heat balance terms for various emissivity values for particles with transport-limited surface reactions. Simulations are conducted for $P = 1$ atm, $r_s = 0.02$ cm, $T_{amb} = 300$ K. Columns represent the particle emissivity, heat needed for Mg vaporization, heat from the surface reaction, conductive and convective heat feedback from the flame region, radiative feedback from the flame region, and the flame region temperature. Units of all heat terms are cal/s and temperature are K. King refers to original methodology implementation (from [91]) and Study refers to the methodology developed for this investigation.

ϵ	Mg Vap.		Surface Rx		Cond./Conv.		Radiation		Flame Temp.	
	King	Study	King	Study	King	Study	King	Study	King	Study
0.00	0.466	0.470	0.407	0.388	0.060	0.082	0.000	0.000	3674	4328
0.25	0.466	0.463	0.409	0.406	0.037	0.037	0.020	0.020	2658	2669
0.50	0.468	0.466	0.402	0.399	0.026	0.026	0.040	0.042	2284	2300
0.75	0.471	0.469	0.393	0.390	0.020	0.020	0.059	0.060	2088	2096
1.00	0.475	0.473	0.386	0.382	0.015	0.016	0.073	0.076	1948	1958

The simulation was also verified by comparing the results of both implementations to various parameter sweeps conducted by King. Shown in Figure 25 is one particular comparisons of the the magnesium consumption rate as a function of activation energy. This comparison was chosen to validate the metrics used for the burning time integration. It is again evident that both solutions predict the same performance. Minor discrepancies in burn rate are possibly from differences in implementation but can also be attributed to errors in digitizing the original dataset.

The final validation was performed on the burn time estimates to compare the overall prediction of each simulation, listed in Table 4. It is evident that burn time predictions between both implementations are similar. As a result, the combination of all three comparisons validates that the particle burning simulation accurately solves the conservation equations to determine the particle burning time.

The numerical model was also compared against a simplified analytic model as a further check on its performance. The analytic model made similar assumptions of vanishingly thin reaction zones separated by regions of no chemistry and calculated
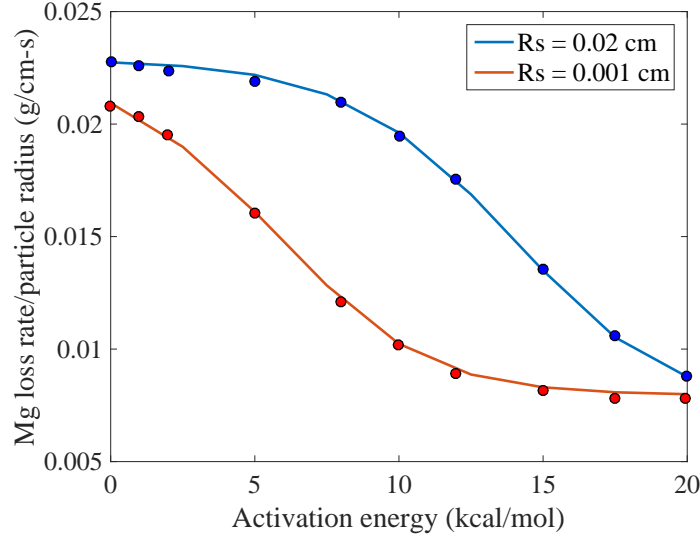
Figure 25: Graphs of the magnesium loss rate divided by particle radius for a range of activation energies of the surface reaction. Simulations are conducted at $P = 1$ atm, $\epsilon = 1.0$, $T_{amb} = 300$ K. Top curve represents solutions for $r_s = 0.02$ cm and bottom curve for $r_s = 0.001$ cm. Lines represent curves generated in this simulation and points are solutions from King [91].

Table 4: Predicted burn times for particles with varying initial radii and surface reaction activation energy. Simulations are conducted for $P = 1$ atm, $\epsilon = 0$, $T_{amb} = 300$ K. Units of initial radii are in cm, burn times are in s, and activation energies are in cal/mol. King refers to original methodology implementation (from [91]) and Study refers to the methodology developed for this investigation.

r_s	$E_{Act} = 0$		$E_{Act} = 10,000$		$E_{Act} = 20,000$	
	King	Study	King	Study	King	Study
0.002	0.0014	0.0014	0.0028	0.0029	0.0045	0.0046
0.004	0.0054	0.0055	0.0100	0.0093	0.0179	0.0181
0.006	0.0122	0.0123	0.0196	0.0188	0.0387	0.0401
0.008	0.0216	0.0217	0.0310	0.0310	0.0680	0.0700
0.010	0.0336	0.0338	0.0455	0.0460	0.1052	0.1076
0.012	0.0484	0.0485	0.0629	0.0638	0.1499	0.1525
0.014	0.0658	0.0659	0.0832	0.0843	0.2019	0.2045
0.016	0.0858	0.0860	0.1063	0.1074	0.2609	0.2632
0.018	0.1088	0.1088	0.1322	0.1333	0.3265	0.3283
0.020	0.1340	0.1342	0.1609	0.1618	0.3985	0.3998

the burning parameters based on sets of conserved scalars, or quantities that have no sources or sinks in the flow. The use of the conserved scalars, along with additional simplification of the physics, including the elimination of surface reactions and radiation heat transfer, allowed for the set of conservation equations and the burning rate to be described by a single analytic equation, presented in Eqs. 22, 23, and 24. In the equations, t_{burn} is the particle burning time, K is the inverse burning rate constant (defined in Eq. 23), $d_s(0)$ is the initial particle diameter, λ is the thermal conductivity, ρ is the density, c_P is the specific heat, B is the Spalding transfer number (defined in Eq. 24), Y is the mass fraction, m is the mass, Δh_R is the heat of reaction, and h is the enthalpy. The subscript s denotes properties at the particle surface, $cond$ denotes properties of the condensed phase, ox denotes properties of the oxidizer, ∞ denotes properties of the ambient gas, f denotes properties of the fuel, $stoich$ denotes properties at stoichiometric conditions, and $vapor$ denotes properties of the vapor.

$$t_{burn} = K d_s^2(0) \tag{22}$$

$$K = \left(8 \frac{\lambda}{\rho_{cond} c_P} ln(1+B) \right)^{-1} \tag{23}$$

$$B \approx Y_{ox,\infty} \left(\frac{m_f}{m_{ox}} \right)\Bigg|_{stoich} \frac{-\Delta h_R}{h_{vapor} - h_{cond}} \tag{24}$$

The value of K calculated from the analytic equation is 1.56 s/mm^2; whereas, the King model predicted values of 3.08 s/mm^2 for particles with no surface reactions and 0.83 s/mm^2 for particles with diffusion limited surface reactions. Thus, is can be seen that the analytic equation predicts burning times half a long as the comparable numerical prediction and twice as long as the numerical prediction. Given the number of assumptions of the physics and parameter values, this difference is not unexpected and shows that the results of the numerical model are reasonable values.

The numerical model predictions were also compared against experimentally determined burning rates of magnesium particles in a carbon-dioxide stream, shown in

Eq. 25 [93, 94, 88, 91]. The burning times of a representative 100 μm particle are shown next to their corresponding expressions. Note that the average burn time for these experimental values is 5.1 ms. The units of the equations are in s and mm. t_b denotes the burning time and d is the initial droplet diameter.

Numerical model (with surface reactions) [91]:

$$t_b = 0.83d_s^2 \quad t_b = 8.3 \times 10^{-3}\text{s} \tag{25a}$$

Numerical model (without surface reactions) [91]:

$$t_b = 3.1d_s^2 \quad t_b = 3.1 \times 10^{-2}\text{s} \tag{25b}$$

Analytic model:

$$t_b = 1.6d_s^2 \quad t_b = 1.6 \times 10^{-2}\text{s} \tag{25c}$$

Abbud-Madrid et al. (in reduced gravity) [93]:

$$t_b = 1.0d_s^2 \quad t_b = 1.0 \times 10^{-2}\text{s} \tag{25d}$$

Abbud-Madrid et al. (in terrestrial gravity) [93]:

$$t_b = 0.5d_s^2 \quad t_b = 5.0 \times 10^{-3}\text{s} \tag{25e}$$

Legrand et al. [94]:

$$t_b = 0.5d_s^2 \quad t_b = 5.0 \times 10^{-3}\text{s} \tag{25f}$$

Shafirovich et al. [88]:

$$t_b = 0.25d_s^{2.7} \quad t_b = 5.0 \times 10^{-4}\text{s} \tag{25g}$$

The closest reference experiment is that of Abbud-Madrid in reduced gravity because it eliminates the effects of buoyancy on the results (which are not considered in the numerical model). This is confirmed by the fact that the reduced gravity results lie in between the diffusion and kinetic limited results of the numerical model. The

correlation is encouraging, because it shows that errors due to model assumptions (such as the assumptions that the condensed phase products of the surface reaction accumulate and remain on the surface and that the burning process is modeled as being quasi-steady, so transient processes such as the particle heat-up phase are not captured) are smaller than the natural variability due to the parametric modeling of the surface kinetics. Experiments conducted in terrestrial gravity are observed to be twice as fast for both Abbud-Madrid et al.'s equivalent experiment and Legrand et al.'s experiment and significantly faster for the studies conducted by Shafirovich et al. Given the modest number of experiments conducted, there is no precise characterization of the burning process. Nevertheless, the similar prediction of the numerical model with the experimental results and, in particular, the correlation with the reduced gravity analysis demonstrates that the numerical model is adequate for assessing the magnesium - carbon dioxide particle burning process.

Application of the proposed engine will introduce a more chaotic combustion environment, which will also influence the burning times. This will include turbulent mixing effects, which would increase diffusion and potentially improve combustion. The large fractions of hot, condensed phase products could also improve combustion time estimates by contributing to increased radiation heat transfer back to the particle, radiation from the products being neglected in the numerical model. Evaluating the magnitude of these effects in not possible with the current dataset due to the limited amount of information and would require repeated experimentation in a relevant combustion environment.

2.5.3   Results

The particle burning simulation was used to evaluate the estimated particle burning time, characterize variations in the burning time due to the combustion system

environment, and understand the uncertainty due to variations in assumed model parameters. Results were simulated for a range of model parameters, varying both the emissivity and activation energy of the surface reaction (to parametrically simulate variation in the ratio of kinetic and diffusive timescales). Simulations were conducted at a pressure of 200 kPa (around 2 atm), which was determine to be the pressure resulting from median values across all flight environments and combustion system performance parameters (discussed in Section 2.6).

As observed in Figure 26, the results are qualitatively similar to those seen in the reference study at a pressure of 1 atm. The kinetic timescales are observed to have a significant effect on the results; whereas, the radiation effects are seen to be negligible. Similar results were observed in the original implementation of the algorithm. The surface reaction is important because it allows for sustained magnesium consumption, due to both vaporization at the surface and direct reactions with carbon monoxide. The reaction is also favorable at much lower temperatures than the flame reaction, which allows for faster onset of burning.

For a particle size of 100 μm, cases with negligible surface reactions required up to 21.1 ms to completely burn whereas less restricted and fully diffusion limited cases took 9.4 ms and 8.3 ms to burn, respectively. This corresponds to a factor of three variation in the burn time results. It is important to note that all of the parameters varied in this simulation are not directly controllable through the propulsion system design variables and are, instead, inherent to the magnesium and carbon-dioxide propellants. Therefore, these results do not show how to design the combustor in order to influence the combustion length scales, as much as they show how the uncertainties in the combustion characteristics affect the final result. While realistic surface kinetics are expected to lie in between the two extremes considered, it is clear that uncertainty in the particle burning physics can significantly contribute to performance variation.
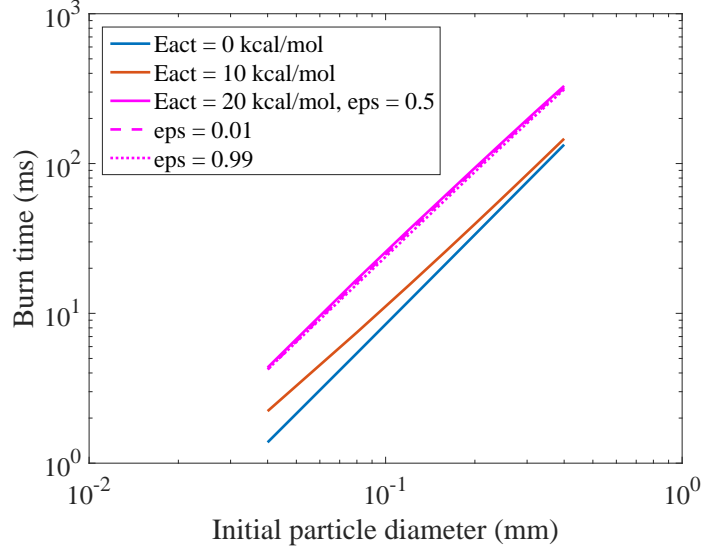
Figure 26: Graph of the burning time for particles of different diameters. Curves represent cases run with different activation energies to show impact of the surface reactions and different emissivities to show the impact of radiative heat transfer. Simulations are conducted at $P = 200$ kPa and equivalent temperature.

The effects of the flight environment on the burn time predictions were also investigated by varying the combustion pressure and corresponding temperature (according to the model in Section 2.6). Results are presented in Figure 27. Runs were conducted with an emissivity of 0.5 and surface reaction activation energy of 10,000 cal/mol. Pressures values of 1 kPa, 200 kPa, and 400 kPa were selected: 1 kPa corresponding to the lowest pressure expected during the trajectory (the nominal surface pressure on Mars is 626 kPa [2]), 200 kPa corresponds to the pressure for the median trajectory state and engine parameters, and 400 kPa represents a reasonably high pressure for the trajectory, encompassing over 80% of the pressures expected and corresponds to either an extreme flight environment or an extreme propulsion system design.

The original implementation of the numerical particle burning simulation (conducted at $P = 1$ atm) observed that burning times were relatively insensitive to variation in pressure. This is confirmed when comparing the $P = 200$ kPa and $P = 400$ kPa cases (approximately 2 and 4 atm, respectively). However, the low pressure result shows significant variation, which is to be expected. Therefore, it is
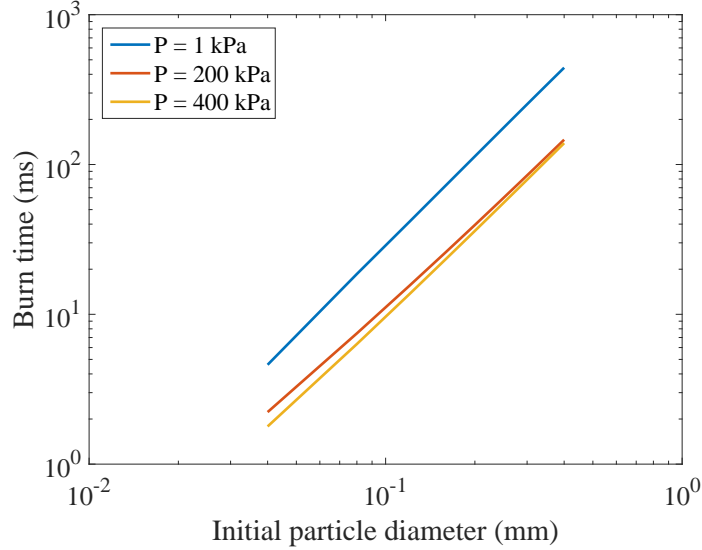
Figure 27: Graph of the burning time for particles of different diameters. Curves represent cases run with different combustion pressures to show impact of the flight environment on the burn time. Simulations are conducted for emissivities of 0.5 and surface reaction activation energies of 10,000 cal/mol.

likely that the ambient combustion pressure is a strong driver of the burning time up to some threshold value, after which variation due to pressure is significantly reduced. Higher pressure regimes are observed to have favorable burning times, with a 100 μm particle burning in 9.4 ms at 200 kPa and in 8.7 ms at 400 kPa, whereas the low-pressure burning time was as high as 27.7 ms.

Burning times are of primary importance for combustion chamber sizing. Depending on the relationship between the burning time and combustion chamber residence time, incomplete combustion or delayed heat release may be a concern, which would significantly hinder the propulsion system performance and efficiency. Combustion will occur subsonically in the retropropulsion engine, with the speed of sound of the propellant mixture being approximately 700 m/s. Assuming that heat release occurs at approximately Mach 0.5 and that the combustion chamber length is an order of magnitude smaller than the vehicle characteristic dimension (entry vehicles are expected to have heatshields on the order of 10 m diameter), this corresponds to a combustion chamber residence time of around 3 ms. Therefore, it is evident

that the chamber residence times and particle burning times are on the same order, which demonstrates that complete combustion is possible within a reasonably sized combustion chamber. Some adjustment of the propulsion system parameters may be necessary if it is determined that the surface reaction kinetics are particularly slow or if combustion pressures approach the lower limit possible during the trajectory but, even for these extremes, the necessary combustor length is still smaller than the characteristic dimensions of the vehicle.

If necessary, faster burning times can be achieved by utilizing smaller magnesium particles. Previous experimental studies combusted particles as small as 50 μm diameter. If particles of this size are used instead of the larger 100 μm particles, burning times for all cases would be below the 3 ms target except for the no surface reactions (5.3 ms burn time) and low pressure (1 kPa, 6.9 ms burn time) cases. These results demonstrate that complete combustion is a reasonable assumption and that, to first order, the propulsion system performance can be described by the equilibrium results.

2.6   Combustion Performance Reformulation

The equilibrium combustion results in Section 2.3 were useful for assessing the performance sensitivities to the combustion design parameters. However, the results made a number of assumptions that limited their applicability. Notable deficiencies were that the calculations assumed the propulsion system to be fully expanded and that the trajectory states were linked to the MSL trajectory. As a result, the results were not applicable to generalized sets of engine design parameters operating in general flight environments; therefore, they were not conducive to use in the trajectory simulations.

This motivated the reformulation of the equilibrium combustion results in terms of generalized parameters that could be determined during the trajectory simulation. In the original simulation, the trajectory, pressure ratio, and temperature ratio results were translated into definable combustion parameters: the combustion pressure,

expansion pressure, and fuel and oxidizer temperatures. Therefore, these parameters were used as the independent variables for the combustion performance maps.

2.6.1   Expansion Pressure Mapping

While the combustion pressure and temperatures could be calculated from the flight environment and the engine design, the expansion pressure was not easily determined, being a function of the combustion and expansion processes. This was solved through the use of the mass flow rate which, following fuel injection, was a constant throughout the engine. The mass flow rate, defined in Eq. 26, related the conditions at the exit plane of the engine to the throat plane based on their areas. The remaining parameters, the density and the velocity, were easily calculated from the equilibrium simulation, by isentropically expanding the products to the specified exit pressure. This allowed for the mapping of the mass flow rate to the exit pressure, which was then used to calculate the I_{SP}.

$$\dot{m} = \rho v A \tag{26}$$

2.6.2   Reduced Order Input Modeling

Calculation of the equilibrium combustion performance requires sampling from the propulsion system maps based on the instantaneous values of the four input parameters. Brute force generation and sampling of the four-dimensional map however, would be prohibitively time consuming. Instead, it was desired to develop a performance map that was based on a total of two parameters: one to define the combustion state based on the flight environment and engine design and the other to define the exit state based on the nozzle configuration.

The expansion pressure was the dominant parameter affecting the exit state so it was selected as a mapping input. The other three parameters, the combustion pressure and the fuel and oxidizer temperatures, all contributed to the definition of the combustion state. As discussed in the equilibrium combustion results, fuel

temperature variation (through modulation of the temperature ratio parameter) was observed to have negligible impact on the propulsion system performance. This was a result of both the pressure dominating the performance variability and the larger oxidizer mass fraction dominating the variability in total enthalpy. Therefore, the reduced order model eliminated the dependence on fuel temperature by assuming that it was equal to that of the oxidizer.

As a result, it was necessary to eliminate the dependence of the performance map to one of the two remaining parameters. For a given entry state and engine design, the combustion pressure and temperature are uniquely defined and, thus, uniquely related. However, due to compression from both the forebody shock and the on-board compressor, there exists a non-unique relationship between the combustion pressure and temperature based on the relative magnitude of compression from each source. As a result, combustion states arising from high shock compression and low on-board compression could have the same pressure as states arising from low shock compression and high on-board compression, but with different temperatures.

The magnitude of this deviation was assessed by calculating the pressure and temperature values for all expected combustion states during the trajectory. A parameter sweep was conducted which varied the compression pressure from 1 to 100 times compression, the freestream mach number from 1 to 4, and the freestream pressure from 336 to 626 Pa. The combination of these states encompassed the full range of possible engine configurations and set of expected flight environments during propulsive descent. Resulting combustion pressure and temperature values are displayed in Figure 28.

A curve was fit using the data, shown in green in Figure 28, to correlate the pressure and temperature values. Mapping of the reduced order model (pressure as a function of temperature, or temperature as a function of pressure) was determined based on the ordering that minimized the error in the final I_{SP} and $\dot{m}/A$ results.
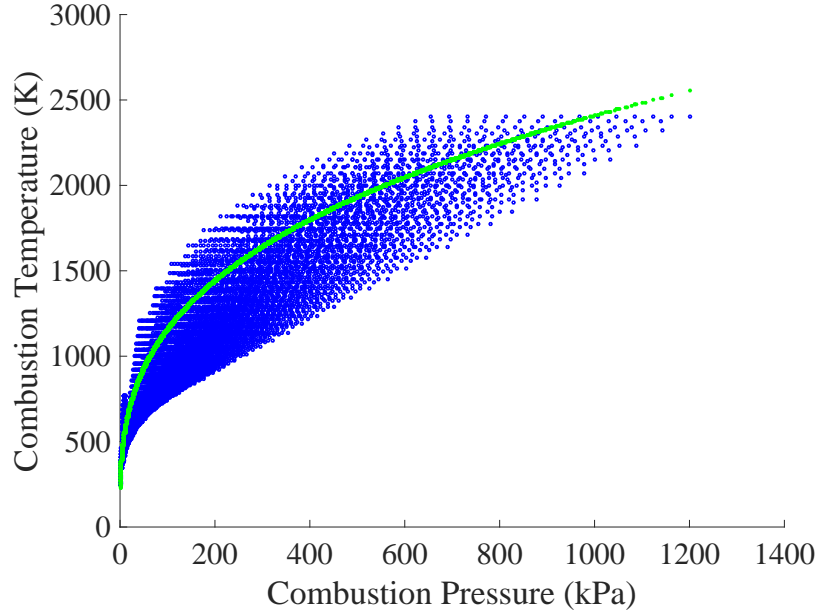
Figure 28: All combustion pressures and temperatures expected during propulsive descent, depicted with blue datapoints, along with the reduced-order combustion temperature model, depicted with the solid green line.

These errors were assessed by selecting a point on the reduced order model and perturbing the pressure and temperature values to their maximum possible errors relative to that point. The I_{SP} and $\dot{m}/A$ results were calculated for the nominal, as well as positive and negative perturbed points, to determine the maximum possible error in the results.

A summary of the I_{SP} and $\dot{m}/A$ uncertainty due to errors in the combustion pressure and temperature are shown in Tables 5 and 6. The nominal point used in Table 5 is the combustion pressure and temperature resulting from the median values of the compression ratio, freestream pressure, and freestream Mach number. The nominal point used in Table 6 is a reasonable estimate of the highest combustion pressure and associated temperature during the trajectory. Variation of I_{SP} and $\dot{m}/A$ with expansion pressure was also assessed in order to evaluate its relative effect on the results. Expansion pressure perturbations were not related to the reduced order model and were instead based on extreme possible values.

Table 5: Uncertainties in I_{SP} and $\dot{m}/A$ due to errors in the reduced order input model. Nominal point is the pressure resulting from the median values of compression ratio, freestream pressure, and freestream Mach number: $P_{comb} = 200$ kPa, $T_{comb} = 1100$ K, and $P_{exp} = 20$ kPa. Perturbed values are the maximum possible error in the input values at that selected point. Units of pressure are in kPa and temperature are in K. The percent variation in input parameters and percent error in I_{SP} and $\dot{m}/A$ are the percent errors with respect to the nominal values.

Input Parameter	Value	% Var Input	% Error I_{SP}	% Error $\dot{m}/A$
Combustion Temperature				
Perturb Up	1800	64	6.5	-7.1
Perturb Down	900	-18	-2.9	4.3
Range	900	82	9.4	11.4
Combustion Pressure				
Perturb Up	380	90	12	19
Perturb Down	39	-81	-45	-51
Range	341	171	57	70
Expansion Pressure				
Perturb Up	100	400	-43	150
Perturb Down	0.6	-97	46	-93
Range	99	497	89	243

Table 6: Uncertainties in I_{SP} and $\dot{m}/A$ due to errors in the reduced order input model. Nominal point is a reasonable upper bound on the pressure expected during the trajectory: $P_{comb} = 400$ kPa, $T_{comb} = 1600$ K, and $P_{exp} = 40$ kPa. Perturbed values are the maximum possible error in the input values at that selected point. Units of pressure are in kPa and temperature are in K. The percent variation in input parameters and percent error in I_{SP} and $\dot{m}/A$ are the percent errors with respect to the nominal values.

Input Parameter	Value	% Var Input	% Error I_{SP}	% Error $\dot{m}/A$
Combustion Temperature				
Perturb Up	2100	31	4.2	-4.2
Perturb Down	1200	-25	-3.8	4.7
Range	900	56	8.0	8.9
Combustion Pressure				
Perturb Up	680	70	10	15
Perturb Down	140	-65	-25	-30
Range	540	135	35	45
Expansion Pressure				
Perturb Up	200	400	-43	150
Perturb Down	0.6	-98	54	-96
Range	199	498	97	196

As shown in the tables, the possible error in combustion pressure at each point is more than double that of combustion temperature. Even when accounting for the discrepancy in the input uncertainties, the sensitivity of the I_{SP} and $\dot{m}/A$ results to variation in combustion pressure is still much greater than to combustion temperature. As a result, in an effort to minimize uncertainty in the propulsion performance, the combustion pressure was chosen as the mapping input describing the combustion state for the the equilibrium combustion data. The temperature value used in the combustion performance map generation was determined from the input pressure according to the relation in Eq. 27. In the equation, units of temperature are in K and pressure are in Pa.

$$T_{comb} = 29.3995 * (P_{comb})^{0.3189} \tag{27}$$

Removing the temperature from the equilibrium model did introduce some uncertainty in the results. Across both the I_{SP} and $\dot{m}/A$ results, maximum uncertainty due to errors in the combustion temperature were around 10%, with around 5% maximum error for perturbations in a single direction.

The sensitivity of the performance results to the expansion pressure is observed to be greater even than sensitivity to errors in combustion pressure. While the possible range of expansion pressures is much larger than the other two parameters, even when accounting for the magnitude of the input variation, the resulting error in the I_{SP} and $\dot{m}/A$ is still significant. This reinforced the use of the expansion pressure as the other mapping input parameter.

2.6.3 Combustion Models

Inspection of the equilibrium combustion results reveals the ABSRP engine to have both very modest performance and negligible I_{SP} for low-compression configurations. The sharp decline in performance is largely a function of the combustion being modeled as a constant pressure, constant enthalpy process, resulting in limited to no

pressure differential during expansion to drive an increase in mixture velocity. Note that steady-state flow fields conserve mass, momentum, and total-enthalpy values; and correspondingly, in the subsonic domain, even a modest heat release due to combustion yields an increase in both the velocity and I_{SP}.

Another way of modeling a combustion process is by assuming constant volume combustion, which does produce a pressure rise at low compression ratios and results in enhanced I_{SP} performance. In an effort to understand the effects of the combustion modeling, particularly at low compression ratios, an additional equilibrium combustion simulation was developed, which modeled the combustor as a constant volume process.

The constant volume combustion simulation was based on the same algorithm as the original constant pressure simulation, which iteratively converged upon the equilibrium composition and temperature of the combusting mixture by enforcing the conservation equations. The primary difference between the simulations was in the treatment of the static pressure equation (Eq. 14), which was replaced with a constant volume constraint, implemented by enforcing a constant mixture density. The conservation of energy equation was also reformulated to involve the relevant parameters, presented in Eq. 28. In the equations n is the number of moles, c_V is the specific heat at constant volume, and $E_{T_{ref}}$ is the energy of formation.

$$\sum n_i \Big(\int_{T_{ref}}^{T} c_V dT + E_{T_{ref}} \Big) = const \tag{28}$$

A comparison of the constant volume and constant pressure modeling results is shown in Figure 29. As observed in Figure 29(a), the constant volume simulation predicts higher I_{SP} values than the corresponding constant pressure simulation. The magnitude of the difference is reduced for even modest pressure ratios and continues to decreases as pressure is increased. For the Mach 4 trajectory point, shown in Figure 29(b), the constant pressure and constant volume results are similar, and converge for both increasing pressure ratio and increasing absolute pressure values. The $\dot{m}/A$
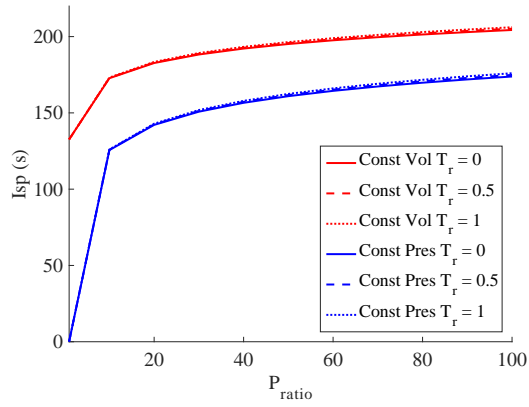
(a) I_{SP} results at the Mach 1 trajectory state
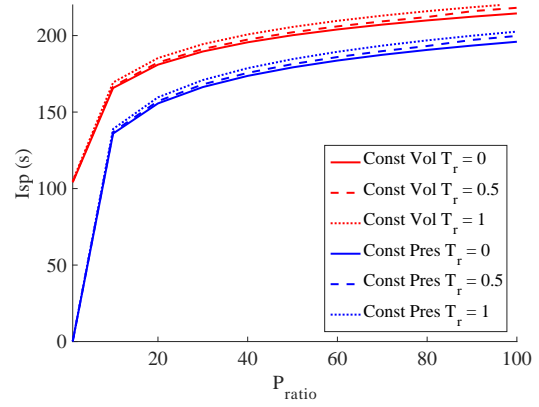
(b) I_{SP} results at the Mach 4 trajectory state
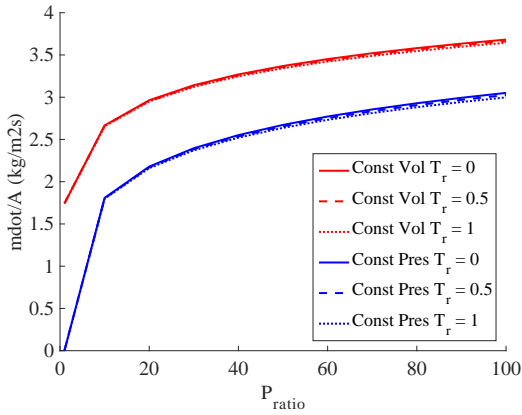
(c) $\dot{m}/A$ results at the Mach 1 trajectory state
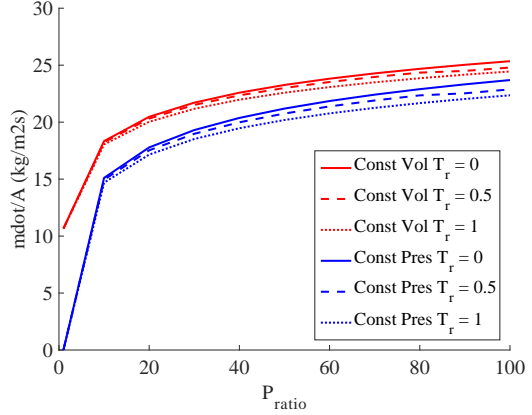
(d) $\dot{m}/A$ results at the Mach 4 trajectory state

Figure 29: Comparison of the I_{SP} and $\dot{m}/A$ results for the constant pressure and constant volume equilibrium combustion models as a function of the ratio between the combustion and expansion pressure and the amount of fuel preheating.

results, seen in Figures 29(c) and 29(d), display similar trends.

The constant volume and constant pressure assumptions model different engine processes. This investigation did not presuppose a specific engine and, instead, blended the performance results of the constant pressure and constant volume assumptions by taking an average (mean) of both results in order to eliminate the dependence on the engine type. Overall, this decision is observed to increase both the I_{SP} and propellant flow rate of the simulated engine with respect to a constant pressure process and have the opposite effect with respect to a constant volume process. The largest effect is seen for severely limited compression configurations, where the performance results differ significantly, with small to moderate differences for larger compression, larger absolute pressure configurations.

Sensitivity to engine modeling can be investigated by evaluating the overall performance sensitivity to the I_{SP} and mass flow rate. The compression pressure ratio is observed to have the same effect as scaling between the two engine models, resulting in an increase or decrease in both I_{SP} and $\dot{m}/A$. Therefore, assessing the impact of the engine modeling can be determined by using the pressure ratio as an equivalent metric.

2.7   Summary

The overall feasibility and performance of an ABSRP propulsion system is investigated through numerical simulation. Representative engines were seen to have sufficient I_{SP} values and burning rates.

An equilibrium combustion simulation was developed to calculate the ideal I_{SP} of an ABSRP propulsion system. The presence of solid species caused significant convergence issues in pre-existing equilibrium codes. Therefore, an independent simulation was developed which reformulated the equilibrium combustion algorithms to improve robustness and convergence for mixtures with solid phases. Realistic I_{SP} values in

an ABSRP relevant flight regime were around 120-160 s (corresponding to effective I_{SP} values of 600-800 s), double that of a traditional SRP propulsion system when calculated based on on-board propellant consumption. Attaining significant I_{SP} values will require moderate compression of the oxidizer prior to combustion. This must be achieved using an on-board subsystem because inlet compression alone is unable to provide sufficient pressure rise. Pressure ratios above 10-to-1 provide diminishing benefit in I_{SP} performance. In addition, preheating of the fuel does not provide any noticeable gain in the theoretical I_{SP} for reasonable compression ratios; however, it does significantly improve the combustion kinetics.

A finite-rate kinetics simulation was also developed to evaluate the kinetic timescales and to assess whether or not the combustion kinetics inhibited the theoretical I_{SP} predictions from being achieved. This simulation also evaluated the propulsion system's ability to ignite and maintain a flame. The Mg(s) - CO_2 mixture did not ignite for any of the considered trajectory points, pressure or temperature ratios. Therefore, either the magnesium needs to be vaporized prior to ignition or an igniter needs to be added to the engine. The Mg(g) - CO_2 mixture ignited for Mach 3+ initiation but required moderate compression. Simulation of the magnesium, carbon dioxide flame demonstrated that burning times were sufficiently fast for a wide range of pressures expected throughout the trajectory. Therefore, maintaining a Mg - CO_2 flame, from a kinetics standpoint, appears feasible.

The burning times were also assessed through a particle burning simulation, which evaluated the timescales of the diffusion effects. Combustion residence times were estimated to be on the order of 3 ms. Burning times were found to range between 2 and 27 ms, depending on the solid particle size, combustion pressure, and scaling of the diffusive and kinetic timescales of the surface reaction. These combustion chamber residence time and particle burning times are on the same order, which demonstrates that complete combustion is possible for magnesium - carbon dioxide

76

mixtures with reasonably sized combustion chambers. These findings also reinforce the assertion that the equilibrium combustion results are appropriate predictions of the combustion performance.

CHAPTER III

VEHICLE PERFORMANCE METHODOLOGY

3.1 Introduction

In addition to having adequate propulsive efficiency, effective descent systems must also translate their propulsive performance into favorable system performance. The performance of an atmospheric-breathing propulsion system is coupled to the local flight environment and the amount of oxidizer ingested. As a result, these additional constraints alter the trajectory and impose limits on the available thrust. This study develops integrated performance models of ABSRP vehicles in order to estimate the propellant usage and facilitate quantitative comparisons between different architectures and propulsion design parameters.

3.2 First-Order Feasibility of ABSRP

A first-order assessment of the feasibility of ABSRP was performed to understand the fundamental characteristics of atmospheric-breathing descent trajectories and the coupling effects between the oxidizer ingestion and available thrust. A three-degree of freedom, point-mass trajectory simulation that numerically integrated the descent equations of motion from conventional initial conditions was developed using Matlab. This simulation simplified the vehicle modeling by decoupling the propulsion system performance calculations, assuming a nominal efficiency value, and fixed initial conditions. The ABSRP efficiency was based on the equilibrium thermodynamics results and the propulsion initiation state was obtained from architectures evaluated in previous studies [55].

3.2.1 Methodology

The vehicle model assumed that the supersonic and subsonic aerodynamic and propulsion characteristics were independent. The drag coefficient was obtained from CFD simulations of SRP vehicles with a canted nozzle configuration and the lift coefficient was assumed to be zero [48]. The aeroshell reference diameter was 10 m, resulting in a reference area of 79 m^2. The inlets were modeled as to sweep out a column during descent through the atmosphere (of cross section equal to the inlet area, A_{inlet}), where all of the CO_2 within that column was captured by the inlets and processed by the propulsion system. Note that, as a result of this definition, the inlet area represents the total oxidizer capture area. Actual area of the physical inlet, found on the vehicle surface, would therefore be smaller. The efficiency of the inlet capture can be accounted for in future analyses by scaling the inlet area by the capture efficiency. It was also assumed that the engines were run in steady state during the entire descent so that all of the CO_2 captured was immediately combusted with Mg. An exponential atmosphere model was used, generated from nominal atmospheric properties [2].

Previous studies of human scale Mars entry vehicles (50 t dry mass) indicated that SRP initiation would occur at Mach 2.7 at an altitude of 4600 m, corresponding to an approximate velocity of 555 m/s [55]. An I_{SP} of 160 s was chosen for the trajectories based on inspection of the equilibrium combustion results. A summary of the simulation parameters is shown in Table 7.

Table 7: Trajectory parameters at simulation start and end

	Simulation Start	Simulation End
Dry mass (t)	50	50
I_{SP} (s)	160	160
Altitude (m)	4600	0
Velocity (m/s)	555	0

3.2.2 Discussion

A set of example trajectories for vehicles with varying inlet areas is shown in Figure 30. It is evident from the trajectories in Figure 30(a) that ABSRP vehicles running in steady state cannot achieve the desired terminal condition of zero velocity. This is due to the velocity dependence of the decelerative forces, thrust and drag. The thrust, described in Eq. 29, is velocity dependent through the ingested $\dot{m}_{ox}$ (Eq. 30) and the dynamic pressure term in the drag force (Eqs. 31 and 32) is velocity square dependent, whereas the counteracting force of gravity (Eq. 33) is independent of the vehicle velocity. Note in the equations that F denotes the forces acting on the vehicle, g_e is the acceleration due to gravity on Earth, I_{SP} is the specific impulse, OF is the oxidizer-to-fuel ratio, $\dot{m}_{ox}$ is the mass flowrate of ingested oxidizer, ρ is the freestream density, v is the vehicle velocity, A_{inlet} is the inlet area, q is the freestream dynamic pressure, C_D is the drag coefficient, A_{ref} is a reference area, and m is the total mass of the vehicle. Vector directions are as denoted in Figure 30(b).

$$F_{Thrust} = g_e I_{SP} \frac{OF + 1}{OF} \dot{m}_{ox} \tag{29}$$

$$\dot{m}_{ox} = \rho v A_{inlet} \tag{30}$$

$$F_{Drag} = q C_D A_{ref} \tag{31}$$

$$q = {}^1\!/_2 \rho v^2 \tag{32}$$

$$F_{Gravity} = mg \tag{33}$$

Therefore, much like a parachute or other aerodynamic body, without capture and storage of oxidizer, the ABSRP vehicle achieves a terminal-velocity condition which equilibrates the retropropulsive thrust and drag with gravity. Ignoring the effects of varying the oxidizer-to-fuel ratio, which causes a corresponding nonlinear response in the I_{SP}, the terminal velocity can be varied through the inlet area term, as evidenced

(a) Plot of altitude vs. velocity

(b) Terminal velocity force balance, modified from image of entry vehicle in [110]
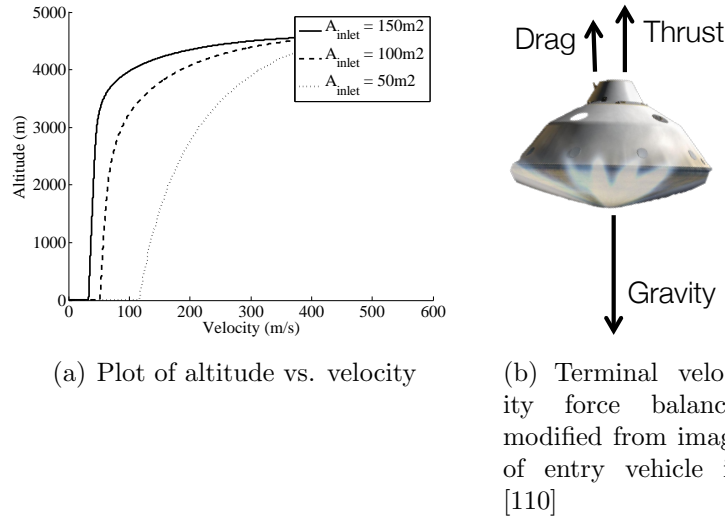
Figure 30: Example trajectories of ABSRP vehicles with varying inlet area

in Figure 30(a). Larger inlets process more oxidizer, producing more thrust and are able to achieve lower terminal velocities; whereas, smaller inlets produce less thrust and result in higher terminal velocities. Only in the limit of inlet area approaching infinity, however, does the terminal velocity achieve a value of zero. As a result, this first-order assessment demonstrates that, without capture and storage of oxidizer, an additional subsonic maneuver is necessary to negate the residual velocity and achieve the desired final state.

3.3 EDL Trajectory Simulation

An ABSRP trajectory simulation of the entire EDL sequence was developed in the Program to Optimize Simulated Trajectories II (POST), which numerically integrated the equations of motion [111]. This model was first used to duplicate and validate against the simplified matlab simulation. Specific modules were then iteratively added to expand the modeling capabilities and account for the additional phenomena. This simulation removed both of the primary simplifications used in Section 3.2 - the decoupled propulsion system performance and constrained propulsive initiation conditions. In order to determine the valid range of retropropulsive staging conditions,

a hypersonic deceleration segment was performed to bound possible trajectories.

3.3.1 Hypersonic Trajectory Optimization

Traditional hypersonic EDL guidance relies on bank angle modulation, or rotating the vehicle lift vector about the velocity vector. Bank angle modulation is useful for many objectives including the introduction of cross-range capabilities and downrange control for precision landing. In this three degree-of-freedom simulation, however, bank angle modulation is used exclusively to control the vehicle descent rate and adjust the altitude versus velocity profile.

Previous studies have addressed hypersonic guidance by employing heuristic optimization methods, which use large populations of candidate designs to search the design space [57, 112, 113]. These methods were shown to avoid the suboptimal local minimum and robustly determine favorable trajectories for a wide range of vehicle configurations. This study opted to use a genetic algorithm optimizer, in which individual members would quickly simulate the hypersonic phase of flight for a given bank angle and, as a population, seek out the optimal profile. The bank profile for each member was determined by directly controlling the bank angles at a set of Mach numbers, and linearly interpolating for data between the specified points. Twelve Mach values were chosen, distributed to provide sufficient coverage of the entire input range with higher density allocated to the more sensitive high Mach regime.

3.3.2 Vehicle Modeling Approach

The required propellant mass can be fully determined from the supersonic (propulsive) phase of flight, with the propellant mass being a unique function of the specific vehicle design parameters and SRP initiation state (in the three degree of freedom simulation taken to be initiation altitude, velocity, and flight path angle). For a given vehicle, optimization of the propellant mass equates to determining the optimal set of initial state variables. This was complicated somewhat due to the coupled nature of the

supersonic and hypersonic phases of flight. The supersonic trajectory is coupled to the hypersonic trajectory through bounds on the valid set of staging conditions. The hypersonic trajectory is also coupled to the supersonic trajectory because the varying propellant mass requirements from different supersonic trajectories result in different masses during the hypersonic flight segment.

(a) First step of the vehicle modeling: simulating a single supersonic/subsonic trajectory from a fixed set of initiation conditions

(b) Second step of the vehicle modeling: sweeping through initiation conditions to develop the propellant mass performance map
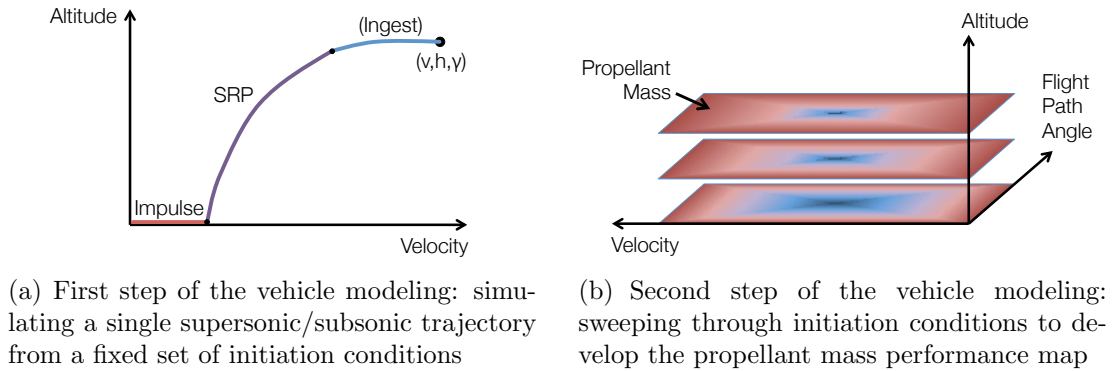
Figure 31: Diagram of steps used in the vehicle performance map generation

Classical optimizers were found to be efficient for the targeting routines used in the supersonic simulation; however, problems with coordinating the hypersonic bank angles precluded their use for hypersonic descent. Therefore, to optimize across both the hypersonic and supersonic domains, this study utilized a dual sequential quadratic programming - genetic algorithm optimizer approach that leveraged the strengths of both classical and heuristic optimization algorithms. Propulsive initiation was assumed to start at a specified set of conditions and propulsive descent and targeting were coordinated by the classical, sequential quadratic programming optimizer, which converged upon a unique propellant mass consumption estimate, shown in Figure 31(a). A map of the propulsive initiation design space was developed by sweeping the altitude, velocity, and flight path angle inputs throughout their applicable domains, as shown in Figure 31(b). While this solution introduced more supersonic trajectories to be run, each trajectory in the map could be conducted in parallel, which considerably

reduced overall computational time. The 500 point map implemented in this study running on 24 cores required 30 minutes to complete.

(a) Third step of the vehicle modeling: simulating a hypersonic trajectory for a single bank angle profile, which intersects the performance map

(b) Fourth step of the vehicle modeling: optimization of the hypersonic bank profile to target favorable initiation conditions that minimize the vehicle mass
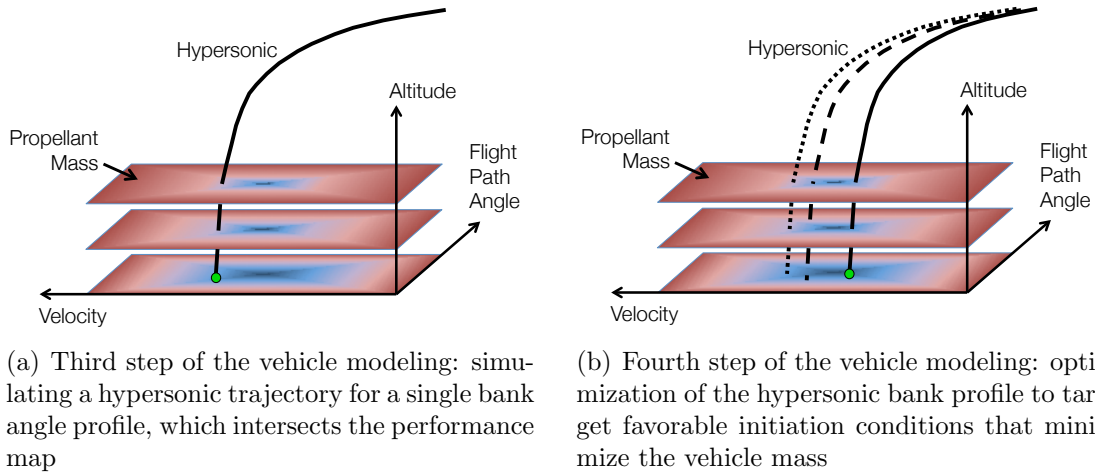
Figure 32: Diagram of steps used in the hypersonic trajectory targeting

The propellant mass map was then transferred to the hypersonic descent simulation. The genetic algorithm optimizer specified the bank profile for each of the hypersonic entry segments. These trajectories passed through the supersonic performance map and a propellant mass value was assigned to each point in the trajectory according to the propellant mass required if propulsion was initiated at that instant, shown in Figure 32(a). The vehicle mass was then updated with the minimum propellant mass required and the trajectory was repeated until the assumed propellant mass was equal to the minimum resultant propellant mass during the trajectory. In this way, the hypersonic simulation leveraged the power of the parallelized genetic algorithm to rapidly simulate trajectories in order to converge to an approximate global optimum, as visualized in Figure 32(b). With each of the individual hypersonic trajectories requiring 2 seconds computational time, 10 seconds when including propellant mass convergence, the duration of the entire hypersonic simulation was approximately 17 minutes when run on 24 cores. Like the supersonic simulation, each of these runs

could be conducted in parallel, up to the maximum number of members per generation. Mass optimization was managed by the genetic algorithm, which proved to be more robust that the classical optimizer and better able to search the entire design space. Care was also taken to ensure the optimality of the decomposed algorithm by separating all convergence routines to the supersonic descent simulation and allowing for pure targeting of the propellant usage map in the hypersonic simulation.

3.3.3 Vehicle Architectures

As discussed in section 3.2, due to the dependence of the vehicle velocity on the atmospheric-breathing thrust, ABSRP vehicles require an additional subsonic maneuver to meet the desired zero velocity target condition. Therefore, an impulsive burn was added following propulsive descent to negate the residual velocity. Two different vehicle architectures were considered, each implementing the impulsive maneuver differently. The first solution was to use the atmospheric-breathing engine for both descent and landing (referred to as the ABSRP-Only vehicle) and the second was to switch to a rocket engine when performing the impulsive maneuver (referred to as the Rocket-Impulsive vehicle).

The benefit of the ABSRP-Only solution was that a single propulsion system would be used for all stages of flight. To bypass the velocity dependent propulsion performance however, it was necessary to supplement the oxidizer supply during the impulsive maneuver. In this way, the atmospheric-breathing engine could be converted to a pseudo-rocket propulsion engine that was not dependent on oxidizer ingestion for thrust. To generate this oxidizer supply, an additional phase of flight was added prior to propulsion system initiation, in which the vehicle ingested and stored freestream oxidizer instead of using it for thrust. Once the requisite mass of oxidizer had been stored, the engine would start thrusting in steady state until the vehicle approached the ground. At that point, the engine would switch back to

the stored oxidizer supply to satisfy the impulsive maneuver oxidizer requirements. The oxidizer ingestion phase was added prior to propulsive initiation due to the large oxidizer mass flowrate during this time, shortening the maneuver duration. The separate engine modes would likely require dual flowpaths to be introduced, as seen in Figure 33, one for steady state combustion and exhaust (depicted in red) and one for storage and impulsive thrust (depicted in blue). While this would contribute to increased mass and complexity, commonality between many of the propulsion system elements (depicted in green) would mitigate mass growth as much as possible. In the figure, Item 1 is the freestream oxidizer flow, Item 2 is inlet compression, Item 3 is oxidizer stagnation and turning, Item 4 is on-board compression, Item 5 is fuel-oxizider mixing, Item 6 is combustion, and Item 7 is exhaust of the propellant. Items A and B are the fuel and oxidizer storage tanks, respectively. The dashed lines around tank B signify gates that can be open or closed to allow for oxidizer ingestion and storage or impulsive thrust.
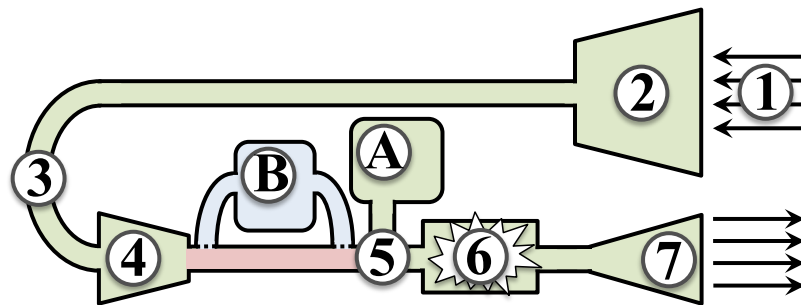
Figure 33: Notional flowpath diagram for the ABSRP engine used for both the descent and impulsive maneuvers

The benefit of the Rocket-Impulsive solution was that all propulsion technologies would be utilized in their most effective flight regimes. The atmospheric-breathing engine would provide fuel-efficient thrust when oxidizer ingestion was available and the rocket engine would enable a higher efficiency propulsion cycle (and possible higher energy propellant mixture) for improved low velocity performance. These systems could potentially be integrated together, in a similar manner as a rocket-based

combined cycle engine, to reduce mass. This investigation, however, conservatively assumed that the Rocket-Impulsive architecture involved two independent propulsion systems and evaluated whether or not the propellant mass savings could outweigh the total engine mass increase.

An additional rocket only simulation was also developed (referred to as the Rocket-Only vehicle), which employed a constant thrust rocket engine for both the descent and impulsive maneuvers. This simulation was used as the baseline vehicle from which to compare the performance of the different ABSRP architectures.

3.3.4 Subsystem Modeling

Individual modules were developed to model specific subsystems and capabilities. These modules were incorporated into the overall vehicle models in order to capture the relevant physics and improve the modeling fidelity.

3.3.4.1 Force Accounting

Force accounting is important for airbreathing vehicles in order to understand all contributions to the thrust and drag and to accurately calculate the net acceleration. Force accounting equations are readily available for traditional airbreathing engines, which feature an inlet on the forebody of the vehicle and exhaust on the aftbody. The geometry of atmospheric-breathing retropropulsion engines however, is significantly different. Due to the need for thrust directed in opposition to the vehicle velocity vector, retropropulsion engines feature both the inlet and exhaust on the vehicle forebody, as shown in the notional diagram in Figure 34. As a result, derivation of the relevant force accounting equations was necessary.

Force accounting for airframe integrated vehicles leads to a somewhat ambiguous distinction between aerodynamic and propulsive forces. As a result, it is convenient to describe the net force on the vehicle as the sum of the internal flowpath forces and the external vehicle forces. The internal flowpath forces are described in Eq. 34.
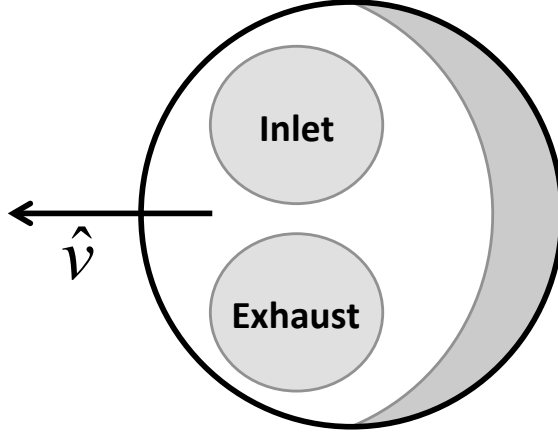
Figure 34: Notional diagram of the inlet and exhaust placement in relation to the vehicle velocity vector

In the equation, $\dot{m}$ is the mass flowrate, v is the velocity, the subscript ox denotes properties of the oxidizer, subscript f denotes properties of the fuel, subscript $inlet$ denotes properties of the engine inlet, and subscript $exit$ denotes properties of the nozzle exit. A unit vector, denoted as $\hat{v}$, is oriented in the direction of the vehicle velocity vector, shown in Figure 34. The convention is $\dot{m}$ positive for ingestion and positive vector quantities in the direction of the vehicle velocity vector, $\hat{v}$. As a result, all terms in Eq. 34 are negative (in the drag direction) due to all $\dot{m}_{exit}$ and v_{inlet} values being negative.

$$
\begin{aligned}
\vec{F}_{int} &= \dot{m}\Delta v \\
&= \dot{m}_{ox,inlet}(v_{inlet} - 0)\hat{v} + \dot{m}_{ox,exit}(v_{exit} - 0)\hat{v} + \dot{m}_{f,exit}(v_{exit} - 0)\hat{v} \quad (34) \\
&= (\dot{m}_{ox,exit} + \dot{m}_{f,exit})v_{exit}\hat{v} + \dot{m}_{ox,inlet}v_{inlet}\hat{v}
\end{aligned}
$$

The external vehicle forces are described in Eq. 35, which includes the traditional definition of aerodynamic drag in addition to the pressure modification terms to account for the presence of the inlet and exhaust. In the equation, C_D is the drag coefficient, A is the area, q is the dynamic pressure, P is the pressure, the subscript ref denotes a reference quantity, and the subscript ∞ denotes the properties of the

freestream.

$$\vec{F}_{ext} = -C_D A_{ref} q_\infty - (P_{inlet} - P_\infty)A_{inlet} - (P_{exit} - P_\infty)A_{exit} \tag{35}$$

The net force on the vehicle, the sum of F_{int} and F_{ext}, is shown in Eq. 36. The first group of terms describes the propulsion system performance, the second group describes the inlet drag terms, and the third describes the aerodynamic drag. It is important to note that, in the case of $(P_{inlet} - P_\infty) > 0$ and $(P_{exit} - P_\infty) > 0$, all terms are negative and, as a result, contribute to deceleration of the vehicle. This observation highlights one of the unique advantages of an atmospheric-breathing retropropulsion vehicle over traditional forward-propulsion vehicles, that large inlet drag and other parasitic forces, which are typically undesirable, instead improve deceleration capabilities of the retropropulsion engine.

$$\vec{F}_{net} = \left((\dot{m}_{ox,exit} + \dot{m}_{f,exit})v_{exit}\hat{v} - (P_{inlet} - P_\infty)A_{inlet} \right)$$
$$+ \left(\dot{m}_{ox,inlet}v_{inlet}\hat{v} - (P_{exit} - P_\infty)A_{exit} \right) \tag{36}$$
$$- C_D A_{ref} q_\infty$$

3.3.4.2 Realistic Engine Expansion

The expansion ratio of the engine significantly impacts engine performance and sizing. Perfectly expanded engines, while favorable from a performance standpoint, are often not feasible due to the freestream pressure variation throughout the trajectory as well as practical limits on the the nozzle area. Due to the low atmospheric pressure on Mars, most propulsion systems will be underexpanded. As a result, it is important to characterize the effects of the underexpansion on the propulsion system performance.

The engine expansion calculations relied on the propulsion tables formulated in terms of the combustion and expansion pressures. Example data of the engine I_{SP} and $\dot{m}/A$ versus combustion and expansion pressure are shown in Figure 35 for constant pressure combustion with an oxidizer-to-fuel ratio of 4.

(a) I_{SP} results (in seconds)

(b) $\dot{m}/A$ results (in $kg/m^2 s$)
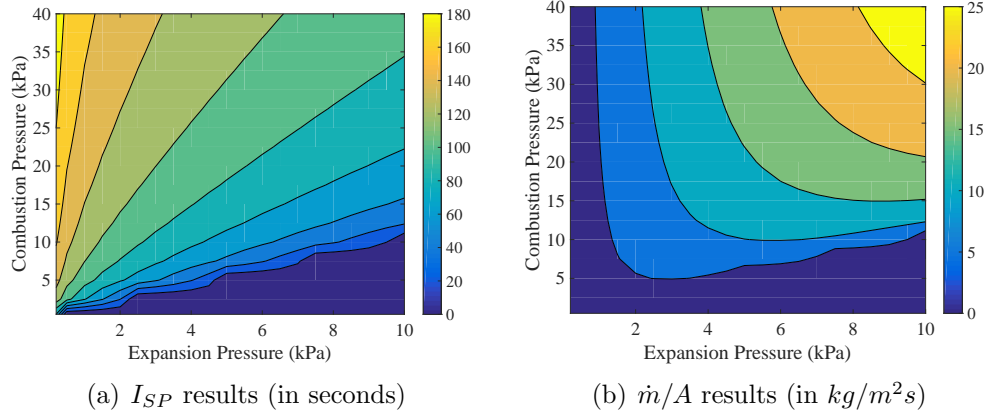
Figure 35: Equilibrium combustion simulation results of a constant pressure ABSRP engine at $OF = 4$

The combustion and expansion pressure limits used in the propulsion performance mapping were chosen to bound the complete combustion environment that could be experienced during the trajectory. As a result, it was understood that certain pressure combinations, such as those where the expansion pressure was higher than the combustion pressure, would result in unrealistic behavior. In particular, many of the pressure combinations simulated impractical subsonic expansion solutions. By sweeping over the expansion pressure, the combustion calculations enabled the identification of the mixture choke conditions, which allowed for the isolation of favorable supersonic expansion cases. The choke identification routine was based on the fact that, for a given set of engine parameters and flight environment, the combustion pressure would be specified. As a result, the expansion pressure and engine cross-sectional area were related through the $\dot{m}/A$ curve at constant combustion pressure. Because the engine would run in steady state, there would be no accumulation term and the propellant $\dot{m}$ through all stages of the engine would be constant. Therefore, the $\dot{m}/A$ curve represented the variation in the inverse of the engine cross-sectional area, $1/A$. The engine throat, the location of minimum cross-sectional area, would therefore be identified as the maximum $\dot{m}/A$ value on the curve. All solutions for

90

lower expansion pressures (to the left) were valid supersonic flow solutions and all so-
lutions for higher expansion pressures (to the right) were the subsonic flow solutions,
which were discarded. The resulting graphs of the I_{SP} and $\dot{m}/A$ versus combustion
and expansion pressure, which isolated the valid supersonic flow solutions, are shown
in Figure 36.

(a) I_{SP} results (in seconds)

(b) $\dot{m}/A$ results (in $kg/m^2 s$)
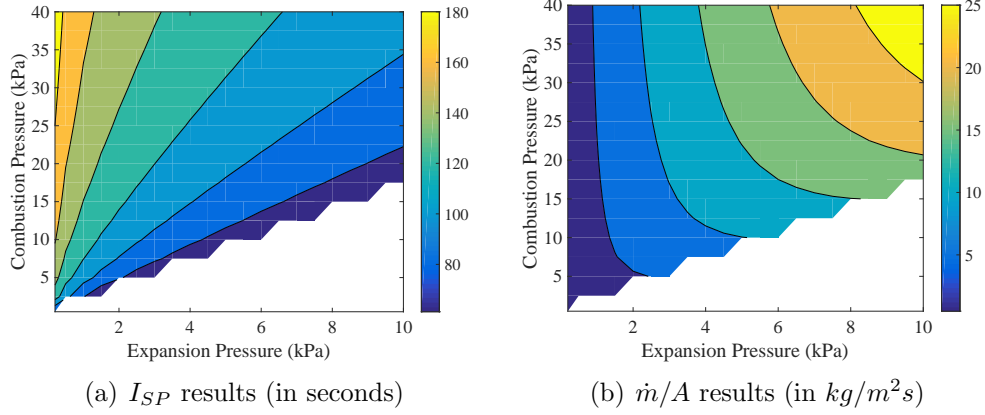
Figure 36: Equilibrium combustion simulation results of a constant pressure ABSRP
engine at $OF = 4$ isolating the supersonic flow solutions

The propulsion system thrust is defined in Eq. 37. Both terms, I_{SP} and $\dot{m}$, can
be calculated based on the combustion and expansion pressure.

$$\vec{F}_T = g_e I_{SP} \dot{m}_{exit} \tag{37}$$

While the combustion pressure is a unique function of the propulsion system param-
eters and flight environment, the expansion pressure cannot be directly calculated
because it is linked to the mass flowrate through the cross-sectional area. The mass
flowrate can be determined, however, by referencing the throat conditions, which are
known. As a result, the combustion pressure can be determined from the vehicle
design parameters and flight environment, the mass flowrate can be determined from
the $\dot{m}/A$ parameter at the choke conditions, and the expansion pressure can be cal-
culated from the mass flowrate and the geometry of the engine. Finally, the I_{SP} can
be determined from the combustion and expansion pressures, which would specify all

necessary parameters in Eq. 37.

The algorithm to calculate the thrust cannot be directly implemented with the given outputs from the equilibrium propulsion performance data. Instead, a pre-processing routine was added that transformed the $\dot{m}/A$ as a function of combustion and expansion pressure table into an expansion pressure as a function of combustion pressure and $\dot{m}/A$ table. This was accomplished by inverting the $\dot{m}/A$ and expansion pressure axes (z- and x-axes in Figure 36(b), respectively). First, the range of $\dot{m}/A$ values for each compression pressure were collected, along with the full range for the entire map. These two parameters were used to determine the sampling density of the $\dot{m}/A$ axis, with the range at each compression pressure bounding the minimum sampling density and the full range being used to determine the maximum. The final selection of the $\dot{m}/A$ sampling was a compromise of high resolution to be able to capture the edges of the expansion pressure map and computational limits on total data size and the expense of evaluating a large two dimensional map during every trajectory integration step. Based on the full $\dot{m}/A$ range and the sampling density, the new $\dot{m}/A$ axis was determined for use in the expansion pressure map. The map was then populated by isolating the $\dot{m}/A$ data at a given combustion pressure, resampling that data according to the $\dot{m}/A$ axis values for the expansion pressure map, and then interpolating the original expansion pressure axis based on the corresponding resampled $\dot{m}/A$ values. Any $\dot{m}/A$ data outside of the isolated data range was ignored because it was either a subsonic flow solution or was outside the original combustion and expansion mapping ranges. This process was repeated for each value of the combustion pressure until the entire expansion pressure map was filled. This inversion algorithm is not valid for general maps, but was possible in this case because of the earlier process to remove all of subsonic flow solutions. As a result, all multivalued expansion pressure as a function of $\dot{m}/A$ data was removed, which left a one-to-one mapping of the expansion pressure and $\dot{m}/A$ values at a given combustion pressure.
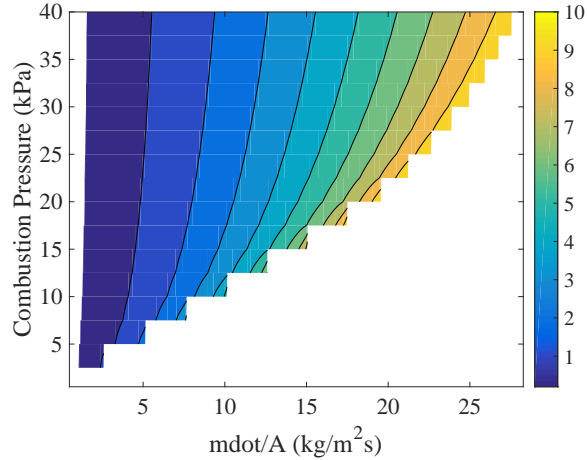
Figure 37: Expansion pressure map (in kPa) based on the equilibrium combustion simulation results of a constant pressure ABSRP engine at $OF = 4$

An example of the resultant expansion pressure map as a function of combustion pressure and $\dot{m}/A$ is displayed in Figure 37.

As mentioned previously, the inversion process truncates data along the edge of the map due to imperfect sampling. As a check, the inversion process was performed again to reformulate the original $\dot{m}/A$ as a function of combustion and expansion pressure map. A high sampling rate was utilized in the reformulation step in order to minimally affect the results. Both the original and reformulated $\dot{m}/A$ maps are shown in Figure 38. In this example, the inversion algorithm sampled the x-axis for the expansion pressure map at ten times the resolution of the original $\dot{m}/A$ map x-axis. The reformulated map is missing a small strip of data along the lower expansion pressure limit of the map (which is not resolved in this image) and a more significant section along the high expansion pressure limit. It is important to note that even the peaks of the sawtooth-like function seen in the reformulated map are recessed from the boundary of the original map.

3.3.4.3 Propulsion System Performance Calculations

The thrust and mass flowrate parameters used for the POST propulsion inputs were based on the propulsion system performance maps, described in section 3.3.4.2, with

(a) Original $\dot{m}/A$ map (in $kg/m^2 s$)

(b) Reformulated $\dot{m}/A$ map (in $kg/m^2 s$) generated from inverted expansion pressure map
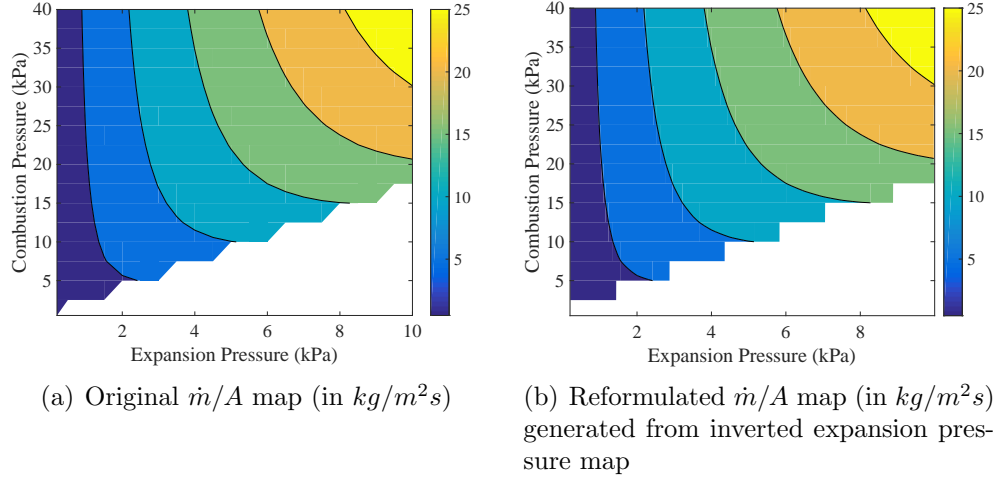
Figure 38: $\dot{m}/A$ maps as a function of combustion and expansion pressure for a constant pressure ABSRP engine at $OF = 4$ with isolated supersonic flow solutions

inputs of the instantaneous freestream conditions and the specified vehicle parameters. A series of calculations were performed during each trajectory integration step in order to transform the vehicle trajectory state into usable metrics for use in the propulsion system mapping and to convert the mapping results into the POST inputs. The calculations assume that a normal shock stands in front of the vehicle during hypersonic and supersonic descent, as is typically seen with the blunt body entry vehicles used in EDL. Future studies with better estimates of the vehicle configuration can adjust this assumption to account for the reduced total pressure loss of oblique shock compression. When traveling at supersonic speeds, all freestream oxidizer being ingested by the vehicle is assumed to first pass through the shock. The oxidizer pressure on the aft-side of the shock is calculated from Eq. 38, with M being the Mach number, P being the pressure, γ being the oxidizer specific heat ratio, the subscript ∞ denoting properties of the freestream, and the subscript PS denoting properties of the post-shock region.

$$P_{PS} = P_\infty \left(\frac{2\gamma M_\infty^2 - (\gamma - 1)}{\gamma + 1} \right) \tag{38}$$

The aft-shock mach number is calculated via Eq. 39.

$$M_{PS} = \sqrt{\frac{(\gamma - 1)M_\infty^2 + 2}{2\gamma M_\infty^2 - (\gamma - 1)}} \tag{39}$$

After being compressed by the bowshock, the oxidizer is ingested and compressed by the inlet, idealized as an isentropic process. The retropropulsion engine then needs to reverse the flow direction and redirect it back out the front of the vehicle. Stagnation of the flow prior to redirection allows for a pressure rise in the oxidizer, which improves combustion performance, and also transfers the oxidizer momentum to the vehicle, improving drag performance. Therefore, stagnation of the oxidizer stream is assumed following ingestion and inlet compression. This process is also modeled as being isentropic. The post-stagnation pressure, P_{stag}, is calculated as in Eq. 40. In the equation, the subscript *stag* denotes a post-stagnation property.

$$P_{stag} = P_{PS}\left(1 + \frac{\gamma - 1}{2}M_{PS}^2\right)^{\frac{\gamma}{\gamma - 1}} \tag{40}$$

Following stagnation, the oxidizer is compressed by an on-board compression system, described in Eq. 41. The oxidizer is later combusted at the post-compression pressure, which is therefore denoted P_{comb}. In the equation, the variable PR refers to the pressure ratio across the compressor. In addition to being a specified performance parameter of the engine, the pressure ratio parameter can also be used to compensate for non-ideal operation of the engine, accounting for the effects of anisentropic inlet compression and stagnation, for example.

$$P_{comb} = P_{stag}PR \tag{41}$$

The bowshock also produces a corresponding temperature rise, the temperature ratio across the shock being defined in Eq. 42. In the equation, TR refers to the temperature ratio and the subscript PS is used to denote the property across the shock.

$$TR_{PS} = \frac{\left(\left((\gamma - 1)M_\infty^2 + 2\right)\left(2\gamma M_\infty^2 - (\gamma - 1)\right)\right)}{(\gamma + 1)^2 M_\infty^2} \tag{42}$$

The mach number ratio across the shock, denoted MR, is calculated in Eq. 43.

$$MR_{PS} = \frac{M_{PS}}{M_\infty} \tag{43}$$

The post-shock velocity, for use in the ram drag calculation, is defined in Eq. 44.

$$v_{PS} = v_\infty \sqrt{TR_{PS}} MR_{PS} \tag{44}$$

The ingested oxidizer mass flowrate is defined in Eq. 45. In the equation, ρ is the density and A_{inlet} is the inlet area.

$$\dot{m}_{inlet} = \rho_\infty v_\infty A_{inlet} \tag{45}$$

Two different parameters constrain the mass flowrate of propellant through the engine. The first, described in Eq. 46 and denoted by $\dot{m}_{exit,aero}$, is that the mass flowrate of propellant is limited by the amount of oxidizer ingested. The second, described in Eq. 48 and denoted by $\dot{m}_{exit,eng}$, is that the mass flowrate of propellant is limited by the choke point of the engine. Therefore, the actual mass flowrate is the minimum of the two, defined in Eq. 49. During instances where $|\dot{m}_{exit,aero}| > |\dot{m}_{exit,eng}|$, the excess oxidizer spills around the inlet and passes around the vehicle instead of being ingested. The added drag from the spillage is not accounted for in the model. During instances where $|\dot{m}_{exit,aero}| < |\dot{m}_{exit,eng}|$, it is assumed that choked flow is maintained through a pintled nozzle or other mechanism. The variation in expansion ratio and efficiency considerations however, are not modeled. In Eq. 47, $\dot{m}/A|_{choke}$ is the value of $\dot{m}/A$ at the choke point, interpolated from the equilibrium combustion results based on the current value of P_{comb}. The variable OF is the oxidizer to fuel ratio, A_{exit} is the exit area, and ER is the expansion ratio. The negative sign is based on the convention that mass ingestion is a positive $\dot{m}$.

$$\dot{m}_{exit,aero} = -\dot{m}_{inlet} \frac{OF + 1}{OF} \tag{46}$$

$$\left. \frac{\dot{m}}{A} \right|_{choke} = f(P_{comb}) \tag{47}$$

$$\dot{m}_{exit,eng} = \frac{\dot{m}}{A}\bigg|_{choke} \frac{A_{exit}}{ER} \tag{48}$$

$$\dot{m}_{exit} = -\min(|\dot{m}_{exit,aero}|, |\dot{m}_{exit,eng}|) \tag{49}$$

The expansion pressure, P_{exp}, is obtained by interpolating the expansion pressure map based on the current values of P_{comb} and $\dot{m}/A$, seen in Eq. 51. The $\dot{m}/A|_{exit}$ value is calculated based on the exit $\dot{m}$ and the exit area, shown in Eq. 50.

$$\frac{\dot{m}}{A}\bigg|_{exit} = \frac{\dot{m}_{exit}}{A_{exit}} \tag{50}$$

$$P_{exp} = f\left(P_{comb}, \frac{\dot{m}}{A}\bigg|_{exit}\right) \tag{51}$$

For the last of the intermediate calculations, the engine I_{SP} is determined by interpolating the equilibrium combustion results based on the current combustion and expansion pressures, as in Eq. 52.

$$I_{SP} = f(P_{comb}, P_{exp}) \tag{52}$$

Four separate engines were used to model the different forcing terms, with POST requiring that the thrust and either the propellant mass flowrate or the I_{SP} be specified for each engine. The inlet was modeled as to ingest the atmospheric oxidizer, shown in Eq. 53, and experience the ram drag forcing, described in Eq. 54. In the equations, T is the thrust and the subscript $ramdrag$ denotes properties of the modeled ramdrag engine. The inlet forcing is negative due to $\dot{m}_{exit}$ being negative.

$$\dot{m}_{ramdrag} = -\dot{m}_{exit}\frac{OF}{OF+1} \tag{53}$$

$$T_{ramdrag} = v_{PS}\dot{m}_{exit}\frac{OF}{OF+1} \tag{54}$$

The second engine modeled the retropropulsive thrust from the ABSRP nozzle, calculated via Eq. 56, with efficiency determined based on the equilibrium combustion modeling, shown in Eq. 55. In the equations, g_e is the acceleration due to gravity

on earth and the subscript $ABSRP$ denotes the properties of the modeled ABSRP nozzle.

$$I_{SP,ABSRP} = I_{SP} \tag{55}$$

$$T_{ABSRP} = g_e I_{SP} \dot{m}_{exit} \tag{56}$$

The final two engines modeled the pressure correction terms for both the inlet and exhaust, shown in Eqs. 57 and 59, respectively. Because these two engines do not model physical components, the mass flowrate parameters are arbitrary. As a result, the mass flowrate values of each engine were set to an arbitrary constant of opposite sign in order to avoid unwanted mass loss or accumulation, set in Eqs. 58 and 60. In the equations, the subscript $inletP$ denotes the inlet pressure correction engine and the subscript $exitP$ denotes the exhaust pressure correction engine. The negative sign is used to denote a decelerative term.

$$T_{inletP} = -(P_{PS} - P_{\infty})A_{inlet} \tag{57}$$

$$\dot{m}_{inletP} = +constant \tag{58}$$

$$T_{exitP} = -(P_{exp} - P_{\infty})A_{exit} \tag{59}$$

$$\dot{m}_{exitP} = -constant \tag{60}$$

3.3.4.4 Impulsive Maneuver Model

The impulsive maneuver model was used to determine the propellant mass required to negate the residual delta-v following ABSRP descent. The first step was to determine the impulsive engine performance. The impulsive model for the ABSRP-based engine calculated the engine thrust and propellant flowrate based on the impulsive storage tank pressure and the atmospheric-breathing performance data generated from the equilibrium combustion calculations. The model assumed that the engine was capable of maintaining the initial tank pressure within the combustion chamber for the

duration of the maneuver. The thrust for rocket-based impulsive maneuvers was directly input into the simulation and the propellant flowrate was calculated from the thrust and I_{SP} values.

The impulsive delta-v calculations accounted for the effects of acceleration due to gravity in an effort to penalize low-thrust maneuvers that would, in reality, require significant time to complete. This also ensured that impulsive maneuvers with a thrust-to-weight less than one were not considered. Due to the simplifications inherent in the impulsive calculations however, any associated altitude and drag losses were not modeled.

The gravity and exit pressure correction terms were added into the rocket equation by equating the rate of change of momentum with the applied forces, as shown in Eq. 61. In the equation, m is the vehicle mass, v is the vehicle velocity, v_{exit} is the velocity of the exhaust mixture, A_{exit} is the area of the nozzle, P is the pressure, and g is the acceleration due to gravity on Mars.

$$m\dot{v} - \dot{m}v_{exit} = A_{exit}(P_{exp} - P_\infty) - gm \tag{61}$$

Equation 61 could be reformulated as in Eq. 62, with the effective velocity, v_{eff}, defined in Eq. 63.

$$m\dot{v} = \dot{m}v_{eff} - gm \tag{62}$$

$$v_{eff} = v_{exit} + \frac{A_{exit}}{\dot{m}}(P_{exp} - P_\infty) \tag{63}$$

The resultant vehicle acceleration, described in Eq. 64, was then integrated to produce the modified rocket equation, shown in Eq. 65. The effective I_{SP} variable, $I_{SP,eff}$, is defined in Eq. 66. In the equations, g_e refers the the acceleration due to gravity on earth.

$$\dot{v} = \frac{\dot{m}}{m} v_{eff} - g \tag{64}$$

$$\Delta v = g_e I_{SP,eff} \log\left(\frac{m_{initial}}{m_{final}}\right) - g\Delta t \tag{65}$$

$$I_{SP,eff} = I_{SP} + \frac{A_{exit}}{g_e \dot{m}}(P_{exp} - P_\infty) \tag{66}$$

The maneuver duration, Δt is defined based on the consumed propellant mass and mass flowrate, as shown in Eq. 67. Therefore, the rocket equation could be expressed as Eq. 68. In the equation, m_{prop} refers to the impulsive propellant mass and the convention is to take $\dot{m}$ as positive. It is important to note that this definition of the impulsive delta-v neglected losses due to residual, unusable propellant.

$$\Delta t = \frac{m_{prop}}{\dot{m}} \tag{67}$$

$$\Delta v = g_e I_{SP,eff} \log\left(\frac{m_{final} + m_{prop}}{m_{final}}\right) - g\frac{m_{prop}}{\dot{m}} \tag{68}$$

An impulsive map was generated for use in targeting during the vehicle simulations. This was necessary in order to allow for the calculation of the impulsive propellant mass based on the impulsive delta-v because Eq. 68 is not analytically invertible. Due to the competing effects of the propulsive thrust and gravity terms, the graph of delta-v as a function of propellant mass achieved a maximum at a single propellant mass value, as shown in Figure 39. Utilizing less propellant resulted in less delta-v due to the reduced total available impulse of the engine; whereas, carrying more propellant resulted in less delta-v due to the corresponding increase in vehicle weight. In order to avoid the multi-valued mapping of delta-v to propellant mass, the maximum point was calculated for use in truncating the valid propellant mass
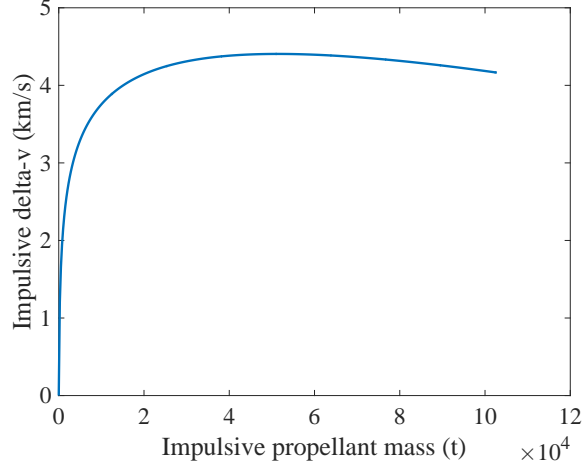
Figure 39: Example graph of the delta-v available as a function of the propellant mass consumed for the impulsive maneuver.

domain. The propellant mass at maximum delta-v was calculated by taking the first derivative of Eq. 68 with respect to propellant mass, shown in Eq. 69.

$$\frac{\delta \Delta v}{\delta m_{prop}} = g_e I_{SP,eff} \frac{m_{final}}{m_{final} + m_{prop}} \frac{1}{m_{final}} - \frac{g}{\dot{m}} \tag{69}$$

Note that the existence of a zero is guaranteed because Eq. 69 is a monotonically decreasing function with a range of $\left\langle \infty, \frac{-g}{\dot{m}} \right\rangle$ over the valid domain of m_{prop}, $\langle -m_{final}, \infty \rangle$. The maximum is guaranteed because the second derivative of Eq. 68 with respect to propellant mass is strictly negative, as shown in Eq. 70.

$$\frac{\delta^2 \Delta v}{\delta m_{prop}^2} = \frac{-g_e I_{SP,eff}}{(m_{final} + m_{prop})^2} \tag{70}$$

The propellant mass at maximum delta-v, $m_{prop,vmax}$ is found by setting Eq. 69 equal to zero and solving for m_{prop}, resulting in Eq. 71.

$$m_{prop,vmax} = \dot{m} I_{SP,eff} \frac{g_e}{g} - m_{final} \tag{71}$$

A check was performed on the sign of $m_{prop,vmax}$ to ensure a valid maneuver. Given the existence of the solution zero delta-v at zero propellant mass and the guarantee of a maximum, any solution with $m_{prop,vmax} > 0$ resulted in a positive maximum

101

delta-v. All solutions with $m_{prop,vmax} < 0$ were deemed unfeasible due to insufficient thrust. While highly unlikely to occur due to the underexpansion of the impulsive engines, it is mathematically possible for $I_{SP,eff}$ to be negative from a large difference between P_∞ and P_{exp}. In this case, the guarantee of the maximum breaks down. No additional checks are required, because the resulting propellant mass at maximum delta-v, calculated from Eq. 71, is negative and is caught by the aforementioned condition. It is also important to note that, in the event of P_∞ being much larger than P_{exp} for any realistic engine, the flow out the nozzle of the engine would separate and would significantly degrade the thrust performance.

The impulsive map was then populated by generating an array of propellant mass values from the domain of zero to $m_{prop,vmax}$ and calculating the corresponding delta-v using Eq. 68.

3.3.4.5 Mass Models

Comparable ABSRP-Only and Rocket-Impulsive simulations could possibly have the same propellant consumption with radically different vehicle masses. As a result, basing vehicle comparisons off the propellant mass alone could lead to misleading results. Instead, the overall vehicle mass was used as the vehicle performance metric, defined as being the sum of all non-payload components and propellant (alternatively, the total entry mass minus the payload mass). In order to make such a comparison, it was necessary to size the vehicle component masses in order to understand their contributions to the vehicle total mass.

Due to the fact that detailed component mass breakdowns are not available during conceptual design, a "size-as-you-fly" methodology was implemented, which assumed a vehicle dry mass and simulated the vehicle trajectory. Individual component masses were then retroactively calculated based on metrics derived from the resulting trajectory. The payload mass for the vehicle is the resulting dry mass available after

subtracting out the mass for each component. It is important to note that this methodology did allow for negative payload mass results. These vehicles would correspond to unfeasible solutions, where the vehicle was too heavy to land itself. This methodology did however, remove the need for multiple convergence iterations for each mass component and, as a result, drastically improved computational efficiency.

A number of mass relationships are available to size the various components. Most sizing equations were either generated from regressions based on historical vehicle mass data, engineering rules of thumb that estimated the component mass fractions, or a combination of both. Previous application of the "size-as-you-fly" methodology, and the associated mass relations, showed it to have reasonable agreement with higher fidelity mass modeling of an MSL-class vehicle with a payload mass of around 1 ton [57, 114]. Comparison with other conceptual design studies of larger human-class payload vehicles showed similar performance [57, 64].

The rocket engine mass relation, shown in Eq. 72, is developed from a regression of conceptual LOX/CH4 engine mass and thrust estimates [64]. In the equation, the rocket engine mass ($m_{eng,rocket}$) units are in kg and the thrust (F_T) units are in N. Neglecting the constant term, this sizing relation equates to an approximate thrust-to-weight of 71.

$$m_{eng,rocket} = 0.00144 F_T + 49.6 \tag{72}$$

The TPS mass relation, shown in Eq. 73, is regressed from historical data of ablative TPS mass fractions versus integrated heat load for a number of United States missions to other planets [115]. In the equation, Q is the integrated heat load in J/cm^2 and m_0 is the entry mass.

$$m_{TPS} = m_0 \big(0.00091 Q^{0.51575} \big) \tag{73}$$

Sizing of the vehicle structure mass, described in Eq. 74, is based on a regression of

structural mass fraction versus dynamic pressure for a number of planetary missions [57]. All data used to generate this relationship was referenced from missions involving blunt entry vehicles. As a result, estimating the structure mass of other vehicle shapes, such as for slender vehicles, requires the use of an additional scaling factor, as shown in Eq. 75. In the equations, q_{max} is the maximum dynamic pressure in Pa experienced during the trajectory and s_{wet} is the wetted area of the vehicle in m^2.

$$m_{struct,blunt} = m_0 \left(0.0232 q_{max}^{0.1708} \right) \tag{74}$$

$$m_{struct,slender} = \left(\frac{s_{wet,slender}}{s_{wet,blunt}} \right)^{1/2} m_{struct,blunt} \tag{75}$$

The backshell mass fraction is estimated based on past Mars robotic missions, with the backshell mass being described in Eq. 76. The backshell mass estimate was similarly developed based on blunt-body vehicles. As a result, a scaling factor is used to extrapolate the results to slender-body configurations, as shown in Eq. 77. In the equation, $s_{backshell,blunt}$ is the backshell area of of the blunt-body vehicle and $(s_{total,slender} - s_{wet,slender})$ corresponds to the non-wetted, or the effective backshell, area, with all areas in m^2.

$$m_{backshell,blunt} = 0.14 m_0 \tag{76}$$

$$m_{backshell,slender} = \left(\frac{s_{total,slender} - s_{wet,slender}}{s_{backshell,blunt}} \right)^{1/2} 0.14 m_0 \tag{77}$$

A reaction control system is assumed for bank angle control during the hypersonic descent phase. The reaction control system (RCS) component mass is assumed to be 0.5% of the entry mass, described in Eq. 78. The RCS is assumed to provide a total delta-v of 30 m/s (ΔV_{RCS}), with an I_{SP} of 200 s. The propellant mass can, therefore, be calculated from Eq. 79.

$$m_{RCS,eng} = 0.005m_0 \tag{78}$$

$$m_{RCS,prop} = \left(1 - \frac{1}{\exp\left(\frac{\Delta V_{RCS}}{g_e I_{SP}}\right)}\right)m_0 = 0.0101m_0 \tag{79}$$

The mass relation for the final component, the ABSRP engine, was not available in the literature. This study attempted to develop a regression equation similar to those used for the other subcomponents. Unfortunately, specific data on the mass and performance of high-speed airbreathing propulsion engines used in missiles or aircraft were severely lacking. Three datapoints were found, containing information on the vehicle thrust and weight [116, 117]. A summary of the engine results is shown in Table 8. The average thrust to weight of the three engines was 19.7, with a total range of 12 to 23. Therefore, a thrust to weight of 20 was assumed in this study for the sizing of all ABSRP engines. The ABSRP engine sizing relation ($m_{eng,ABSRP}$) is shown in Eq. 80.

$$m_{eng,ABSRP} = \frac{F_T}{20g_e} \tag{80}$$

Table 8: Mass and performance data for high-speed airbreathing propulsion engines

	SERJ	RJ-43-MA-11	RJ-43-MA-3
Thrust (N)	142343	53379	51155
Weight (N)		2380	2202
T/W	12-15	22.4	23.2

Additional margin was applied to the mass estimates in order to account for the uncertainty in the mass estimating relationships and the use of extrapolation. A 15% margin was added to the dry mass components and a 10% margin was added to the simulated propellant consumption.

CHAPTER IV

VEHICLE DESIGN ASSESSMENT

4.1   Motivation

Before any comparisons can be made between ABSRP architectures and similar rocket configurations, the vehicles themselves must be understood within the context of their individual design spaces. This is a result of the unique constraints on atmospheric-breathing propulsion systems, where favorable design characteristics of rocket vehicles may not translate to atmospheric-breathing configurations. As a result, conceptual design of ABSRP architectures must consider how individual vehicle design characteristics affect performance of the ABSRP architecture. Exploration of the vehicle design space also allows for the identification of constraints, where given sets of design parameters do not allow for a viable vehicle.

4.2   Vehicle Design Parameters

ABSRP has the greatest application to high mass, human-class missions, where traditional rocket propulsion has been shown to be excessively massive [15, 57]. Past studies have focused on human-class payload masses on the order of 40 t [1, 15, 57]. This requirement was derived from the NASA Design Reference Architecture study in 2009, which subdivided all required surface systems into multiple landings, the largest of which weighed 40 t [55]. More recent assessments have reevaluated the surface elements and packaging, estimating a number of payload alternatives weighing 15, 18, 27, or 40 t [50]. Limited information is available on vehicle performance estimates for these vehicles. As a result, this study chose to target the baseline 40 t payload class, due in part to the ample availability of reference literature studies.

106

Due to the nature of the "size-as-you-fly" methodology, the payload mass value was an output of the simulation instead of a target, with the performance of each vehicle being assessed in terms of the maximum available payload for a given initial mass. As a result, an entry dry mass of 70 t was chosen for the simulations, as it was estimated to result in vehicles in the 40 t payload range.

Given the intent of this study to assess the performance of ABSRP in relation to existing alternatives for human-class Mars missions, entry vehicle models were chosen based on literature data of predicted vehicles [55, 15, 57]. The first vehicle, shown on the left in Figure 40, and referred to in this study as the blunt-body configuration, is a blunt-body entry vehicle with a 70° sphere-cone aeroshell. This vehicle achieves an $L/D = 0.3$ and $C_D = 1.424$. The second vehicle, shown on the right in Figure 40, and referred to as the slender-body configuration, is a mid-L/D aeroshell consisting of a cylindrical segment with a hemispherical cap on one end. This vehicle is assumed to fly at a high angle of attack and, as a result, achieves an $L/D = 0.68$ and $C_D = 1.713$. The slender-body does involve a larger aerodynamic surface area however, which contributes to larger structural and TPS mass fractions. The hypersonic C_D values are also used for the powered descent phases but with the added correction terms for the presence of the inlet and exhaust. Powered descent L/D values are assumed to be zero. The reference areas for both vehicles are based on their common diameter of 10 m, corresponding to reference areas of 79 m^2. As a result, both vehicles are sized with the expectation that future heavy lift launch vehicles will have a shroud diameter of 10 m. Alternatively, previous studies have also hypothesized that either configuration could be mounted on top of the launch vehicle stack during liftoff from Earth.

A certain percentage of the vehicle projected area was allocated to the inlet and exhaust, here taken to be 85 percent. This area was then partitioned between the inlet and exhaust, with the inlet area being chosen up to the total usable area and the
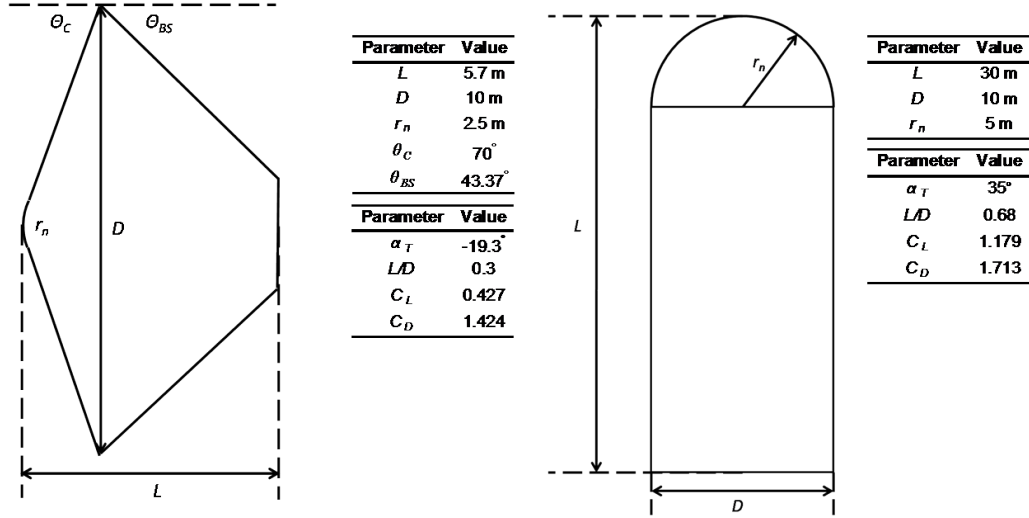
Figure 40: Geometry of vehicle models considered in the study. Left: blunt-body configuration. Right: slender-body configuration. [57]

exit area encompassing the complementary area. The exit and throat areas jointly defined the nozzle geometry. However, instead of varying these coupled parameters in the study, the exit area and expansion ratio were chosen as design variables. This was motivated by the fact that the expansion ratio has a direct relation to the engine efficiency and because it allowed for independent variation of both variables without constraints on the domain. A range of expansion ratios between 1:1 and 40:1 was chosen, motivated by the geometry of existing engines, the low atmospheric pressure on Mars, and the desire to encompass a sufficient range in order to observe the parameter sensitivity.

As observed in Chapter 2, three variables contributed to the majority of the atmospheric-breathing propulsion performance variability - the combustion pressure, expansion pressure, and oxidizer-to-fuel ratio. The expansion pressure is derived from the combustion chamber pressure and the expansion ratio. Knowing the instantaneous flight environment, the combustion pressure input can be reformulated in terms of the pressure ratio across the compressor. Based on the propulsion system performance results, the pressure ratio was allowed to vary between 1 and 50 times

compression. Additional compression was allowed on the stored oxidizer for the impulsive maneuver. Given that the oxidizer would have already been compressed, the pressure ratio for the impulsive oxidizer was varied between 1 and 10 times compression. The oxidizer-to-fuel ratio domain was based on two competing effects. Stoichiometric engines running oxidizer-to-fuel ratios around 2 achieve the highest propulsive cycle efficiency in terms of total propellant usage. Higher oxidizer-to-fuel ratio engines have lower propulsive efficiency, but leverage more of the atmospheric oxidizer and, as a result, have lower fuel usage. The oxidizer-to-fuel ratio domain was therefore restricted to be between 2 and 20, with $OF = 2$ defining the the stoichiometric lower limit and $OF = 20$ leveraging a significant amount of atmospheric oxidizer but combusting with minimal efficiency (I_{SP}).

Configurations involving rocket engines were assumed to have constant thrust between 500 kN and 2000 kN, based on use of existing rocket engines and previous human-scale Mars systems studies. The impulsive thrust for the rocket engine in the Rocket-Only configuration was also allowed to vary independently within this same range. Rocket I_{SP} values were assumed to be 370 s, which was based on a typical liquid oxygen, liquid methane engine [14, 108].

All simulations initiated atmospheric entry at 125 km altitude, 4 km/s velocity, and with a flight path angle of -14.5 degrees (oriented below the horizon). These values were based on entry from a Mars parking orbit, which was assumed in this, and previous studies, to be necessary in order to mitigate risk for the human crew.

As a result, five independent design parameters were allowed to vary for for the ABSRP-Only and Rocket-Impulsive configurations in order to characterize the effects of the atmospheric-breathing propulsion system on the integrated vehicle performance. Four of the five design variables were common between the two configurations

while the fifth was unique to each, allowing for specific tailoring of their differing impulsive maneuvers. Two independent parameters were used for the Rocket-Only configuration, the descent and impulsive thrust, due to the absence of the atmospheric-breathing engine.

4.3   Propulsion System Exploration Study

An initial exploration of the propulsion system performance was conducted to understand if any of the performance metrics could be correlated to easily observable quantities and to understand the relative sensitivities of the performance metrics to the independent design parameters. The intent of the exploration was to determine if reduced order models could be constructed for the propulsion system metrics in order to reduce the design space for the full vehicle study or to see if certain design variables could be neglected due to negligible corresponding variation in the performance metrics. Propulsion system metrics of interest were considered to be parameters that affected the forces on the vehicle but could not be trivially determined from the flight environment characteristics. Based on their contribution to the thrust and pressure differential terms, the propulsion system performance metrics were chosen to be the propellant flowrate, $\dot{m}$, the ABSRP engine I_{SP}, and the nozzle expansion pressure, P_{exp}.

Populating the performance data involved sweeping over ranges of altitude and velocity, simulating a trajectory of infinitely short duration that calculated the propulsion system performance at that flight environment (the flight path angle affected the resulting trajectory but had no correlation to the propulsion system performance). A full factorial design space was used for the flight environment sampling as well as for each of the propulsion system design parameters, which were sampled from prescribed ranges. The propulsion system design parameters, the compression ratio, nozzle exit area, nozzle expansion ratio, and oxidizer to fuel ratio, were chosen based on the

110

inputs to the propulsion systems performance maps. Overall, 36300 datapoints were generated.

An initial investigation was conducted to understand the qualitative sensitivity of the performance metrics with respect to the design parameters. The data was visualized by isolating the results of each performance metric versus specific input variables, such as in Figure 41. The figures show the performance metric on the y-axis versus an arbitrary, randomly sampled x-value between zero and one. The x-value range is used to separate the results and aid in visualization. Individual design variable results were isolated by selecting the color of each datapoint based on the value of the design variable of interest. As a result, easily identified stratification of color would indicate a strong correlation between the design variables and the metric; whereas, a homogeneous distribution of color would indicate poor correlation. The degree of overlap or separation between adjacent input variable values indicated the relative sensitivity of that variable to the overall variation in the data. In this way, the most important design variables could be easily identified, enabling a qualitative understanding of their sensitivity across the entire design space. A successive filtering methodology was used, isolating a given value of the most important variables, which enabled an understanding of the hierarchy and relative weighting of the design variables.

A distinct stratification of the expansion pressure results are seen in Figure 41(b), with minimal overlap between adjacent nozzle expansion ratio designs, whereas much more dispersion is seen in Figure 41(a). This indicates that the expansion ratio parameter contributes to higher variability in the expansion pressure, relative to the other design variables, than in the I_{SP}. Determining the parameters contributing to lower order variability involved isolating the results for a single value of the expansion ratio and replotting the remaining data with respect to the other design variables. This was performed for all metrics to determine the various levels of parameter sensitivities. A summary of the qualitative parameter sensitivity results is shown in Table

111

(a) I_{SP} results (y-axis) from the propulsion system exploration study partitioned based on the nozzle expansion ratio (color).

(b) P_{exp} results (y-axis) from the propulsion system exploration study partitioned based on the nozzle expansion ratio (color).
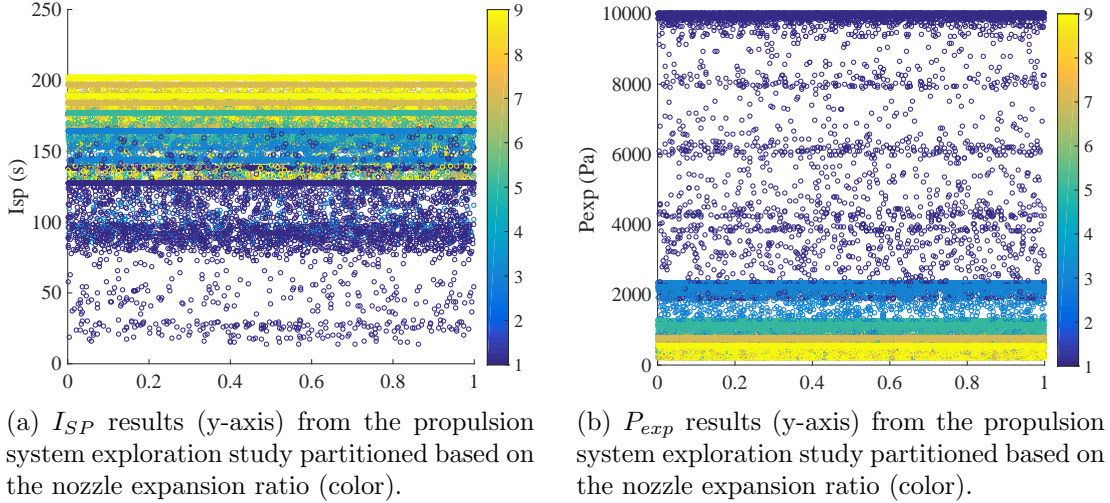
Figure 41: Propulsion system metric results with data partitioned based on the nozzle expansion ratio

9, with Level 1 corresponding to highest correlation and increasing level corresponding to decreasing correlation. While the expansion ratio results in Figure 41 show clear trends, results for higher level parameters became significantly less distinct.

Table 9: Identification of propulsion system design variable parameter sensitivities with respect to the performance metrics. Level 1 corresponds to highest contribution to variability.

Level	I_{SP}	$\dot{m}$	P_{exp}
Level 1	Expansion Ratio	Expansion Ratio	Expansion Ratio
Level 2	OF	Exit Area	OF
Level 3	Pressure Ratio	Pressure Ratio	Pressure Ratio
Level 4	Exit Area	OF	Exit Area

The results indicate that no design parameter is negligible and, thus, all parameters are required in the model. In addition, it is not possible to truncate the input variable domain as the design parameters often have competing effects on different metrics. For example, increasing the nozzle expansion ratio contributes to increased thrust via an improved I_{SP} but also reduced thrust via a lower $\dot{m}$.

Another attempt to reduce the dimensionality of the propulsion system design space was through developing reduced order models of the metrics. The I_{SP}, $\dot{m}$,

112

and P_{exp} results were independently regressed against basis functions derived from the propulsion system design variables and flight environment in order to generate surrogate response surface equations. The 36300 available datapoints from the exploration study allowed for the trial of a number of potential basis function. Linear and quadratic function of the propulsion system design variables, OF, nozzle expansion ratio, nozzle exit area, and compression pressure ratio, were considered. Additional linear and quadratic functions of the instantaneous flight environment parameters, such as the vehicle altitude, velocity, dynamic pressure, freestream density, and post-shock pressure, were also considered. Regressions based on the full basis set were unable to achieve R^2 values above 0.75, indicating poor correlation. This meant that, even with a full knowledge of the vehicle flight environment and propulsion system characteristics, the reduced order models were unable to describe a significant portion of the metric variability. Given the poor R^2 performance coupled with the the need for accurate estimation when used in the vehicle performance study, it was determined that reduced order modeling was not beneficial to continue pursuing.

These results did reinforce the fact that the propulsion system model was truly a non-linear mapping from the flight environment and design parameters to the performance metrics. This study also further motivated the need for a full simulation of the vehicle trajectory's impact on the ABSRP propulsion performance and how the propulsion system, in turn, contributed to the overall vehicle performance.

4.4 Design Space Exploration Study

A design space exploration was conducted for both the ABSRP-Only and Rocket-Impulsive architectures to understand their performance over the full range of vehicle configurations. As discussed in Section 4.2, the inlet and exit areas, nozzle expansion ratio, compression ratio, oxidizer-to-fuel ratio, and the impulsive compression ratio, impulsive engine thrust, or descent engine thrust were sampled from their prescribed

ranges. Trajectories were simulated for vehicles described by the given set of independent parameter values and the results from each configuration were used to assess ABSRP performance for different vehicle designs.

4.4.1 Design Space Exploration Sampling

Design space exploration was conducted using a fractional factorial, latin hypercube design. In latin hypercube designs, each variable is independently sampled with high resolution, in this study taken to be ten times the total number of design variables. The sample values for each variable are then randomly ordered. Data points for the design space are constructed by isolating the first sample value corresponding to each design variable and aggregating them into a set of variables describing a single vehicle configuration, proceeding through the rest of the sample vectors for subsequent configurations. The advantages of this sampling method are that data points are distributed throughout the entire design space and the number of samples grows linearly in the number of design variables. As a result, 50 cases were attempted for each configuration. Many of these cases were shown to be infeasible: only 20 cases for the blunt ABSRP-Only configuration were feasible, 22 cases for the slender ABSRP-Only configuration, 28 for the blunt Rocket-Impulsive configuration, and 50 for the slender Rocket-Impulsive configuration. These results provided valuable information on restricted areas of the design space and the relevant constraints on the design parameters.

4.4.1.1 ABSRP-Only Convergence

The vehicle inlet area was found to be the dominant predictor of convergence for ABSRP-Only architectures. This is because the ABSRP-Only vehicle needs to ingest all of the oxidizer for the impulsive maneuver during descent. As a result, small inlet area vehicles require extended period of oxidizer ingestion and are unable to capture the requisite oxidizer for the impulsive maneuver. This is compounded by the reduced

timeline for atmospheric-breathing descent thrust, which exacerbates the touchdown velocity and impulsive maneuver mass requirements. As a result, no blunt-body configuration converged if the inlet area was below 25 m^2, eliminating more than a third of the allowed range of 1 through 66 m^2. This constraint was found to relax slightly for slender-body vehicles, resulting in non-convergence for vehicles with inlet areas below 22 m^2. The improved convergence for slender-body vehicles is due to the greater lift capabilities of the slender aeroshell, which can target a wider range of ingestion initiation conditions to allow for increased descent timeline.

The remaining parameters had less distinct convergence limits, with the pressure ratio being the only other parameter close to having a strong limit. No convergence was observed for compression ratios below 15 for blunt-body vehicles, with the slender-body configuration enabling convergence of a few configurations within that range. Convergence based on the impulsive compression ratio was poor for values below 2.5 for both the blunt and slender-body vehicles. Higher compression ratios contributed to improved thrust performance due to increased massflow and improved I_{SP}. Therefore, these limits were due to the descent and impulsive engines being unable to negate the entire vehicle velocity.

The oxidizer-to-fuel ratio, while not displaying a distinct cut-off value, did show a clear trend of reduced convergence with increasing oxidizer-to-fuel ratio. While higher oxidizer-to-fuel ratios allowed for lower fuel consumption, they also corresponded to lower efficiency and lower thrust per oxidizer ingested. Because many of the ABSRP-Only trajectories were oxidizer limited, the over-leverage of atmospheric oxidizer was detrimental. This is confirmed by the fact that practically all converging configurations for each oxidizer to fuel ratio were those with the largest inlet areas. Use of the slender-body vehicle, on average, allowed for one additional configuration to converge at each value of oxidizer-to-fuel ratio. This is again due to the slender-body entry vehicle being able to target initiation conditions with improved timeline and

the larger inlet areas allowing for more oxidizer ingestion.

The nozzle expansion ratio parameter exhibited a non-linear convergence criteria, demonstrating difficulties with convergence for both high and low values. Blunt-body vehicles would not converge for expansion ratios below 4. Slender-body vehicles allowed for the convergence of a single configuration within that limit, with an expansion ratio of 1.2. Slender-body vehicles, conversely, exhibited difficulty converging for expansion ratios above 30, whereas a few blunt-body vehicle were observed to converge within that limit. For a given exit area, small expansion ratio engines allowed for a large mass flow, as well as corresponding large oxidizer and fuel consumption and low efficiency. The combination of large oxidizer consumption and low efficiency contributed to larger impulsive maneuver propellant requirements, which were harder to meet with the given descent timelines. Large expansion ratio engines, conversely, had low propellant usage but also low thrust performance. This reduced the performance of the descent and impulsive maneuvers, contributing to larger touchdown velocities and larger impulsive propellant requirements. It is interesting to note that, of the configurations near the expansion ratio extremes that did converge for both vehicle types, the vast majority of them had large compression ratios around or above 40. The improved compression compensated for the low thrust, large expansion ratio configurations. For the single configuration that converged with small expansion ratio and high compression ratio, as evidenced by the smaller propellant usage, the combination of both parameters enabled delayed propulsive initiation, while still meeting the target requirements.

In all of these results it is important to note the distinction between the convergence and non-convergence regions described above. Regions of non-convergence are defined by segments of the design space where no vehicle configurations converge (with the exception of a few converged case, specifically noted above). All designs do

not converge, however, in the complementary regions. Instead, convergence and non-convergence in these regions is characterized as being mixed, with both converged and non-converged cases distributed within the space. Therefore, parameter constraints are defined as being the boundary between regions of strict non-convergence and regions of mixed convergence.

4.4.1.2 Rocket-Impulsive Convergence

It is evident from the relative number of converged cases that the Rocket-Impulsive architecture is much more robust than the ABSRP-Only. Given that the ABSRP descent engine is the same for both vehicles, the differences arise from the use of the rocket engine for the impulsive maneuver and the elimination of the ingestion phase from the descent trajectory. It was observed that the rocket engine was able to provide higher total impulsive delta-v than the atmospheric-breathing engine. However, because it did not leverage the atmospheric oxidizer, this came at the expense of higher propellant requirements. The biggest factor contributing to the improved convergence is most likely the removal of the ingestion phase. It was observed in the ABSRP-Only architectures that the inability to ingest sufficient oxidizer fast enough, and its compounding effect on the descent timeline, significantly hindered convergence. For these cases, the ingestion phase was excessively long and limited the impulsive maneuver capabilities. The use of a rocket engine decouples the descent and impulsive maneuvers, adding timeline for atmospheric-breathing descent and eliminating the constraints on the available impulsive delta-v. The combination of these factors allows the rocket engine to compensate for poor atmospheric-breathing performance and the ABSRP engine to compensate for poor rocket thrust.

The impulsive engine thrust was determined to be the dominant parameter for predicting Rocket-Impulsive vehicle convergence. Of the 23 runs that did not converge, all had thrust values below 1310 kN. Convergence with respect to all other

parameters was considered to be mixed, with no distinct grouping of converged and non-converged cases.

All runs converged for Rocket-Impulsive configurations involving slender-body entry vehicles. As a result, is can be seen that the impulsive engine thrust constraint can be mitigated with improved initiation state targeting. For these cases, the improved lift-to-drag of the slender vehicle allows for increased altitude margin and timeline at propulsive initiation. The added timeline enables the descent engine to further decelerate the vehicle to within the capabilities of the impulsive engine.

4.5 Sensitivity Study

Improved vehicle convergence is required in order to assess the configuration parameter sensitivities. Analysis of the ABSRP-Only design space exploration indicated that the inlet area was the primary driver of vehicle convergence. Therefore, a second exploration simulation was conducted that relaxed the constraints on the ABSRP engine inlet area in order to improve convergence and enable the identification of individual parameter sensitivities and vehicle mass trends. The exit area constraint was also relaxed in the study due to its similar restriction on the ABSRP thrust. While the inlet area was not observed to dictate Rocket-Impulsive vehicle thrust, the same parameters were used for both the ABSRP-Only and Rocket-Impulsive sensitivity studies to enable an even comparison. It was also hypothesized that the improved ABSRP engine performance would provide similar benefit as improving the descent timeline, both enabling a lower touchdown velocity. Therefore, the improved AB-SRP performance would potentially enable the consistent convergence observed in the Rocket-Impulsive design study for slender vehicles.

4.5.1 Sensitivity Study Design Space

The sensitivity study employed a different design space sampling approach than the design space exploration study. In an effort to avoid non-converging regions, a nominal

vehicle was chosen in the middle of the design space. Sensitivity to each parameter was studied by sequentially perturbing individual design parameter values away from the nominal in both the positive and negative directions. In this way, the vehicle parameter sampling would avoid the edges of the design space and regions of potential non-convergence.

The vehicle parameter ranges for the sensitivity study were the same as those used in the design space exploration study. The only exception was that the inlet and exit areas were decoupled in order to understand their individual contributions to the vehicle performance and each were allowed to vary within the range of zero to the vehicle frontal area. The nominal vehicle was constructed from the midpoints of each design variable range, with the nominal oxidizer-to-fuel ratio chosen to be 4. Individual variables were perturbed away from the nominal by selecting the minimum value on their range, the maximum value, and an additional value of 1.5 times the maximum. The added value outside the range, while not necessary physical, was intended to explore designs outside of the current feasible domain and assess whether further improvement of the vehicle parameters, through technology infusion or other means, was promising or worthwhile. Given the sensitivity to the inlet and exit areas, the perturbation of the areas in the negative direction was taken to be a value of 10 instead of the minimum of the range (which was set to zero, arbitrarily) and the oxidizer-to-fuel ratio perturbation allowed for values of $OF = 2, 8,$ or 12.

An additional study, referred to as the expanded study, was conducted which further relaxed the constraints on the inlet and exit areas, allowing them to vary between one half and one times the vehicle frontal area (effectively increasing the lower bound, and thus the average value, of the areas). The ranges of all other parameters remained the same. This exploration was used, in conjunction with the original sensitivity study, to further remove the restrictions limiting the atmospheric-breathing thrust and to enable an assessment of the vehicle parameter sensitivities

for both limited and unrestricted ABSRP thrust vehicles.

4.5.2 Performance Metric Discussion

The overall objective of the "size-as-you-fly" methodology is to maximize the available payload mass. For configurations with a given entry mass, this is equivalent to minimizing the vehicle mass, defined as the sum of the component (engine, structure, TPS, backshell, and RCS) and propellant masses or, alternatively, the entry mass minus the payload mass. However, the vehicle models and, in particular, the impulsive propellant convergence required specification of the vehicle dry mass (entry mass minus propellant) instead of the entry mass. As a result, depending on the relative weighting of the propellant mass and component masses for different vehicles, comparisons of the available payload mass and total vehicle mass may not necessary be equivalent due to the differing entry masses. Unfortunately, adding additional convergence on the vehicle entry mass, through a modulation of the prescribed dry mass, was prohibitively expensive as it would require multiple iterations of the entire supersonic performance map.

Instead of adding the entry mass convergence, a single performance metric was developed to provide a consistent comparison of different vehicle designs across the entire design space. In this study, all designs were evaluated based on their payload mass fraction, or the available payload mass divided by the vehicle entry mass (sum of payload, component, and propellant masses), with favorable vehicles being those with high payload mass fraction values. The only caveat with the use of this unified metric was that it potentially masked the natural variation of payload fraction with vehicle scale. Across all of the designs considered, vehicle entry masses were observed to deviate by less than 10% of the average entry mass. Therefore, it was determined that the use of the single payload mass fraction metric did not artificially skew comparisons between different vehicles.

4.5.3 Design Parameter Performance Sensitivities

The primary intent of the sensitivity study was to determine the effects of the different design parameters on the overall vehicle performance. This was useful not only to enable a characterization of optimal vehicle characteristics for use in future design efforts, but also to understand how the introduction of the impulsive rocket engine affected the coupling of the different design parameters.

4.5.3.1 ABSRP-Only Parameter Sensitivities

The full sensitivity results for the ABSRP-Only blunt-body configuration are shown in Figure 42. The graph shows the payload mass fraction results plotted on the y-axis versus all of the simulated vehicle configurations, grouped by variation in each design parameter. The blue curves correspond to configuration results obtained in the nominal sensitivity study; whereas, the red curves correspond to the expanded study, which further relaxed the inlet and exit area constraints. Note that the figure is clipped at a payload fraction of -50%, indicating that any designs below that point have exceedingly poor performance.

Of all of the configurations considered, only three cases did not converge, corresponding to nominal search vehicles with the lowest inlet area, expansion ratio, and compression ratio. The inlet area result was observed in the design space study, with small inlet area vehicles limiting oxidizer ingestion for the impulsive maneuver. The pressure ratio constraint was also observed in the design space study and is alleviated in the expanded study due to the relaxed restrictions on the atmospheric-breathing engine thrust. The expansion ratio constraint was seen with some vehicles in the design study. The low expansion ratio configurations correspond to high thrust engines due to a large propellant mass flow. In the nominal study, the vehicle is unable to ingest sufficient oxidizer to satisfy the impulsive propellant requirements. This restriction is again alleviated in the expanded search, although the corresponding
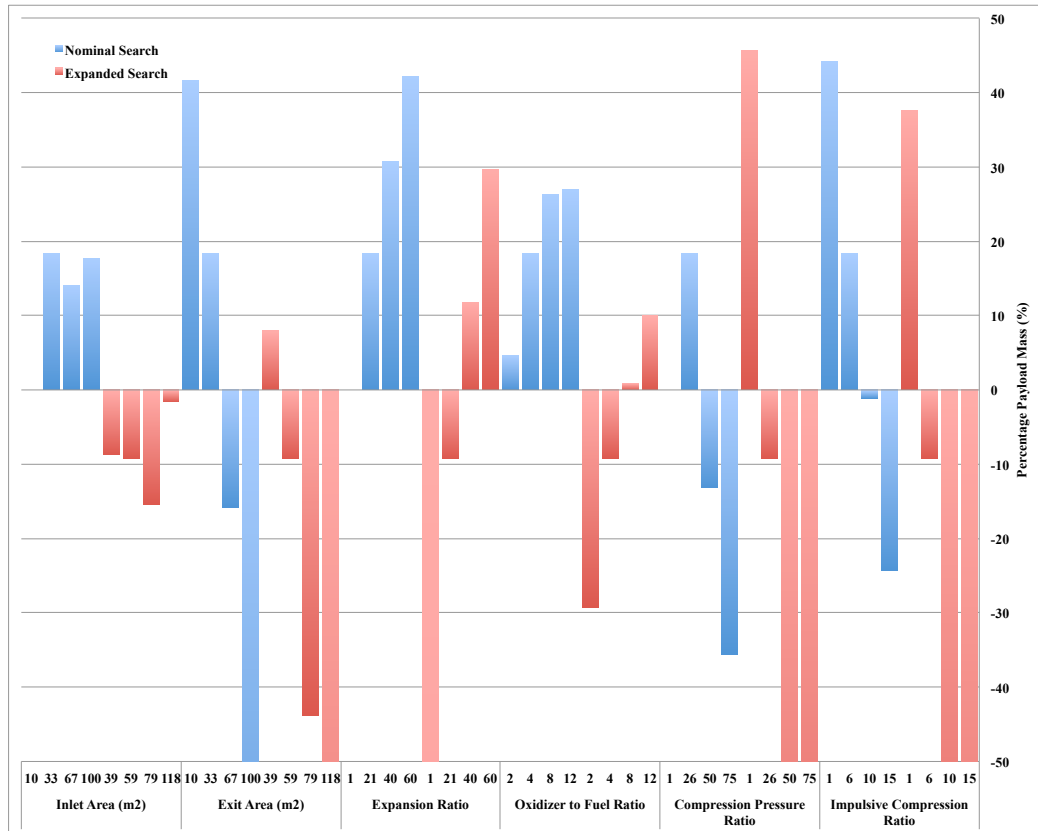
Figure 42: Payload fraction results from the sensitivity study for ABSRP-Only configurations with blunt-body entry vehicles, grouped by variation in the design parameters. Blue curves represent solutions for the nominal search and red curves represent solutions for the expanded search.

expanded search vehicle has very poor payload fraction performance due to its large engine mass.

Despite the inlet area being the dominant contributor to vehicle convergence, it is not observed to be a strong driver of payload fraction performance, with no clear trend in the sensitivity results. The utility of large inlet area vehicles is derived from the need to ingest sufficient oxidizer during descent to fuel the impulsive maneuver. However, above this limit, the inlet area has limited use. This is due to the fact that the engine mass flow rate is limited by both oxidizer ingestion, which is a function of the inlet area, and the choked mass flow rate, which is independent of the inlet area. For vehicles that are constrained by the choked mass flow rate, the inlet area only serves to decrease the required ingestion time. Therefore, the sensitivity results with respect to inlet area reflect the variation in payload performance due to varying staging conditions and the shortened oxidizer ingestion time, which are not observed to be first-order effects.

The payload fraction is seen to be sensitive to the exit area due to its control over thrust performance during the entire trajectory. Payload fraction decreases with increasing exit area for both the nominal and expanded searches due to the increase in engine mass. Payload fraction, conversely, increases for both increasing nozzle expansion ratio and oxidizer-to-fuel ratio, evidenced in both the nominal and expanded searches. The increase in both of these parameters decreases overall thrust but increases fuel efficiency, which contributes to lower engine and propellant mass. The payload fraction displayed an inverse correlation with both the compression pressure and impulsive compression pressure due the decreased engine mass with lower pressurization. However, some compression is needed to maintain adequate thrust levels, as is observed with the non-convergence of the compression pressure equal to one case for the nominal search.

The ABSRP-only slender-body results, shown in Figure 43, have convergence

123

problems for the same configurations, small inlet area, expansion ratio, and compression ratio. The slender-body architecture, in general, shows a significant reduction in payload fraction magnitude across all configurations and also displays nearly identical trends to the blunt-body solutions. The oxidizer-to-fuel ratio trend is slightly obscured for the nominal search. For these cases, the slender-body vehicle enables targeting of initiation states that mitigate the larger engine mass of the low oxidizer to fuel ratio configurations. This is still not possible for the large oxidizer-to-fuel ratio configurations due to their lower thrust values. The expanded simulation increases the exit area of all vehicles, increasing the engine mass of the small oxidizer-to-fuel ratio configurations, but enabling a reduction in engine mass of the large oxidizer to fuel ratio configurations due to the aforementioned favorable staging conditions.
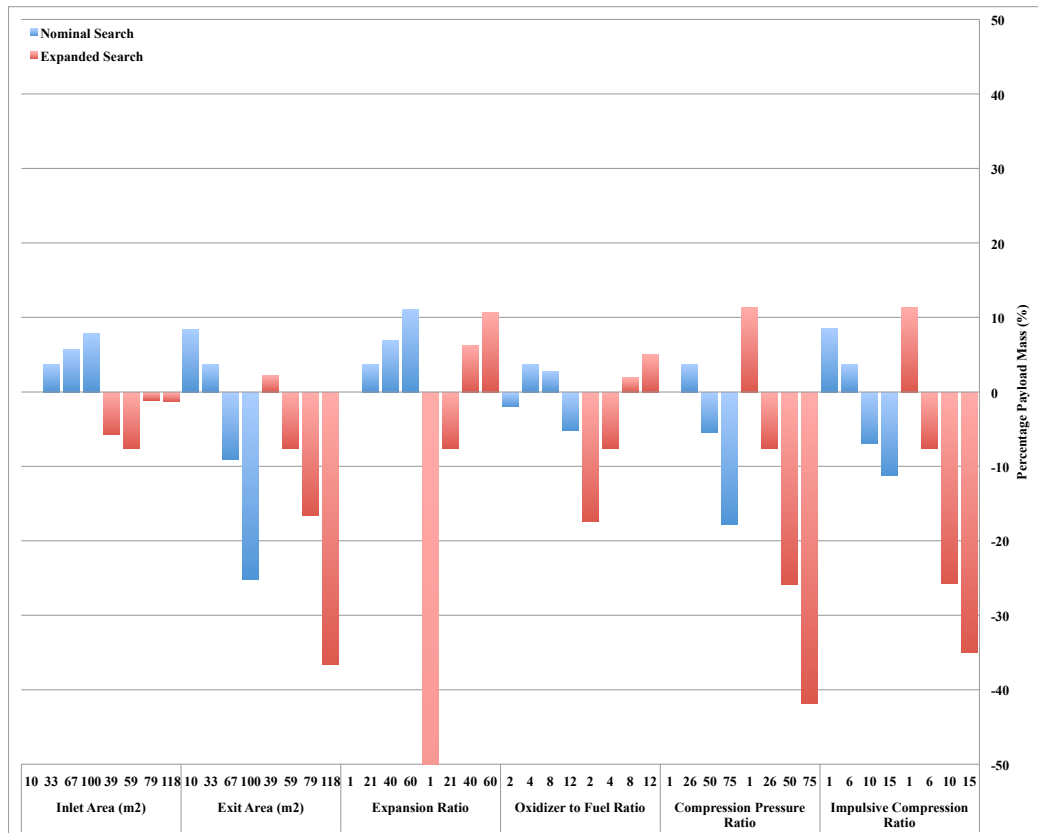
Figure 43: Payload fraction results from the sensitivity study for ABSRP-Only configurations with slender-body entry vehicles, grouped by variation in the design parameters. Blue curves represent solutions for the nominal search and red curves represent solutions for the expanded search.

Overall, it can be seen that optimal ABSRP-Only configurations are characterized by (starting with most payload fraction sensitivity):

1. Small compression ratio

2. Small impulsive compression ratio

3. Small exit area

4. Large expansion ratio

5. Large oxidizer-to-fuel ratio

6. Sufficient inlet area

These characteristics are indicative of low thrust, low propellant consumption designs. The optimal design variable values lie on the extremes of their valid domains and, as evidenced from the convergence results, are often adjacent to non-convergent configurations. This demonstrates that the ABSRP vehicles want to augment the aerodynamic deceleration as little as possible, supplementing only as much as necessary to achieve the desired termination conditions.

4.5.3.2 Rocket-Impulsive Convergence Discussion

The full sensitivity results for the Rocket-Impulsive blunt-body configuration are shown in Figure 44. The figure shows a large discontinuity in the results, with some cases converging to payload fractions on the order of 30% and a number of other cases resulting in payload fractions below -20%. This phenomena is due, in part, to the implementation of the supersonic performance mapping and the particular mass breakdown seen for Rocket-Impulsive architectures.

Robust convergence of the vehicle models required that the supersonic performance map extend to all possible hypersonic touchdown velocities. Unfortunately, supersonic trajectory convergence at the high velocities is impossible, due to the
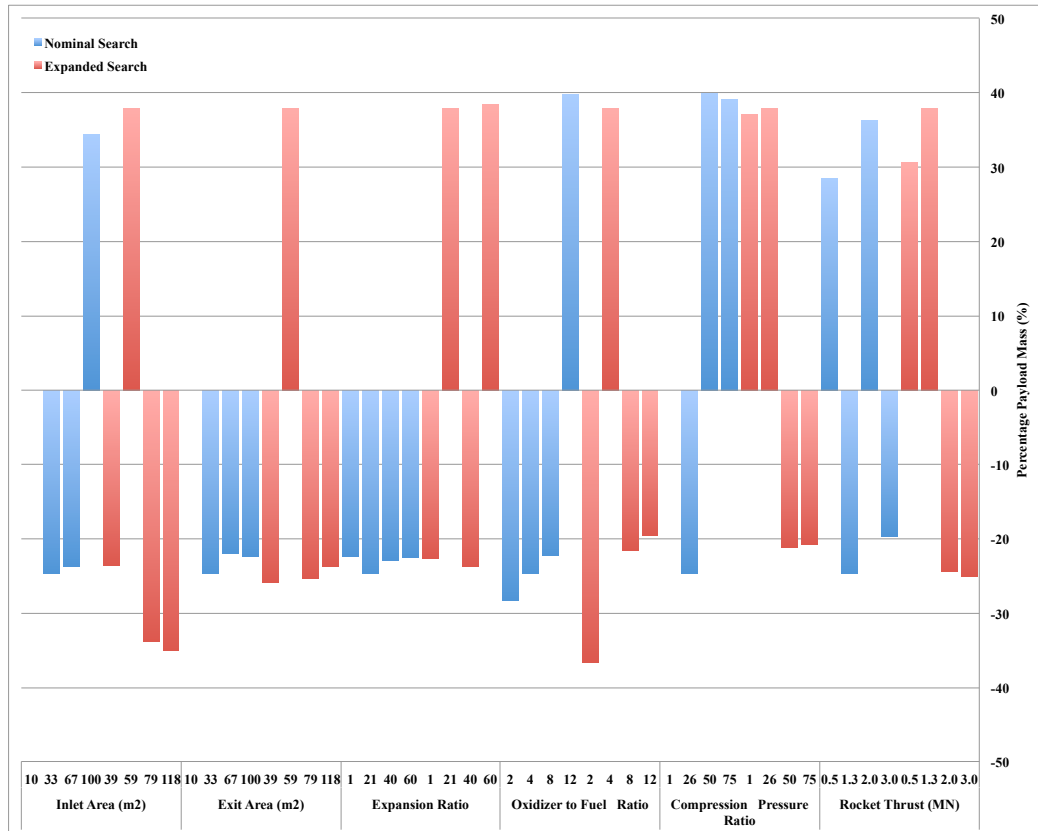
Figure 44: Payload fraction results from the sensitivity study for Rocket-Impulsive configurations with blunt-body entry vehicles, grouped by variation in the design parameters. Blue curves represent solutions for the nominal search and red curves represent solutions for the expanded search.

propellant and engine masses diverging. These solutions were instead generated by extrapolating from results simulated up to a prescribed cutoff velocity.

The extrapolation was designed to be aggressive in order to penalize unfavorable trajectories and drive towards feasible solutions. Consequently, favorable hypersonic trajectories that also intersected the supersonic map above the cutoff velocity over predicted the component mass estimates. The coupling effect of mass and deceleration performance resulted in subsequent targeting to be further up the extrapolation, with the net effect being that the supersonic transition was calculated to be unnecessarily high and with inflated estimates of the vehicle component masses. Despite refinement of the final supersonic trajectory, the excessive initiation velocity distorted the mass results. Additional convergence to further refine the mass estimates was prohibitively expensive and therefore not performed.

The discontinuity in Figure 44 arises from the configurations being unable to target supersonic initiation velocities below the cutoff velocity. The inflated component masses left minimal remainder for the payload, which resulted in very small, or negative, payload fraction values. Fortunately, as evidenced by their inability to target low supersonic initiation conditions, these configurations exhibit poor mass performance and, therefore, do not affect the characterization of the optimal design.

It is interesting to note that a similar discontinuity is not observed for blunt-body ABSRP-Impulsive architectures. This is due to the fact that ABSRP vehicles had lower propellant usage, which enabled targeting of favorable supersonic initial conditions and also avoided the feedback loop of increased mass and reduced deceleration.

4.5.3.3   *Rocket-Impulsive Parameter Sensitivities*

The relaxed constraints on the ABSRP performance for the sensitivity study resulted in a significant improvement in convergence, with only three cases failing to converge

in the nominal search and all cases converging for the expanded search. The non-converged cases corresponded to the configurations with the lowest inlet area, exit area, and compression pressure. It is interesting that convergence was dictated by these ABSRP engine parameters when, in the design space study, the rocket engine thrust was found to dominate convergence. This change is likely due to the improved ABSRP descent performance, where the small inlet and exit areas of the design space study limited the the ABSRP engine thrust and, therefore, placed increasing importance on the impulsive rocket thrust.

While the Rocket-Impulsive convergence challenges did not affect the optimal vehicle design, they did however, make characterization of the performance trends difficult. Convergence was found to be very sensitive to the vehicle parameters due to many of the designs targeting propulsive initiation very close to the cutoff velocity (both above and below). As a result, Figure 44 displays no obvious trends in the parameter sensitivities. When looking at performance variations across the entire design space, it was observed that most of the perturbations had a small effect on the payload fraction results. The one exception was with the rocket engine thrust, with increased thrust corresponding to improved payload fraction performance. The larger thrust values increased the impulsive engine mass, but were compensated by reductions in the descent and impulsive propellant masses as well as the descent engine mass.

The Rocket-Impulsive results for slender-body configurations were unaffected by the convergence problems due to the ability of the mid-L/D aeroshell to target favorable propulsive initiation conditions. It is clear from the sensitivity results presented in Figure 45 that, with the exception of the impulsive engine thrust, the Rocket-Impulsive architecture is largely insensitive to variation in the design parameters. Distinct performance trends are observed, but contribute to less than 5% variability in the payload fraction value.
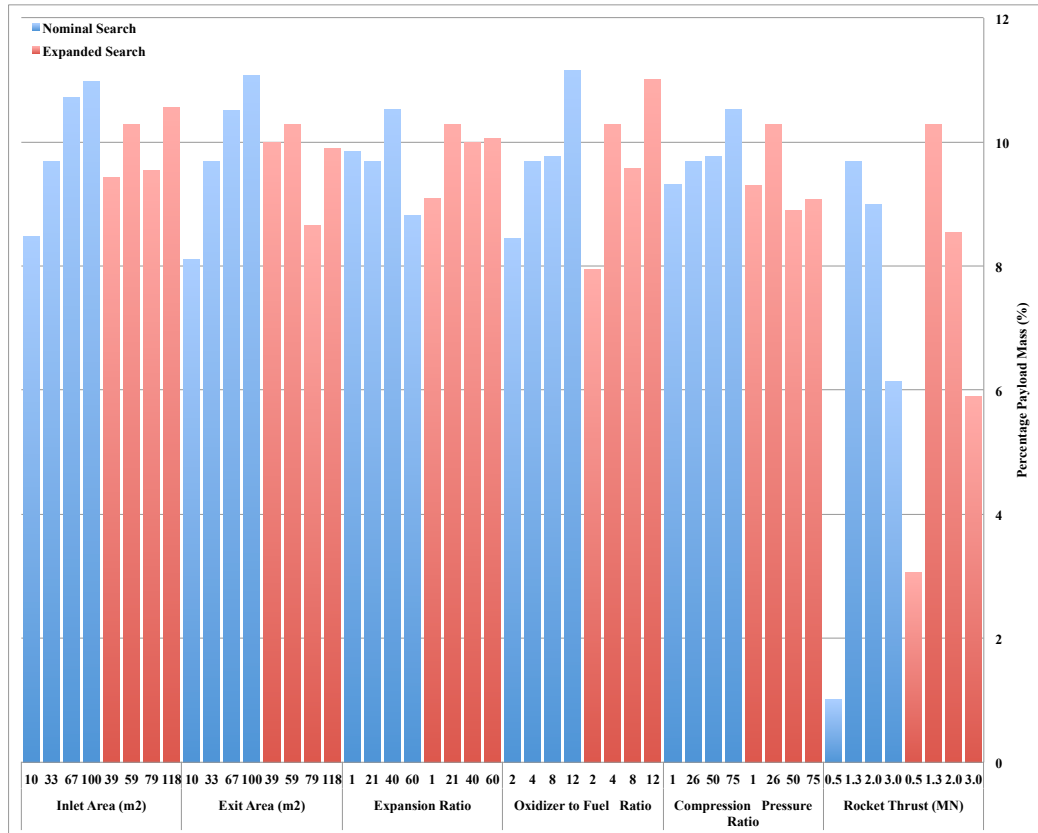
Figure 45: Payload fraction results from the sensitivity study for Rocket-Impulsive configurations with slender-body entry vehicles, grouped by variation in the design parameters. Blue curves represent solutions for the nominal search and red curves represent solutions for the expanded search.

Improved payload fraction is obtained with increased inlet and exit areas, which increase the descent propellant and engine mass but allow for greater reductions in the impulsive propellant mass due to the improved thrust, enabling favorable touchdown velocities. Payload fraction increases for greater compression ratios due to similar reasons. Increasing the oxidizer-to-fuel ratio decreases available thrust but was also observed to improve the payload fraction. This is a result of the dramatic reductions in fuel consumption, coupled with moderate improvements in ABSRP engine mass.

The payload fraction is seen to be most sensitive to variation in the rocket engine thrust, with reductions in thrust improving payload fraction. The higher impulsive and descent propellant consumption for these configurations is counteracted by significant improvements in impulsive rocket engine mass, contributing to lower overall vehicle mass. This trend breaks down for thrust below a certain point, as is evidenced by the drop in payload fraction for the lowest thrust configurations. For these cases, the descent propellant increases dramatically and overtakes the reduction in rocket engine mass. The propellant consumption is reinforced by additional increase in AB-SRP engine mass, where the vehicle must target other SRP initiation conditions in order to allow sufficient timeline for deceleration. Due to the convergence issues of the blunt-body simulations, the apparent performance improvement with increased thrust stems from the limited number of available cases, reflecting instead the reduction in performance for the lowest thrust configuration seen with the slender-body results.

Overall, it can be seen that optimal Rocket-Impulsive configurations are characterized by:

1. Low impulsive rocket thrust

2. Large inlet area

3. Large exit area

4. Large compression ratio

5. Large oxidizer-to-fuel ratio

However, rocket thrust is the parameter that most significantly influences the performance results. With the exception of the oxidizer-to-fuel ratio perturbations, the optimal characteristics are indicative of high ABSRP thrust configurations with low rocket thrust. This demonstrates that Rocket-Impulsive architectures prefer deceleration under the ABSRP engine rather than the rocket. The optimal oxidizer-to-fuel ratio results, despite going against the trend of favorable increasing ABSRP thrust, compensate by allowing for significant fuel mass savings.

4.5.4 Architecture Mass Breakdown

The sensitivity study also provided insight into the component masses of the different architectures. This information was valuable in determining the mass trends for each configuration in order to understand the interactions between the different subcomponents.

4.5.4.1 ABSRP-Only Mass Characteristics

The mass breakdowns of ABSRP-Only configurations are shown in Figure 46, with blunt-body configurations in Figure 46(a) and slender-body configurations in Figure 46(b). Both graphs are sorted in terms of increasing engine mass. Note that in general, lower vehicle mass corresponds to higher payload fraction.

As seen in the figure, blunt-body configurations, on average, have a higher vehicle mass (defined as the entry vehicle mass minus the payload mass) than slender-body configurations. The blunt-body vehicles however, also exhibit a much greater variation in vehicle mass and, as a result, can achieve lower total vehicle masses for certain designs. This gives rise to the tradeoff of favorable peak performance with the blunt-body configuration or favorable robustness to vehicle design with the slender-body
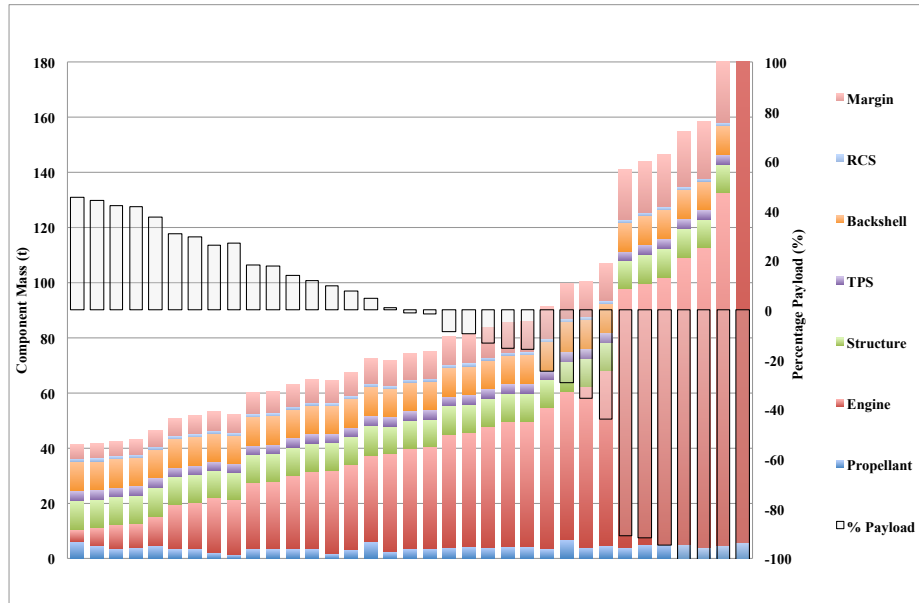
131

(a) Mass breakdown of the ABSRP-Only configurations utilizing blunt-body entry vehicles.
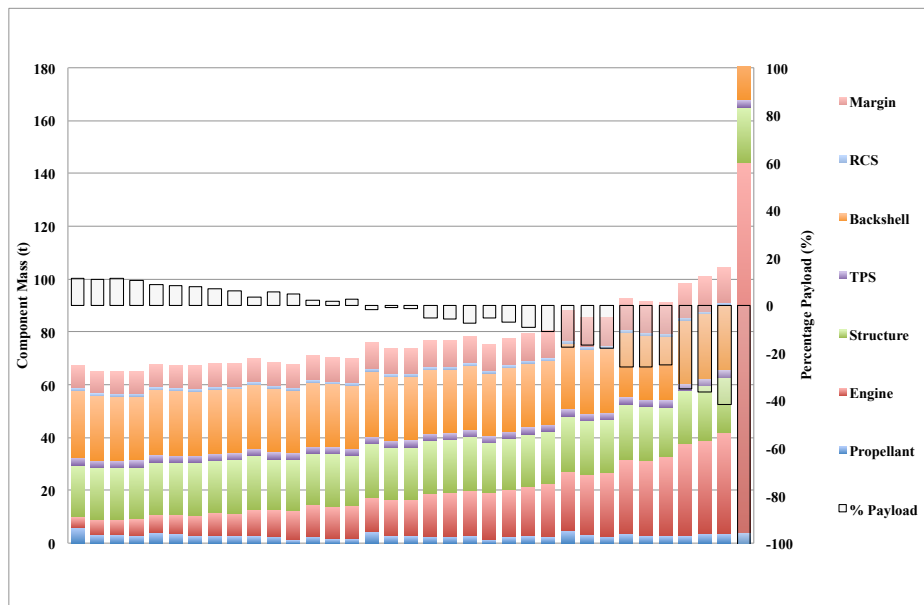
(b) Mass breakdown of the ABSRP-Only configurations utilizing slender-body entry vehicles.

Figure 46: Mass breakdown of the ABSRP-Only configurations simulated in the sensitivity study. Vehicle mass (entry mass minus payload mass) is plotted on the primary (left) axis and payload fraction is plotted on the secondary (right) axis in white for reference.

configuration.

The graphs also display the trend of ABSRP-Only vehicle mass being almost a one-to-one function of ABSRP engine mass. This is mostly due to the fact that the engine mass is the dominant mass component. For many blunt-body vehicles, the engine mass is multiple times larger than the sum of the remaining component masses and for slender-body vehicles, despite being less significant, the engine mass is still substantial and exhibits the largest variation. The remaining components, in order of greatest mass percentage, are the backshell mass, structure mass, propellant mass, TPS mass, and RCS mass. Of these parameters, only the propellant mass displays any significant variation. Nevertheless, the propellant mass has minimal effect on the overall mass results due to its small magnitude, instead contributing more to specific ordering of adjacent configurations.

Across all of the simulated designs, the engine mass of blunt-body vehicle is typically twice that of slender configurations due to the lower L/D blunt-body aeroshell being unable to sufficiently decelerate the vehicle and target favorable propulsive initiation conditions. The structure and backshell masses, conversely, are typically half, primarily due to the larger surface area of the slender aeroshell and associated mass penalty. The remaining propellant and TPS mass are found to be slightly higher, on average, for blunt body vehicles and the RCS mass displays negligible difference.

The payload fraction optimal vehicles, as determined from the sensitivity study, are seen to be the designs that best control the engine mass, with both the blunt-body and slender-body configurations (the left-most configurations in Figures 46(a) and 46(b)) being both payload fraction and engine mass optimal. The optimal blunt-body vehicle is able to reduce the average engine mass by over a factor of 13 whereas the optimal slender-body vehicle reduces the engine mass by 5 times. This results in final engine masses that are approximately equal. The greatest contribution to the increased slender vehicle mass are the structure and backshell mass, comprising 60%

133

of the vehicle mass for the slender-body configuration but only 30% for the blunt-body configuration. This corresponds to over a factor of two in terms of absolute mass. The optimal blunt-body configuration propellant, TPS, and RCS masses are slightly higher than those of the slender-body configuration, but contribute to much lower mass fractions than the structure.

4.5.4.2 Rocket-Impulsive Mass Characteristics

The mass breakdowns of Rocket-Impulsive configurations are shown in Figure 47, with blunt-body configurations in Figure 47(a) and slender-body configurations in Figure 47(b). Figure 47(a) is sorted in terms of increasing impulsive propellant mass while Figure 47(b) is sorted by increasing structure mass. The correlation between vehicle mass and payload fraction is much less pronounced for the Rocket-Impulsive architecture. This is partly due to the wide range of propellant mass values for the blunt-body configurations and the low overall variability of the slender-body configurations.

Just like with the ABSRP-Only architecture, Rocket-Impulsive blunt-body configurations, on average, have a higher vehicle mass than slender-body configurations. The disparity in overall mass variation is much greater for the Rocket-Impulsive architecture, with blunt-body vehicles exhibiting almost a full order of magnitude in variation and slender body vehicles having negligible change in vehicle mass for all but two designs. As a result, as was also seen with the ABSRP-Only architecture, the Rocket-Impulsive blunt-body architecture achieved lower minimum vehicle mass performance compared to slender configurations. Thus, a similar tradeoff is seen, with favorable peak performance for blunt-body vehicles and favorable robustness for slender-body vehicles.

Unlike the ABSRP-Only architecture, there is no single mass performance driver
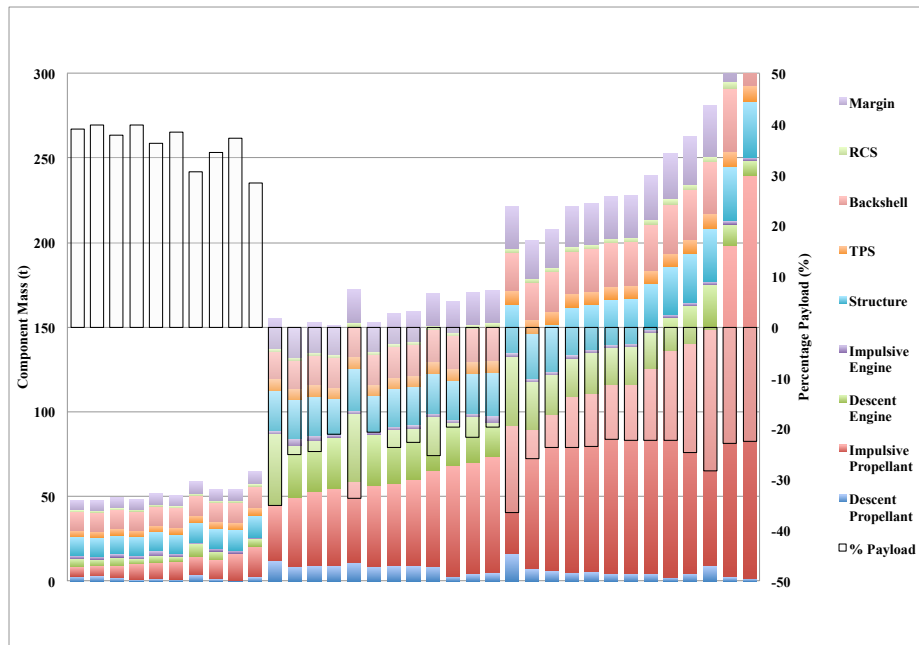
(a) Mass breakdown of the Rocket-Impulsive configurations utilizing blunt-body entry vehicles.
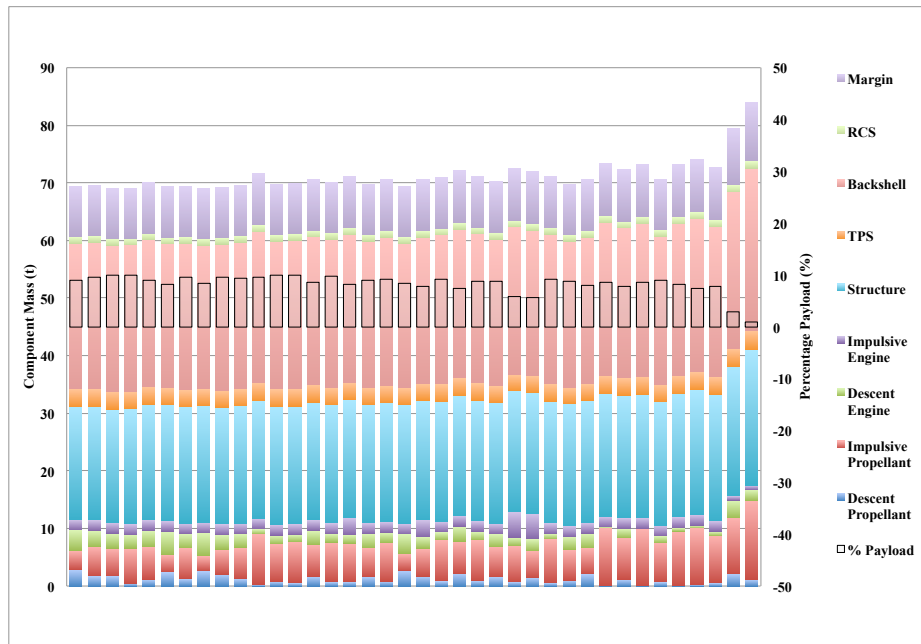
(b) Mass breakdown of the Rocket-Impulsive configurations utilizing slender-body entry vehicles.

Figure 47: Mass breakdown of the Rocket-Impulsive configurations simulated in the sensitivity study. Vehicle mass (entry mass minus payload mass) is plotted on the primary (left) axis and payload fraction is plotted on the secondary (right) axis in white for reference.

for all Rocket-Impulsive configurations. Vehicle mass is best correlated with the impulsive propellant for blunt-body vehicles because it exhibits the greatest variation. Conversely, vehicle mass is better correlated with the structure or backshell mass for slender-body architectures, due primarily to those components dominating the mass breakdown. Differences in the component masses of the two configurations are seen at all levels. The blunt-body vehicle mass is dominated by the impulsive propellant, followed by the structure, descent engine, and backshell mass. The propellant and engine masses are driven by the relatively poor aerodynamic performance of the blunt-body aeroshell, which is limited to targeting higher velocity propulsive initiation states. The remaining structure and backshell mass are a function of the large vehicle entry mass. The slender-body vehicle mass is dominated by the structure and backshell masses, with significant margin between them and the impulsive propellant mass. The structure and backshell mass fractions, in this case, are a direct result of the larger surface area of the slender aeroshell.

Averaged across all simulated configurations, with the exception of the backshell, the blunt-body designs have the same or worse component mass values. The largest difference is with the impulsive propellant, which is over 10 times more massive in blunt body vehicles. Due to its large contribution to the overall mass, this also corresponds to a large absolute mass discrepancy. The blunt-body descent engine mass is also 10 times that of the slender-body and the descent propellant mass is 5 times more massive. The majority of these results however, are a large function of the convergence challenges of the blunt-body configurations. The blunt-body structure and backshell mass are, on average, roughly equivalent. This demonstrates that the increase in predicted entry mass of the blunt-body vehicles counteracts the smaller wetted area, and correspondingly, lower structure and backshell mass fractions. The blunt and slender impulsive engine masses are identical due to the engine mass being a direct function of the prescribed thrust.

When comparing the payload fraction optimal blunt and slender-body vehicles, the optimal blunt configuration is observed to have larger or equal mass values for most subcomponents. The most notable are the significantly larger descent propellant and engine mass, due to the reduced aerodynamic performance of the blunt-body aeroshell and its inability to target favorable propulsive initiation conditions. All of these mass increases are negated however, by the blunt-body configuration requiring less than half of the structure and backshell mass of the slender-body vehicle. As a result, given that these components are the largest contributions to the mass of both optimal configurations, the optimal blunt-body vehicle is seen to have favorable performance over the optimal slender-body vehicle.

4.6   Rocket Descent Performance Characteristics

Rocket-Only configurations were simulated in order to serve as a reference for comparison against the ABSRP-Only and Rocket-Impulsive results. The Rocket-Only design space was sampled using the latin hypercube methodology, sampling both the descent and impulsive thrust values from the range of 500 kN to 2000 kN. All cases converged.

Optimal configurations were observed to be characterized by low impulsive thrust and moderate descent thrust. The total variation in payload fraction over all configurations considered was small, nominally around 5%, so even large changes in the design variables will only have modest effect. The mass breakdowns of Rocket-Only configurations are shown in Figure 48, with blunt-body configurations in Figure 48(a) and slender-body configurations in Figure 48(b). Note that the blunt body Rocket-Only configurations have favorable mass performance across practically all sets of design parameters and exhibit similar variation as the slender-body configurations.

The relative mass components are similar for both the blunt and slender body
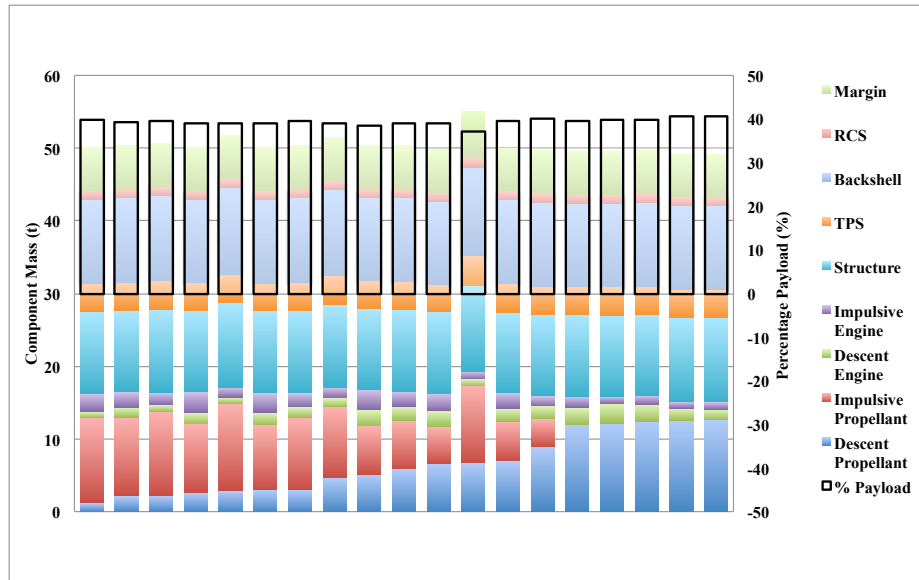
(a) Mass breakdown of the Rocket-Only configurations utilizing blunt-body entry vehicles.
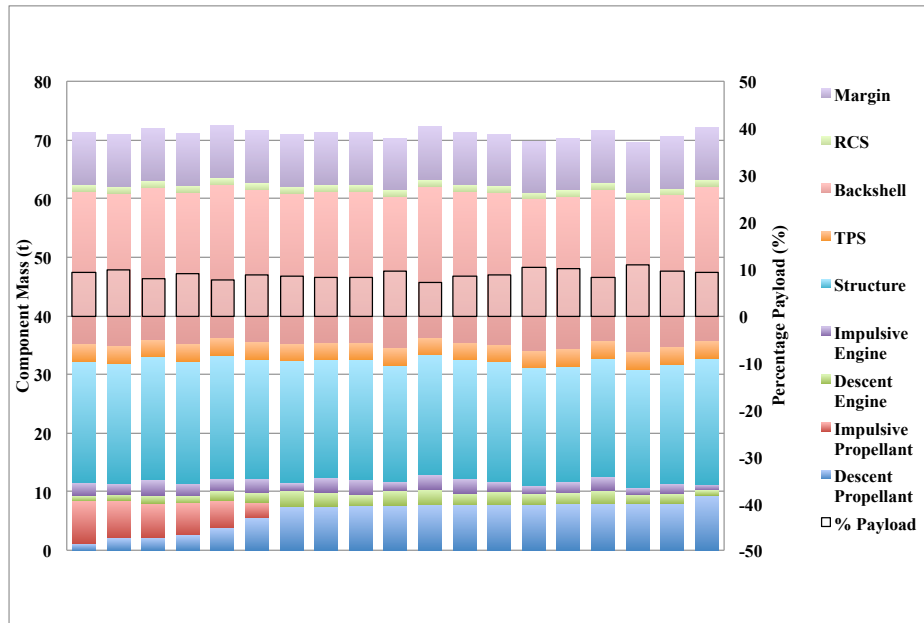
(b) Mass breakdown of the Rocket-Only configurations utilizing slender-body entry vehicles.

Figure 48: Mass breakdown of the Rocket-Only configurations. Vehicle mass (entry mass minus payload mass) is plotted on the primary (left) axis and payload fraction is plotted on the secondary (right) axis in white for reference.

vehicles, with the structure and backshell masses being the largest components (overwhelmingly so for the slender-body configurations). For the blunt-body configuration, the impulsive and descent propellant, the third and fourth biggest contributions, have similar mass fractions; whereas, for the slender-body vehicle, the descent propellant is significant but the impulsive propellant, and the rest of the mass components, do not majorly contribute. The only parameters which exhibit significant variation are the descent and impulsive propellant masses. Yet, it is observed in Figure 48 that the sum of the descent and impulsive propellant masses is approximately a constant value. This phenomena is a result of the identical efficiency values of the descent and impulsive engines and shows that the entire configuration must be capable of negating the total propulsive initiation velocity, regardless of the breakdown between impulsive and descent deceleration. A number of slender-body configurations are observed to have no impulsive propellant consumption, justifying the small averaged impulsive propellant mass fraction, and further demonstrating that the impulsive maneuver is not always necessary.

4.7 Architecture Comparison

The performance of each configuration can be compared based on their payload fraction values. A summary of the performance results and the favorable design parameters is shown in Table 10. In the table, $\%M_{PL}$ is the payload fraction, A_e/A^* is the nozzle expansion ratio, P_{rat} is the compression ratio, F_T is the rocket engine thrust, and Imp denotes properties of the impulsive maneuver. Of all configurations, the favorable design for both the blunt and slender-body vehicles was a configuration simulated in the original design space search.

The favorable ABSRP-Only configurations confirm the sensitivity study findings, that ABSRP-Only configurations prefer lower thrust, low propellant usage designs.

Table 10: Summary of performance and design parameters for favorable configurations of each architecture and entry vehicle type.

	$\% M_{PL}$	A_{in} (m^2)	A_{exit} (m^2)	A_e/A^*	OF	P_{rat}	P_{rat} Imp	F_T (kN)	F_T Imp (kN)
ABSRP-Only									
Blunt	47.9	44	22	36	12	36	4	-	-
Slender	16.3	59	8	23	12	41	9	-	-
Rocket-Impulsive									
Blunt	40.9	59	7	1	12	41	-	-	1880
Slender	10.2	59	7	1	12	41	-	-	1880
Rocket-Only									
Blunt	40.6	-	-	-	-	-	-	1000	656
Slender	10.8	-	-	-	-	-	-	1020	736
Minimum	-	1	1	1	2	1	1	500	500
Maximum	-	67	67	40	20	50	10	2000	2000

This is evidenced by the small exit area, large expansion ratio, and large oxidizer-to-fuel ratio. Counterexamples to the trend, in particular the large compression ratios, can be explained by investigating the convergence of adjacent designs. The favorable blunt-body configuration had one of the smallest impulsive compression ratios of all converged cases. The compression ratio was in the middle of the converged cases, but was necessary to allow for convergence with the largest oxidizer-to-fuel ratio and largest converging expansion ratio. Similar results were found for the favorable slender-body configuration, where the large compression ratios were necessary to allow for convergence with the favorable oxidizer-to-fuel ratio, expansion ratio, and exit area parameters.

The sensitivity study results indicated that favorable Rocket-Impulsive configurations prefer large ABSRP thrust over impulsive rocket thrust. Many of these characteristics are observed in the ideal vehicle configuration, which is seen to be identical for both the blunt and slender configurations. The favorable configuration prefers design variables at the extremes of their ranges, featuring a particularly small exit area and large oxidizer-to-fuel ratio, indicative of low ABSRP thrust, which are

compensated by an extremely low expansion ratio and large compression ratio, indicative of high thrust. The configuration is seen to have higher than average impulsive thrust, which is contrary to what was observed in the sensitivity study. Inspection of the payload fraction results with respect to thrust do not show a similar peak as was seen in the sensitivity study. As a result, the most likely explanation for the large thrust value is due to the Rocket-Impulsive performance being largely insensitive to the vehicle design variables, which allows for small variations in payload fraction to result in drastic variation of the design parameters.

4.7.1 Ideal Configuration Mass Comparison

Mass breakdowns of the most favorable configuration for each architecture are shown in Table 11, for blunt-body configurations, and Table 12, for slender-body configurations. The results show that, across all architectures, blunt body vehicles have considerably higher performance than slender vehicles. Analysis of individual configurations showed slender-body vehicles to outperform blunt-body configurations on average because they enable lower propulsive initiation velocities and correspondingly favorable engine and propellant mass benefits. Whereas blunt body configurations can control the engine and propellant mass components with vehicle design, slender-body vehicles are unable to reduce their large structure and backshell mass values and, as a result, suffer from lower optimal mass performance.

It is clear from the tables that the ABSRP-Only architecture displays the most favorable mass performance, having the lowest component masses in every category but engine mass. Comparing against the addition of the impulsive rocket engine for blunt body vehicles, the ABSRP-Only configuration is observed to enable small improvements to the structure, backshell, and TPS mass and significant reductions in engine mass and propellant usage. The structure, backshell and TPS mass fractions between the two architectures are nearly identical, which is to be expected given the

Table 11: Unmargined component mass values of the most favorable blunt-body configurations for each architecture.

	ABSRP-Only	Rocket-Impulsive	Rocket-Only
% Payload	47.9	40.9	40.6
Payload Mass	34.4	31.1	33.5
Entry Mass	71.6	76.1	82.6
Propellant Mass	1.6	6.1	12.6
Engine Mass	6.7	7.4	2.5
Structure Mass	9.7	10.5	11.6
Backshell Mass	10.0	10.7	11.6
TPS Mass	3.4	3.6	3.9
RCS Mass	1.1	1.1	1.2

Table 12: Unmargined component mass values of the most favorable slender-body configurations for each architecture.

	ABSRP-Only	Rocket-Impulsive	Rocket-Only
% Payload	16.3	10.2	10.8
Payload Mass	11.6	7.7	8.5
Entry Mass	71.4	74.8	78.0
Propellant Mass	1.4	4.8	8.0
Engine Mass	3.8	5.0	2.6
Structure Mass	19.6	20.1	20.2
Backshell Mass	23.7	24.8	25.9
TPS Mass	2.7	2.9	3.0
RCS Mass	1.1	1.1	1.2

use of the same hypersonic entry configuration. Therefore, the difference in mass arises from the reduction in total entry mass. The engine mass benefits stem from the fact that the Rocket-Impulsive configuration requires two separate engines.

The propellant mass savings are due to the different impulsive propulsion technologies. The impulsive maneuver was investigated for candidate ABSRP-Only and Rocket-Impulsive blunt-body configurations. The impulsive engine for the ABSRP-Only architecture achieved a thrust of 1090 kN and I_{SP} of 157s whereas the Rocket-Impulsive architecture reached 1880 kN thrust and 350s I_{SP}. The improved I_{SP} of the rocket engine allowed for 72% greater thrust with 22% reduction in propellant mass flow rate. For delta-v values in the region of interest, the ABSRP-Only engine impulsive maneuver was observed to require over twice the propellant of the Rocket-Impulsive engine. However, the atmospheric-breathing engine for this configuration was operating at an oxidizer-to-fuel ratio of 8 to 1. As a result, the fuel consumption for the ABSRP-Only impulsive maneuver was 75% less than that that of the Rocket-Impulsive engine. Similar results are seen for other atmospheric-breathing engine configurations.

Comparison of the slender-body configurations shows similar reduction in structure, backshell, and TPS mass due to the reduced entry mass of the ABSRP-Only architecture. The use of the slender-body entry vehicle allows for improved propulsive staging conditions and lower impulsive velocities, which benefits the engine and propellant component masses of both architectures. The increased contribution of the structure mass contributes to a reduced, but still substantial, performance gap between the ABSRP-Only and Rocket-Impulsive architectures.

The significant margin between the ABSRP-Only payload fraction and the payload fractions of the other architectures allows for substantial growth in the engine model before the ABSRP-Only architecture is no longer mass favorable. The ABSRP-Only blunt-body vehicle can accommodate an engine mass increase of up to 5.1 t,

which would correspond to a thrust-to-weight of 11.4. The slender-body vehicle can accommodate a 3.8 t growth in engine mass, allowing for thrust-to-weight values as low as 9.9. Therefore, even in the event that the atmospheric-breathing engine mass model underpredicts the weight by a factor of 2, the ABSRP-Only architecture is still mass favorable.

The benefits of using the atmospheric-breathing engine for descent are less significant. Comparison of the Rocket-Impulsive and Rocket-Only architectures shows that the addition of the atmospheric-breathing engine for descent has marginal, if any, benefit to payload fraction performance. For blunt-body configurations, the atmospheric-breathing engine reduces propellant consumption but increases engine mass, both expected due to the increased fuel efficiency but decreased T/W performance. The net result is the Rocket-Only architecture is heavier but also allows for more payload, contributing to similar payload fractions. The same trends are observed for the slender body vehicle.

4.7.2   Ideal Configuration Trajectories

Trajectories were investigated for the most favorable configurations of each architecture. This analysis allowed for greater insight into the characteristics of the different architectures and helped to provide a justification for the variation in architecture component masses and payload performance.

4.7.2.1   ABSRP-Only Trajectory

The trajectory characteristics of the favorable ABSRP-Only blunt-body configuration are shown in Figure 49, with the EDL altitude versus Mach profile displayed in Figure 49(a) and the forcing during the trajectory shown in Figure 49(b). Both figures are read from right to left because the vehicle decelerates throughout the trajectory. The hypersonic deceleration, ingestion, and propulsive initiation phases are indicated with the different colors and their intersections are marked with black circles for emphasis.

(a) Graph of the vehicle altitude profile versus Mach number, indicating the hypersonic, ingestion, and propulsive descent phases

(b) Graph of the drag and propulsive thrust profiles versus Mach number, indicating the hypersonic, ingestion, and propulsive descent phases
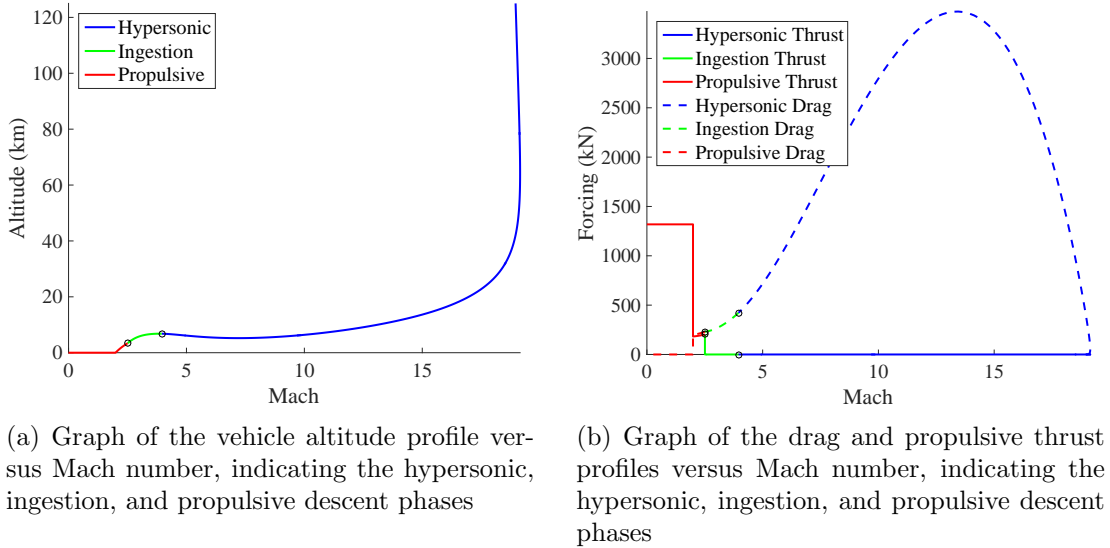
Figure 49: Trajectory characteristics of the favorable ABSRP-Only blunt-body configuration

The hypersonic deceleration phase in Figure 49(a) is typical of a blunt-body entry vehicle, which loses altitude quickly before descending into the higher density regions of the atmosphere and decelerating at relatively constant altitude. Bank angle control during this maneuver is observed to initially bank down in order to descend quicker and then bank up, to maintain altitude margin for propulsive initiation. Minimal control authority is maintained toward the end of the hypersonic maneuver so ingestion is initiated following the constant altitude deceleration at 6800 m.

The vehicle initiates the impulsive maneuver at Mach 2.0. This necessitates an extended ingestion phase, from Mach 4.0 through to Mach 2.5 (duration of 51 s), and leaves 23 s for descent under ABSRP. As evidenced in Figure 49(b), ABSRP descent thrust is on the order of the atmospheric drag. It is clear that the descent thrust is limited by the total available timeline following ingestion rather than a limited ingestion mass flow. The impulsive thrust is observed to be substantial, a function of the added compression and the fact that the impulsive propellant was assumed to be tanked starting at Mach 4.

The ideal slender-body ABSRP-Only trajectory is shown in Figure 50(a). The

overall trajectory shape in Figure 50 is similar to that of the blunt-body configuration, but the bank profile of the slender vehicle is much more chaotic, influenced by the significant control authority across the entire trajectory. This allows for the hypersonic configuration to initiate a loft maneuver prior to ingestion in order to set up favorable initiation conditions (ingestion is initiated at a $+1.6°$ flight path angle). The loft is seen to allow for higher altitude initiation of the ingestion and propulsive descent.

(a) Graph of the vehicle altitude profile versus Mach number, indicating the hypersonic, ingestion, and propulsive descent phases

(b) Graph of the drag and propulsive thrust profiles versus Mach number, indicating the hypersonic, ingestion, and propulsive descent phases
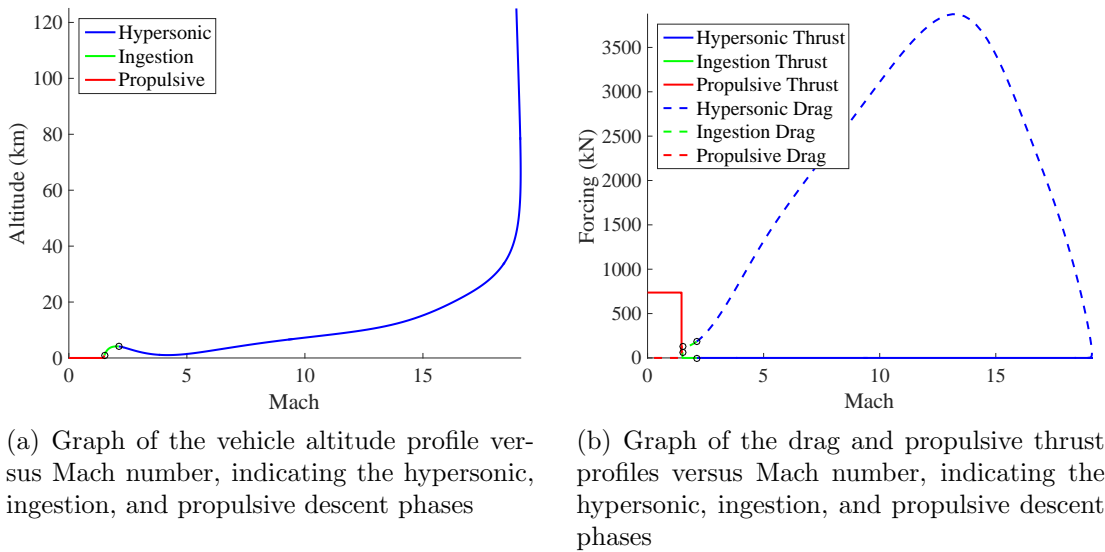
Figure 50: Trajectory characteristics of the favorable ABSRP-Only slender-body configuration

The vehicle transitions to the oxidizer ingestion phase at Mach 2.1 and an altitude of 4100 m. Ingestion continues for 50 s until propulsive initiation at Mach 1.5. Descent under SRP lasts only 7 s and the vehicle initiates the impulsive maneuver at Mach 1.46. It is evident that the slender body vehicle allows for lower transition velocities for all events. Descent thrust is still small, as shown Figure 50(b), but has a much shorter duration due to the favorable conditions established from the hypersonic trajectory. Impulsive thrust is smaller, but still on the order of the blunt-body results, likely a consequence of the lower pressure oxidizer storage.

As a result, both blunt and slender-body ABSRP-Only trajectories are characterized by large impulsive touchdown velocities and corresponding impulsive maneuvers. Collecting the oxidizer for these maneuvers necessitates long ingestion times that dominate the descent maneuver. The remainder of the trajectory is a short propulsive descent phase with limited thrust.

An attempt was made to limit the impulsive maneuvers to subsonic velocities, in an effort to constrain the large delta-v's and understand how those constraints affected the most favorable trajectory characteristics. Both the design space study and sensitivity study were rerun for the blunt and slender-body vehicles. None of the constrained vehicle designs were found to converge. These convergence challenges were likely due to modeling implementation issues, rather than shortcomings of the vehicle performance. This is due to the fact that the supersonic staging corridor for ABSRP-Only configurations shrinks as the constraint on the impulsive maneuver is tightened. Valid initiation conditions are bounded from below by the need to ingest sufficient oxidizer for the impulsive maneuver and are bounded from above by the need for sufficient deceleration in order to touchdown with subsonic velocity. Initiation states satisfying both conditions were found during the supersonic performance map generation, but were difficult to target with the GA optimizer due to the lack of global performance data used to guide the optimizer towards the optimum. In addition, for increased constraining of the impulsive maneuver, the initiation corridor becomes exceedingly narrow. This requires higher resolution mapping in order to adequately capture and sample within the corridor. Subsonic impulsive configurations were found during the sensitivity study for slender-body vehicles without constraints on the impulsive maneuver, but these were for suboptimal design configurations which had poor payload performance. Yet, it is expected that modification of trajectories of favorable design configurations will be able to achieve subsonic impulsive delta-v's with improved payload fraction results.

4.7.2.2   Rocket-Impulsive Trajectory

The trajectory characteristics of the favorable Rocket-Impulsive blunt-body configuration are shown in Figure 51, with the EDL altitude versus Mach profile displayed in Figure 51(a) and the forces during the trajectory shown in Figure 51(b). The Rocket-Impulsive altitude profile is very similar to the ABSRP-Only trajectory by nature of the similar hypersonic aeroshells. The lack of ingestion phase allows the Rocket-Impulsive architecture to sustain powered deceleration longer, initiating retro-propulsion at Mach 3.9 and 6000 m altitude and descending for 78 s before initiating the impulsive maneuver at Mach 0.8. The vehicle transitions to propulsive descent at a slightly positive flight path angle just prior to the loft peak.
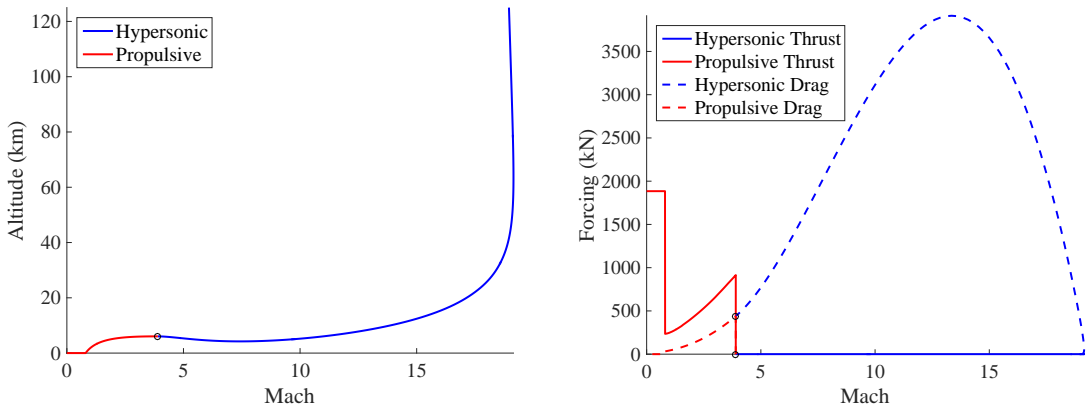
(a) Graph of the vehicle altitude profile versus Mach number, indicating the hypersonic and propulsive descent phases

(b) Graph of the drag and propulsive thrust profiles versus Mach number, indicating the hypersonic and propulsive descent phases

Figure 51: Trajectory characteristics of the favorable Rocket-Impulsive blunt-body configuration

ABSRP descent thrust is observed to be significant for this architecture, up to four times larger than in the ABSRP-Only architecture. The thrust is seen to decay as the vehicle decelerates. This decay is driven by the reduction in available oxidizer flow through the engine. Despite the decay, it is evident that the ABSRP engine is still capable of producing significant thrust upon touchdown. Thrust for the ideal impulsive rocket engine is larger than that of the impulsive ABSRP engine of the

148

ABSRP-Only architecture. The impulsive maneuver is seen to be much smaller than in the ABSRP-Only trajectory, but is still significant.

The slender-body trajectory, shown in Figure 52(a), is likewise similar to the slender-body ABSRP-Only trajectory. The hypersonic configuration sets up a significant loft, transitioning to propulsive descent at the peak in order to increase the timeline for the maneuver. Transition to propulsive descent occurs about the same point as ingestion initiation for the ABSRP-Only configuration, at just under Mach 2.1 at an altitude of 5100 m. Touchdown occurs subsonically, at Mach 0.7, following 68 s on descent propulsion.

(a) Graph of the vehicle altitude profile versus Mach number, indicating the hypersonic and propulsive descent phases

(b) Graph of the drag and propulsive thrust profiles versus Mach number, indicating the hypersonic and propulsive descent phases
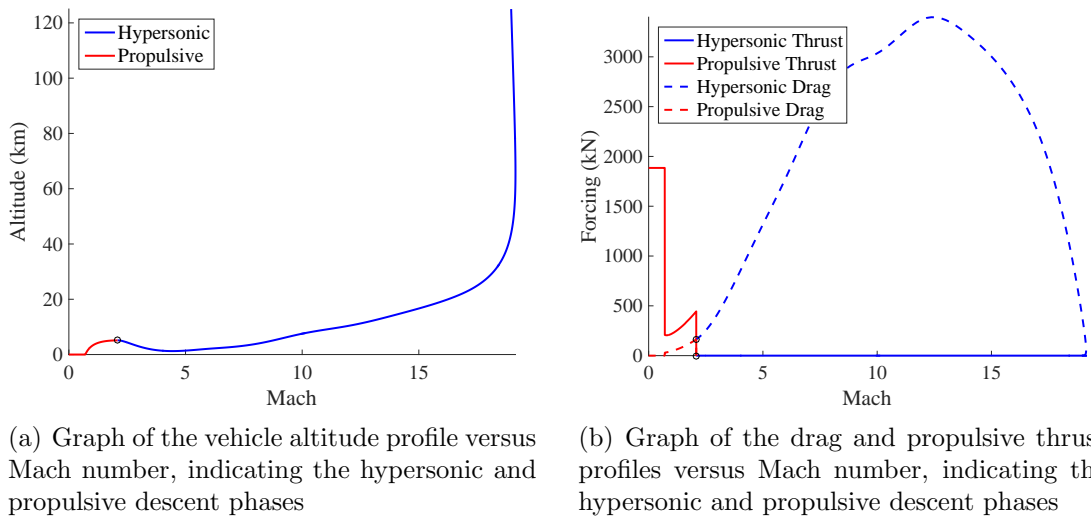
Figure 52: Trajectory characteristics of the favorable Rocket-Impulsive slender-body configuration

Descent thrust is again seen to be significant, as evidenced in Figure 52(b), and decreases over time due to the diminishing freestream conditions. For this configuration, a clear limit in ABSRP performance is observed. This is indicated in Figure 52(a) by the rapid altitude loss towards the end of the descent phase and in Figure 52(b) by the asymptotically decaying ABSRP thrust. As was seen in the initial low-fidelity trajectory simulation, with no transition to the impulsive maneuver, the vehicle would continue descending at approximately constant velocity, while continuing to consume

propellant. As a result, the Rocket-Impulsive configuration is observed to immediately initiate the impulsive maneuver in order to save fuel. Impulsive rocket thrust is much larger than that of the impulsive ABSRP engine in the ABSRP-Only configuration. The slender-body aeroshell is also observed to better control the hypersonic trajectory, maneuvering to reduce the peak dynamic pressure on the vehicle compared to the blunt-body configuration in an effort to mitigate the structural mass increase.

Overall, Rocket-Impulsive trajectories are characterized by longer powered descent phases. This is a direct result of the architecture removing the ingestion phase and allowing for more descent timeline. The net result is a smaller impulsive maneuver, capable of being initiated subsonically. Favorable architectures display significant ABSRP descent thrust, which is sustained as long as possible in order to leverage the higher mass efficiency of the atmospheric-breathing engine. The impulsive rocket engines are likewise able to achieve higher thrust performance than the corresponding impulsive ABSRP engines.

4.7.2.3   Rocket-Only Trajectory

The trajectory of the blunt-body Rocket-Only configuration in Figure 53(a) is significantly different than both of the ABSRP architectures. The hypersonic configuration decelerates at approximately constant altitude and sets up a slight loft, which is to be expected. The propulsive phase, in contrast with ABSRP descent phases, decelerates with constant thrust and achieves the terminal state conditions without the use of an impulsive maneuver. The use of a single maneuver is enabled by the independence of the propulsion system with respect to the flight environment. The preference of descent thrust over impulsive thrust is logical, given that the descent trajectory is aided by aerodynamic drag and the impulsive maneuver is modeled assuming no drag. These results are also similar to those observed in other studies, which found that optimal rocket SRP trajectories initiated propulsive descent as late as possible and

decelerated at full thrust until they achieve the terminal conditions [16]. Descent thrust values are approximately twice that of the ABSRP engine used in the Rocket-Impulsive architecture and around half of it's impulsive rocket engine thrust. The net result is propulsive initiation at Mach 2.8, later than in the Rocket-Impulsive architecture, with descent lasting 49 s.

(a) Graph of the vehicle altitude profile versus Mach number, indicating the hypersonic and propulsive descent phases

(b) Graph of the drag and propulsive thrust profiles versus Mach number, indicating the hypersonic and propulsive descent phases
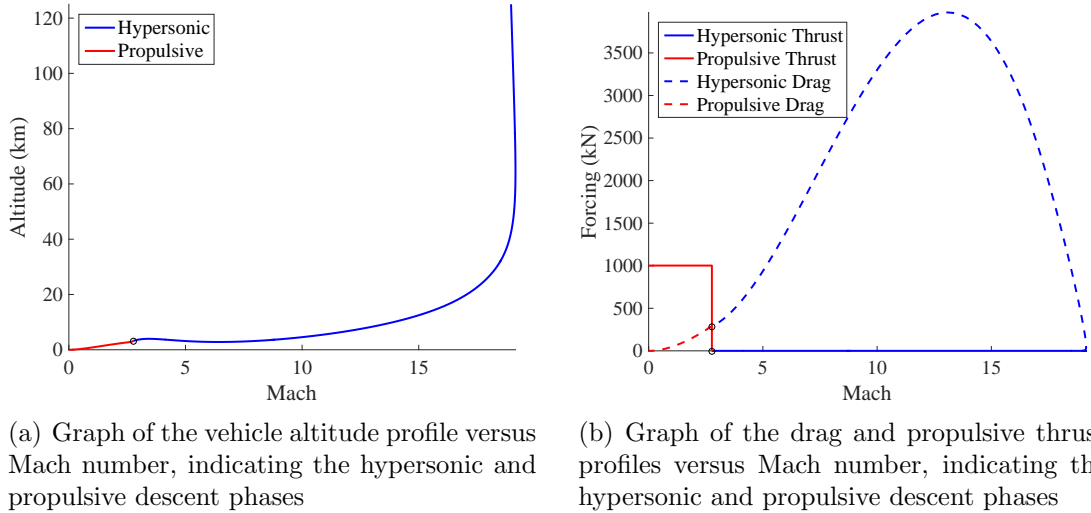
Figure 53: Trajectory characteristics of the favorable Rocket-Only blunt-body configuration

The slender-body Rocket-Only trajectory also targets the termination conditions without use of the impulsive maneuver. The mid-L/D aeroshell sets up a significant loft starting at Mach 4 and retropropulsion is initiated on the aft-side of the peak, at Mach 1.6, once the vehicle has expended all possible aerodynamic deceleration. Initiation occurs at a -15° flight path angle, which contributes to the reduced deceleration time of 34 s. Descent thrust is nearly identical to that of the blunt-body configuration, which is enabled by the favorable staging conditions allowed by the slender-body aeroshell. Like the Rocket-Impulsive configuration, significant modulation of the hypersonic trajectory is used to limit the peak dynamic pressure and resulting structural mass.

(a) Graph of the vehicle altitude profile versus Mach number, indicating the hypersonic and propulsive descent phases

(b) Graph of the drag and propulsive thrust profiles versus Mach number, indicating the hypersonic and propulsive descent phases
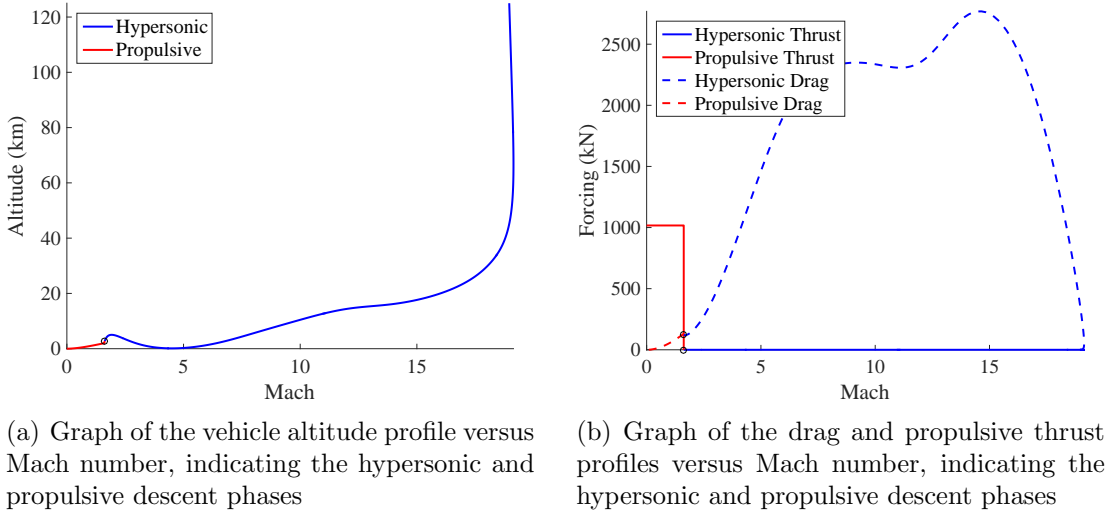
Figure 54: Trajectory characteristics of the favorable Rocket-Only slender-body configuration

4.8   Additional Constraints

Actual engine design will involve satisfying a number of constraints that are not explicitly enforced in the present investigation. One such constraint is the energy required to power the propulsion system compressor. Due to the complications of slag buildup, using a turbine to extract energy from the exhaust flow is likely unfeasible. There are a number of potential alternate energy sources in the system, given the large temperature differentials and energy of the surrounding flow. One option is to use the excess oxidizer (not required for combustion) to power a turbocharger.

The power required to compress the oxidizer can be calculated via Eq. 81, which assumes an isentropic process. If heat extraction is available, allowing for isothermal compression, then the power requirements can be reduced according to Eq. 82. In the equations, P is the power, $\dot{m}$ is the oxidizer mass flow rate, MM is the molar mass, γ is the ratio of the oxidizer specific heats, R is the universal gas constant, T is the temperature, and R_P is the compression ratio. The subscript req denotes power required, while S denotes an isentropic processes and T denotes an isothermal process.

$$P_{req,S} = \dot{m} \frac{\gamma RT}{MM(\gamma - 1)} \left(R_P^{((\gamma - 1)/\gamma)} - 1 \right) \tag{81}$$

$$P_{req,T} = \dot{m} \frac{RT}{MM} \log R_P \tag{82}$$

The power available, based on the excess ingested oxidizer, is on the order of the flow's kinetic energy, shown in Eq. 83. In the equation v_{ing} is the ingested velocity of the oxidizer, which approximates the oxidizer state prior to entering the turbocharger.

$$P_{avail} = \dot{m} v_{ing}^2 \tag{83}$$

The power available and required were evaluated for the optimal ABSRP-Only blunt and slender-body configurations, shown in Figure 55. For the slender-body configuration in Figure 55(b), the power available is on the same order as the power required. The power requirements for the blunt-body configuration in Figure 55(a) are increased, a function of the larger allowed mass flow rate through the engine. The ratio of the power available to the power required is reduced for this configuration, but is still on the same order.

(a) Power requirements for the blunt-body vehicle

(b) Power requirements for the slender-body vehicle
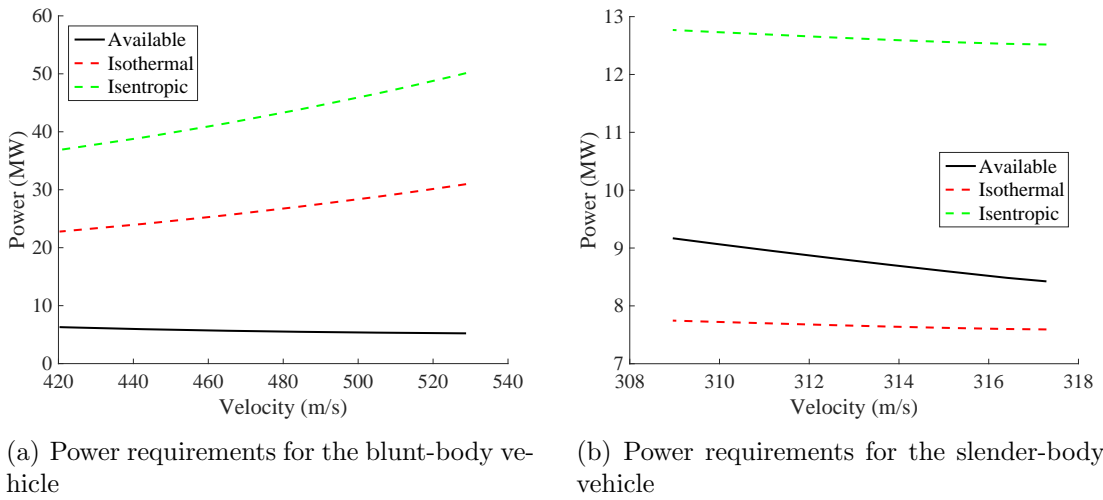
Figure 55: Power available (solid line) and required (dashed lines) to compress the oxidizer for the optimal ABSRP-Only configurations

Overall, it is observed that oxidizer compression power requirements are significant and could potentially influence design constraints. Nevertheless, power generation from the excess ingested oxidizer has the potential to satisfy a significant portion of the power requirements.

4.9 Summary

The design space and sensitivity studies provide critical insight into the performance and applications of architectures involving ABSRP. Vehicles employing solely atmospheric-breathing propulsion elements are seen to be most limited by the inlet area parameter and their associated ability to ingest oxidizer. This is primarily driven by the fact that these vehicles require significant oxidizer ingestion and storage in order to conduct the impulsive maneuver. The use of a rocket engine for terminal descent eliminates the need for the ingestion phase and, as a result, many more configurations are observed to converge. For these vehicle, the impulsive rocket thrust is observed to dictate convergence as the impulsive maneuver compensates for any lack of atmospheric-breathing deceleration during descent. The comparison between blunt body and slender-body Rocket-Impulsive configurations expands upon this observation, that convergence is ultimately based on total reduction in velocity, this being achieved either through greater impulsive delta-v, greater deceleration during descent, or lower velocity propulsive initiation conditions, with the performance impact of each configuration being determined by the associated component and propellant mass costs.

Optimal ABSRP configurations were seen to prefer low thrust, low propellant usage configurations. These vehicles were best able to mitigate the increased mass penalty due to the low thrust-to-weight of the atmospheric-breathing engine. As a result, favorable ABSRP-Only configurations were observed to be on the bound of non-convergence, desiring the minimal capabilities necessary to land the vehicle.

Architectures involving a rocket engine for impulsive deceleration were observed to prefer descent under the atmospheric-breathing engine over impulsive thrust from the rocket engine. While providing less thrust performance and being more massive, the atmospheric-breathing engine provided significant propellant mass savings. These configurations were ultimately observed to be relatively insensitive to changes in the input variables, with less than 5% variability in results across the entire space considered; whereas, atmospheric-breathing only configurations experienced multiple orders of magnitude variation. Architectures involving only rocket engines were likewise seen to be insensitive to variations in input parameters. Favorable Rocket-Only configurations were those that had minimum necessary descent thrust with small impulsive thrust. These configurations were best able to leverage aerodynamic deceleration while still ensuring that the vehicle landed safely.

Blunt-body configurations were observed to have poorer mass performance when averaged over all simulated vehicles, being a direct result of the wide variability among the configurations compared to slender-body vehicles. The blunt-body configurations were observed however, to achieve superior mass performance for certain configurations by mitigating their largest mass terms. The slender-body vehicles, conversely, were penalized by large structural components that dominated mass performance. Rocket-Only architectures were the one exception, with blunt-body configurations experiencing favorable mass performance across all architectures with similar variability to slender-body vehicles. This further demonstrates that the rocket vehicle performance was much less sensitive to the propulsive staging velocities. Mass performance of the ABSRP-Only architectures was observed to be driven by the atmospheric-breathing engine mass; whereas, Rocket-Impulsive configurations were driven by the impulsive propellant mass.

Among all of the architectures considered, ABSRP-Only vehicles were the most

mass-favorable for both blunt and slender vehicles. The use of the atmospheric-breathing engine for both descent and impulsive maneuvers displayed mass reductions for all components over configurations utilizing impulsive rocket engines. The use of an atmospheric-breathing engine versus a rocket for the descent maneuver resulted in lower propellant consumption at the cost of larger engine mass. As a result, the use of atmospheric-breathing propulsion for Mars descent and landing shows promise and can be seen to dramatically reduce propellant consumption. The main challenge with this architecture involves trying to reduce the large touchdown velocity inherent from including both ingestion and propulsion phases during descent without significant decrease in mass performance.

CHAPTER V

SUMMARY

5.1   Summary

In this investigation, atmospheric-breathing supersonic retropropulsion is shown to be a promising descent solution for human-class Mars EDL. Favorable configurations were found with total oxidizer capture and product expansion areas equaling 85% of the vehicle base area, demonstrating that, despite the low atmospheric density on Mars, ABSRP vehicles are able to capture and process sufficient oxidizer with inlets and exit areas of lower order than the vehicle scale. While significant effort remains to mature the technology, preliminary conceptual analysis shows the potential for overall mass reduction and does not reveal any insurmountable problems that preclude ABSRP from further consideration on future high-mass Mars missions.

This thesis quantifies the overall feasibility and performance of the ABSRP technology through the development of modeling methods and tools, the evaluation of conceptual ABSRP performance and sensitivities, and the formulation of vehicle concepts. Model development targeted components and subsystems most relevant to ABSRP in order to capture the necessary physics and provide a preliminary integrated vehicle simulation for future conceptual design efforts.

Models were developed to understand magnesium - carbon dioxide combustion performance and sensitivity to the wide range of flight environments relevant to Mars EDL. An equilibrium combustion simulation was developed with improved convergence for mixtures involving condensed phase species by decomposing convergence routines into robust subfunctions. Results showed Mg - CO_2 combustion to have favorable I_{SP} performance relative to rocket propulsion systems when accounting for

the fact that the atmospheric-breathing system does not carry its own oxidizer supply. The combustion performance was observed to be strongly influenced by the pressure of combustion and the ratio of the combustion and exhaust pressures.

A finite-rate kinetics simulation was also developed to assess the Mg-CO_2 kinetic timescales of the burning mixture. Auto-ignition was not predicted for any of the expected flight environments which indicated that an ignitor would likely be necessary to initiate combustion. Once the flame was established, combustion was observed to progress rapidly. An additional simulation was implemented in order to assess the diffusive timescales by simulating the evolution of a burning droplet. Burning times were shown to be sensitive to ambient pressure and the ratio of diffusive to kinetic timescale of the surface reaction. Combustion residence times were estimated to be on the order of 3 ms and burning times were on the order of 2-27 ms, demonstrating that complete combustion is indeed possible for reasonably sized combustion chambers.

Overall, Mg-CO_2 combustion was observed to have promising I_{SP} performance for moderate pressure ratios with significant potential improvement in fuel consumption. Evaluation of the burning timescales from kinetic and diffusion-limited models showed that combustion timescale requirements do not pose significant constraints on the design and that equilibrium performance results are valid as a first order prediction.

ABSRP vehicle and component models were also developed to allow for the evaluation of architecture performance in conceptual design. A first-order assessment was first performed, which decoupled the propulsion performance calculations and anchored all trajectories to a single initiation state. Without earlier collection and storage of oxidizer, atmospheric-breathing trajectories were observed to reach a terminal velocity state due to the velocity dependence of the engine, where the retro-propulsive thrust and aerodynamic drag jointly equaled the force of gravity acting on the vehicle. As a result, without the use of a separate maneuver, ABSRP vehicles are unable to reach the terminal state of zero velocity at zero altitude.

A full vehicle model extended beyond this first-order assessment by integrating the effects of varying propulsive performance and removing the assumption of constant propulsive initiation conditions. This necessitated the development of an additional hypersonic simulation, which was coupled with the existing supersonic propulsive simulation through the vehicle propellant mass and set of feasible propulsive staging conditions. A multi-step method was devised to converge this coupled system, which first simulated supersonic propulsive descent across a large map of initiation conditions. The supersonic performance map was used as the objective function for hypersonic trajectory optimization to determine the optimum staging conditions.

The full vehicle model also included subsystem models to account for specifics of the atmospheric-breathing trajectory. Unique force accounting equations were derived due to the exit and inlet areas both being located on the forebody for atmospheric-breathing retropropulsion vehicles. Realistic propulsion performance was implemented to determine the effects of the underexpanded engine, which involved remapping of the combustion performance data in order to calculate the expansion pressure based on the flight environment and engine parameters. The effects of gravity were added to the derivation of the impulsive maneuver in order to penalize low thrust-to-weight designs. Finally, subcomponent mass models were included to allow for sizing based on the specific vehicle and trajectory characteristics.

Multiple vehicle concepts were formulated utilizing various degrees of atmospheric-breathing propulsion. The first utilized atmospheric-breathing propulsion for both the descent and impulsive maneuvers. In order to provide a supplemental oxidizer supply to the engine for the impulsive maneuver, an additional ingestion phase was added prior to propulsive initiation. The second architecture utilized atmospheric-breathing propulsion during descent and transitioned to rocket propulsion for the impulsive maneuver. This allowed for the elimination of the oxidizer ingestion phase

and the corresponding complexity. The final simulation served as a reference vehicle for comparison, assuming traditional rocket propulsion for both the descent and impulsive maneuvers.

Investigations were conducted to evaluate the overall feasibility and performance of ABSRP as an EDL technology solution for human-class Mars missions. Candidate configurations were sized to land a 40 t, human-class payload using either a blunt or slender-body aeroshell. Variations were allowed in the relevant ABSRP and rocket propulsion design variables in order to understand their effects on the vehicle performance. Exploration of the full design space revealed insight into vehicle closure. Convergence of ABSRP-Only configurations was primarily dependent on the inlet area due to the constraint of ingesting sufficient oxidizer for the impulsive maneuver during descent. The Rocket-Impulsive configuration was seen to be more robust due to independence of the descent and impulsive maneuvers and the subsequent removal of the oxidizer ingestion phase. Convergence for these vehicles was most influenced by the impulsive thrust.

Parameter sensitivities were determined by perturbing designs away from a nominal vehicle, which was designed with relaxed constraints on the oxidizer capture in order to isolate the sensitivity of the results to the parameter in question. Optimal ABSRP-Only vehicles were characterized by low thrust trajectories that were on the boundary of not closing. Optimal Rocket-Impulsive trajectories indicated a preference of deceleration during atmospheric-breathing descent over impulsive rocket thrust. The Rocket-Impulsive architecture was not observed to be as sensitive to design changes.

The dominant mass component for the ABSRP-Only architecture was shown to be the atmospheric-breathing engine mass. Optimal ABSRP-Only configurations were those that were best able to mitigate this large component mass. The Rocket-Impulsive architecture, conversely, was characterized by large impulsive propellant

masses, with favorable configurations best minimizing the impulsive propellant usage. Slender-body vehicles tended to compare favorably in all propulsive component mass categories relative to equivalent blunt-body vehicles, but were penalized by significantly larger structure and backshell masses, due to the increased wetted area, which resulted in poor overall mass performance. As a result, favorable blunt-body configurations outperformed favorable slender-body configurations for all architectures considered.

The ABSRP-Only architecture exhibited the best mass performance among all architectures considered for both the blunt-body and slender-body vehicles, with significant margin to accommodate mass growth of the atmospheric-breathing engine. Rocket-Impulsive vehicles did not similarly outperform the Rocket-Only architecture, with payload fractions for the favorable vehicle of each architecture being comparable. While the ABSRP-Only architecture was mass-optimal, it was the only vehicle which was not observed to initiate the terminal impulsive maneuver subsonically.

The numerical models developed in this thesis provide the foundation for future conceptual design studies. The performance results provide a preliminary assessment of the vehicle capabilities and, in combination with the sensitivity assessment, allow for a prediction of the ABSRP performance across the design space. Vehicle concepts describe practical implementations of the ABSRP technology and enable assessment of both the benefits and drawbacks of the ABSRP integration into the overall EDL architecture.

5.2   Suggestions for Future Work

The propulsion system characterization provided a preliminary estimate of the engine performance and variation due to design changes and flight environment. As was observed with the particle burning results however, significant deviation still exists between computational and experimental results. The combustion of magnesium

and carbon dioxide requires accurate simulation of the kinetic, diffusive, and flow equations for a multi-phase mixture that exhibits both evaporation and condensation effects. Time varying simulation of a realistic combustor may have to also predict accumulation of the condensed-phase products on the combustion chamber or nozzle, as well as predict the effects of imperfect particle injection and settling.

The combination of these factors motivates the need for ample experimental exploration and performance qualification. Limited validation and qualification data exists today of any sort. The information that is present is primarily focused on the combustion phenomena of isolated particles. As a result, much more work is required investigating streams of suspended particles in order to understand the effects of flame propagation and stabilization, especially when influenced by the effects of settling, clumping, and recirculation. Most important, is a systematic experimental effort to study Mg-CO$_2$ combustion across the range of environments expected during Mars EDL in order to characterize the performance, associated timescales, and burning phenomena. Additional effort should be focused on understanding the impact of the condensed phase particles on the propulsive performance, including any performance reductions as a result of mitigation of slag buildup.

The full vehicle modeling presented an initial approach of how to account for the relevant effects of atmospheric-breathing propulsion during conceptual design. One noticeable shortcoming was the lack of adequate mass models for the atmospheric-breathing engine, which incorporate effects of the flow stagnation and redirection. Unfortunately, due to their use on primarily military and other restricted vehicles, available data for high-speed propulsion engine masses and specifications is considerably lacking. Use of a regression method, similar to what was performed with the other component mass estimates, will require a supporting dataset of many candidate engines, preferably at the scale of interest. The alternative, summing mass estimates of individual components is likely even more challenging, requiring a concrete layout

of the engine and understanding of the specific combustion environment. Any mass models used will need to account for the flow redirection, effects of varying oxidizer compression and, in the case of the ABSRP-Only architecture, ingestion and storage of the oxidizer. Improved mass models would also be useful for the structure and backshell masses of the slender-body entry vehicle. Estimates used in this study relied on penalizing blunt-body results based on the ratio of wetted or non-wetted areas. Additional study, including the assessment of realistic vehicle designs, would be useful for refining this estimate.

Finally, any vehicle sizing performed during conceptual design will require the definition of a specific baseline mission and payload. This will allow for the specification of more appropriate initiation and termination conditions for ABSRP based on the other decent technologies used in the architecture and their associated flight envelopes. While the present investigation identified ABSRP as possibly enabling significant mass savings, the ability for ABSRP to integrate with the entry vehicle and payload is a significant contribution to its overall technology performance. This includes a characterization of the volume of all elements of the design as well as their layout, ensuring that they can integrate around a payload without interfering with the function of either.

One particular issue that was not addressed is the location and design of inlets and exhaust on the forward side of the vehicle. Integration with the vehicle heat shield will therefore require an engineering solution that does not inhibit the performance of the heatshield or structural performance of the vehicle. The one advantage of the system is the separation between the primary heating events, which occur at the high mach numbers, and propulsive descent, which will occur in the supersonic regime. Therefore, the implementation of a vehicle reconfiguration or transition event is theoretically possible. Packaging of the remaining components, such as the propellant tanks, pumps, and combustion chamber will similarly require detailed design

and packaging within the vehicle. Specific treatment is required to ensure that these components do not geometrically interfere with the payload or surrounding vehicle and that the heat generated from the propulsion system does not adversely interfere with other components. All of these considerations, as is typical with EDL systems, will be highly vehicle and mission dependent.

APPENDIX A

LIST OF PUBLICATIONS

Thesis-relevant publications

- Gonyea, K. C., Braun, R. D., and Auslender, A. H., "Feasibility and Performance of Atmospheric-Breathing Propulsion for Mars Descent," submitted to *Journal of Spacecraft and Rockets*, May 2017

- Gonyea, K. C., Braun, R. D., and Auslender, A. H., "Propulsion System Design for a Martian Atmosphere Breathing Supersonic Retropropulsion Engine," *Journal of Propulsion and Power*, Vol. 32, No. 3, May 2016, pp. 574-582.

- Gonyea, K. C. and Braun, R. D., "Propulsion System Design for a Martian Atmosphere Breathing Supersonic Retropropulsion Engine," *50th AIAA Joint Propulsion Conference*, Cleveland, OH, July 2014.

Non-thesis-relevant publications

- Gonyea, K. C., Tanner, C. L., Clark, I. G., Kushner, L. K., Schairer, E. T., and Braun, R. D., "Aerodynamic Stability and Performance of Next-Generation Parachutes for Mars Entry, Descent, and Landing," *22nd AIAA Aerodynamic Decelerator Systems Technology Conference and Seminar*, Daytona Beach, FL, March 2013.

- Li, L., Gonyea, K. C., and Braun, R. D. "Finite Element Analysis of the Inflatable Re-Entry Vehicle Experiment," *2015 AIAA Science and Technology Forum*, Kissimmee, Florida, January 2015.

REFERENCES

[1] Braun, R. D. and Manning, R. M., "Mars Exploration Entry, Descent, and Landing Challenges," *Journal of Spacecraft and Rockets*, Vol. 44, No. 2, March 2007, pp. 310–323.

[2] Williams, D. R., "Mars Fact Sheet," April 2014.

[3] Williams, David R, "Earth Fact Sheet," July 2013.

[4] Soffen, G., "Mars and the Remarkable Viking Results," *Aerospace Sciences Meetings*, American Institute of Aeronautics and Astronautics, Jan. 1978, pp. –.

[5] nasa.gov, "Viking on Mars: 30 Year Later," Aug. 2015.

[6] Thurman, S., "Return to the Red Planet - An Overview of the Mars Pathfinder Mission," *Aerodynamic Decelerator Systems Technology Conferences*, American Institute of Aeronautics and Astronautics, May 1995, pp. –.

[7] Steltzner, A., Lee, W., Bruno, R., and Desai, P., "The Mars Exploration Rovers Entry Descent and Landing Phase and the Use of Aerodynamic Decelerators," *Aerodynamic Decelerator Systems Technology Conferences*, American Institute of Aeronautics and Astronautics, May 2003, pp. –.

[8] Steltzner, A. D., Miguel San Martin, A., Rivellini, T. P., Chen, A., and Kipp, D., "Mars Science Laboratory Entry, Descent, and Landing System Development Challenges," *Journal of Spacecraft and Rockets*, Vol. 51, No. 4, May 2014, pp. 994–1003.

[9] Fallon II, E., "System Design Overview of the Mars Pathfinder Parachute Decelerator Subsystem," *Aerodynamic Decelerator Systems Technology Conferences*, American Institute of Aeronautics and Astronautics, June 1997, pp. –.

[10] Cruz, J., Mineck, R., Keller, D., and Bobskill, M., "Wind Tunnel Testing of Various Disk-Gap-Band Parachutes," *Aerodynamic Decelerator Systems Technology Conferences*, American Institute of Aeronautics and Astronautics, May 2003, pp. –.

[11] Witkowski, A. and Bruno, R., "Mars Exploration Rover Parachute Decelerator System Program Overview," *Aerodynamic Decelerator Systems Technology Conferences*, American Institute of Aeronautics and Astronautics, May 2003, pp. –.

[12] Witkowski, A., Kandis, M., and Adams, D., "Mars Scout Phoenix Parachute System Performance," *Aerodynamic Decelerator Systems Technology Conferences*, American Institute of Aeronautics and Astronautics, May 2009, pp. –.

[13] Sengupta, A., Witkowski, A., Rowan, J., Taeger, Y., Kandis, M., Malachick, W., Moran, J., Baker, K., Smith, D., Morris, J., Thome, E., and Masterleo, M., "Overview of the Mars Science Laboratory Parachute Decelerator System," *Aerodynamic Decelerator Systems Technology Conferences*, American Institute of Aeronautics and Astronautics, May 2007, pp. –.

[14] Edquist, K. T., Korzun, A. M., Dyakonov, A. A., Studak, J. W., Kipp, D. M., and Dupzyk, I. C., "Development of Supersonic Retropropulsion for Future Mars Entry, Descent, and Landing Systems," *Journal of Spacecraft and Rockets*, Vol. 51, No. 3, April 2014, pp. 650–663.

[15] Dwyer-Cianciolo, A., Davis, J., Komar, D., Munk, M., Samareh, J., Williams-Byrd, J, Z. T., Powell, R., Shidner, J., Stanley, D., Wilhite, A., Kinney, D., McGuire, K., Arnold, J., Howard, A., Sostaric, R., Studak, J., Zumwalt, C., Llama, E., Casoliva, J., Ivanov, M., Clark, I., and Sengupta, A., "Entry, Descent and Landing Systems Analysis Study: Phase 1 Report," *NASA TM-2010-216720*, July 2010.

[16] Korzun, A. M., *Aerodynamic and Performance Characterization of Supersonic Retropropulsion for Application to Planetary Entry and Descent*, Ph.D. thesis, Georgia Institute of Technology, 2012.

[17] Edquist, K., "Supersonic Retropropulsion for Mars Entry," .

[18] Korzun, A., Christopher Cordell, J., and Braun, R., "Comparison of Inviscid and Viscous Aerodynamic Predictions of Supersonic Retropropulsion Flowfields," *Fluid Dynamics and Co-located Conferences*, American Institute of Aeronautics and Astronautics, June 2010, pp. –.

[19] Peters, C. and Phares, W., "The Structure of Plumes from Moderately Underexpanded Supersonic Nozzles," *Aerospace Sciences Meetings*, American Institute of Aeronautics and Astronautics, Jan. 1970, pp. –.

[20] Wilkes, J., Glass, C., Danehy, P., and Nowak, R., "Fluorescence Imaging of Underexpanded Jets and Comparison with CFD," *Aerospace Sciences Meetings*, American Institute of Aeronautics and Astronautics, Jan. 2006, pp. –.

[21] Abbett, M., "Mach Disk in Underexpanded Exhaust Plumes," *AIAA Journal*, Vol. 9, No. 3, March 1971, pp. 512–514.

[22] Jarvinen, P. O. and Adams, R. H., "The Aerodynamic Characteristics of Large Angled Cones with Retrorockets," Tech. Rep. CR NAS 7-576, Feb. 1970.

[23] Moeckel, W. E., "Flow Separation Ahead of Blunt Bodies at Supersonic Speeds," Tech. rep., July 1951.

[24] Love, E. S., Grigsby, C. E., Lee, L. P., and Woodling, M. J., "Experimental and Theoretical Studies of Axisymmetric Free Jets," Tech. rep., 1959.

[25] Moeckel, W. E., "Flow Separation Ahead of a Blunt Axially Symmetric Body at Mach Numbers 1.76 to 2.10," Tech. rep., Dec. 1951.

[26] Love, E. S., Woodling, M. J., and Lee, L. P., "Boundaries of Supersonic Axisymmetric Free Jets," Tech. rep., Oct. 1956.

[27] Love, E. S., "The Effects of a Small jet of Air Exhausting from the Nose of a Body of Revolution in Supersonic Flow," Tech. rep., Nov. 1952.

[28] Korzun, A. M., Braun, R. D., and Cruz, J. R., "Survey of Supersonic Retropropulsion Technology for Mars Entry, Descent, and Landing," *Journal of Spacecraft and Rockets*, Vol. 46, No. 5, Sept. 2009, pp. 929–937.

[29] Hefner, J. N. and Keyes, J. W., "Effect of Forward-Facing Jets on Aerodynamic Characteristics of Blunt Configurations at Mach 6," *Journal of Spacecraft and Rockets*, Vol. 4, No. 4, April 1967, pp. 533–534.

[30] Jarvinen, P. O. and Adams, R. H., "The Effects of Retrorockets on the Aerodynamic Characteristics of Conical Aeroshell Planetary Entry Vehicles," *Aerospace Sciences Meetings*, American Institute of Aeronautics and Astronautics, Jan. 1970, pp. –.

[31] Charczenko, N. and Hennessey, K. W., "Investigation of a Retrorocket Exhausting From the Nose of a Blunt Body Into a Supersonic Free Stream," Tech. rep., Sept. 1961.

[32] McGhee, R. J., "Effects of a Retronozzle Located at the Apex of a 140 Degree Blunt Cone at Mach Numbers of 3.00, 4.50, and 6.00," Tech. rep., Jan. 1971.

[33] Peterson, V. L., McKenzie, R. L., and States, U., *Effects of Simulated Retrorockets on the Aerodynamic Characteristics of a Body of Revolution at Mach Numbers from 0.25 to 1.90*, NASA technical note ;NASA TN D-1300, National Aeronautics and Space Administration : [For sale by the Office of Technical Services, Dept. of Commerce, Washington, D.C., 1962.

[34] Berry, S. A., Laws, C. T., Kleb, W. L., Rhode, M. N., Spells, C., Mccrea, A. C., Trumble, K. A., Schauerhamer, D. G., and Oberkampf, W. L., "Supersonic Retropropulsion Experimental Design for Computational Fluid Dynamics Model Validation," *2011 Aerospace Conference*, Institute of Electrical and Electronics Engineers (IEEE), Institute of Electrical & Electronics Engineers (IEEE), March 2011.

[35] Berry, S., Rhode, M., and Edquist, K., "Supersonic Retropropulsion Experimental Results from the NASA Ames 9- x 7-Foot Supersonic Wind Tunnel," *Fluid Dynamics and Co-located Conferences*, American Institute of Aeronautics and Astronautics, June 2012, pp. –.

[36] Berry, S. A. and Rhode, M. N., "Supersonic Retropropulsion Test 1853 in NASA LaRC Unitary Plan Wind Tunnel Test Section 2," Tech. rep., April 2014.

[37] Berry, S., Rhode, M., Edquist, K., and Player, C., "Supersonic Retropropulsion Experimental Results from the NASA Langley Unitary Plan Wind Tunnel," *Fluid Dynamics and Co-located Conferences*, American Institute of Aeronautics and Astronautics, June 2011, pp. –.

[38] Bakhtian, N. M. and Aftosmis, M. J., "Parametric Study of Peripheral Nozzle Configurations for Supersonic Retropropulsion," *Journal of Spacecraft and Rockets*, Vol. 47, No. 6, Nov. 2010, pp. 935–950.

[39] Bakhtian, N. and Aftosmis, M., "Analysis of Inviscid Simulations for the Study of Supersonic Retropropulsion," *Fluid Dynamics and Co-located Conferences*, American Institute of Aeronautics and Astronautics, June 2011, pp. –.

[40] Cordell, C. E., Clark, I. G., and Braun, R. D., "CFD Verification of Supersonic Retropropulsion for a Central and Peripheral Configuration," *IEEEAC paper 1190*, IEEE, 2011.

[41] Korzun, A. M., Cordell, C. E., and Braun, R. D., "Computational Aerodynamic Predictions of Supersonic Retropropulsion Flowfields," *Journal of Spacecraft and Rockets*, Vol. 50, No. 5, Aug. 2013, pp. 950–960.

[42] Korzun, A. M. and Braun, R. D., "Application of a Reynolds-Averaged Navier-Stokes Approach to Supersonic Retropropulsion Flowfields," *Journal of Spacecraft and Rockets*, Vol. 50, No. 5, July 2013, pp. 961–980.

[43] Schauerhamer, D., Trumble, K., Kleb, W., Carlson, J.-R., and Edquist, K., "Continuing Validation of Computational Fluid Dynamics for Supersonic Retropropulsion," *Aerospace Sciences Meetings*, American Institute of Aeronautics and Astronautics, Jan. 2012, pp. –.

[44] Trumble, K., "An Initial Assessment of Navier-Stokes Codes Applied to Supersonic Retro-Propulsion," *Fluid Dynamics and Co-located Conferences*, American Institute of Aeronautics and Astronautics, June 2010, pp. –.

[45] Zarchi, K. A., Schauerhamer, D. G., Kleb, W. L., Carlson, J.-R., and Edquist, K. T., "Analysis of Navier-Stokes Codes Applied to Supersonic Retropropulsion Wind-Tunnel Test," *Journal of Spacecraft and Rockets*, Vol. 51, No. 3, April 2014, pp. 680–692.

[46] Berry, S. A., Rhode, M. N., and Edquist, K., "Supersonic Retropropulsion Validation Experiment in the NASA Langley Unitary Plan Wind Tunnel," *Journal of Spacecraft and Rockets*, Vol. 51, No. 3, April 2014, pp. 664–679.

[47] Cordell, C. E. and Braun, R. D., "Analytical Modeling of Supersonic Retropropulsion Plume Structures," *Journal of Spacecraft and Rockets*, Vol. 50, No. 4, June 2013, pp. 763–770.

[48] Cordell, C. E., *Computational Fluid Dynamics and Analytical Modeling of Supersonic Retropropulsion Flowfield Structures Across a Wide Range of Potential Vehicle Configurations*, Ph.D. thesis, Georgia Institute of Technology, Atlanta, GA, 2013.

[49] Adler, M., Wright, M., Campbell, C., Clark, I., Engelund, W., and Rivellini, T., "Entry, Descent, and Landing Roadmap: Technology Area 09," Tech. rep., Nov. 2010.

[50] Toups, L., Brown, K., and Hoffman, S. J., "Transportation-Driven Mars Surface Operations Supporting an Evolvable Mars Campaign," *IEEE Aerospace Conference*, IEEE, Jan. 2015.

[51] Horvath, T. J., Aubuchon, V. V., Rufer, S. J., Campbell, C. H., Schwartz, R. J., Mercer, C. D., Tack, S., Spisz, T. S., Taylor, J. C., Gibson, D. M., Osei-Wusu, K., Kennerly, S., Scriven, G., Pottebaum, T., and Ross, M., "**Advancing Supersonic Retro-Propulsion Technology Readiness: Infrared Observations of the SpaceX Falcon 9 First Stage**," *AIAA Space Forum*, American Institute of Aeronautics and Astronautics, Sept. 2017.

[52] Spisz, T. S., Taylor, J. C., Gibson, D. M., Kennerly, S., Osei-Wusu, K., Scriven, G., Pottebaum, T., Horvath, T. J., Schwartz, R. J., Tack, S., and Bush, B. C., "**Processing Infrared Imagery of the SpaceX Falcon First Stage Reentry During CRS-4 Mission** ," *AIAA Space Forum*, American Institute of Aeronautics and Astronautics, Sept. 2017.

[53] Edquist, K. T., Korzun, A. M., Bibb, K. L., Schauerhamer, D. G., Ma, E. C., McCloud, P. L., Palmer, G. E., and Monk, J. D., "**Comparison of Navier-Stokes Flow Solvers to Falcon 9 Supersonic Retropropulsion Flight Data** ," *AIAA Space Forum*, American Institute of Aeronautics and Astronautics, Sept. 2017.

[54] Sforzo, B. and Braun, R. D., "Feasibility of Supersonic Retropropulsion Based on Assessment of Mars-Relevant Flight Data," *AIAA Space Forum*, American Institute of Aeronautics and Astronautics, Sept. 2017.

[55] "Human Exploration of Mars, Design Reference Architecture 5.0," *Mars Architecture Steering Group*, edited by B. Drake, NASA, July 2009.

[56] Price, H., Hawkins, A., and Radcliffe, T., "Austere Human Missions to Mars," *SPACE Conferences and Exposition*, American Institute of Aeronautics and Astronautics, Sept. 2009, pp. –.

[57] Steinfeldt, B., Theisinger, J., Korzun, A., Clark, I., Grant, M., and Braun, R., "High Mass Mars Entry, Descent, and Landing Architecture Assessment," *SPACE Conferences and Exposition*, American Institute of Aeronautics and Astronautics, Sept. 2009, pp. –.

[58] Cianciolo, A. D., Zang, T. A., Sostaric, R. R., and McGuire, M. K., "Overview of the NASA Entry, Descent and Landing Systems Analysis Exploration Feed-Forward Study," *Proceedings of the 8th International Planetary Probe Workshop*, June 2011.

[59] Cianciolo, A. M. D., Davis, J. L., Engelund, W. C., Komar, D. R., Queen, E. M., Samareh, J. A., Way, D. W., Zang, T. A., Murch, J. G., Krizan, S. A., Olds, A. D., Powell, R. W., Shidner, J. D., Kinney, D. J., McGuire, M. K., Arnold, J. O., Covington, M. A., Sostaric, R. R., Zumwalt, C. H., and Llama, E. G., "Entry, Descent and Landing Systems Analysis Study: Phase 2 Report on Exploration Feed-Forward Systems," Tech. rep., Feb. 2011.

[60] Grant, M. J., Steinfeldt, B. A., Braun, R. D., and Barton, G. H., "Smart Divert: A New Mars Robotic Entry, Descent, and Landing Architecture," *Journal of Spacecraft and Rockets*, Vol. 47, No. 3, May 2010, pp. 385–393.

[61] Mandalia, A. B. and Braun, R. D., "High-Altitude Divert Architectures for Future Robotic and Human Mars Missions," *Journal of Spacecraft and Rockets*, Vol. 52, No. 5, Sept. 2015, pp. 1311–1319.

[62] Grenich, A. and Woods, W., "Flow Field Investigation of Atmospheric Braking for High Drag Vehicles with Forward Facing Jets," *Aerospace Sciences Meetings*, American Institute of Aeronautics and Astronautics, Jan. 1981, pp. –.

[63] "NASA, SpaceX Share Data On Supersonic Retropropulsion," *Aviation Week Space Technology*, http://aviationweek.com/space/nasa-spacex-share-data-supersonic-retropropulsion, Oct. 2014.

[64] Christian, J. A., Wells, G., Lafleur, J. M., Verges, A., and Braun, R. D., "Extension of Traditional Entry, Descent, and Landing Technologies for Human Mars Exploration," *Journal of Spacecraft and Rockets*, Vol. 45, No. 1, Jan. 2008, pp. 130–141.

[65] Marsh, C. L. and Braun, R. D., "Fully-Propulsive Mars Atmospheric Transit Strategies for High-Mass Missions," *Journal of Spacecraft and Rockets*, Vol. 48, No. 2, March 2011, pp. 271–282.

[66] Korzun, A. M. and Braun, R. D., "Performance Characterization of Supersonic Retropropulsion for High-Mass Mars Entry Systems," *Journal of Spacecraft and Rockets*, Vol. 47, No. 5, Sept. 2010, pp. 836–848.

[67] Whitlow, W., Blech, R. A., and Blankson, I. M., "Innovative Airbreathing Propulsion Concepts for Access to Space." *Novel Aero Propulsion Systems International Symposium*, Institution of Mechanical Engineers, London, UK, Oct. 2001.

[68] *Airplane Flying Handbook*, U.S. Federal Aviation Administration, Washington D.C., 2004.

[69] Musielak, D. E., "Introduction toHypersonic Air-Breathing Propulsion (HAP),"
Tech. rep., AIAA, July 2015.

[70] Ramsey, R. W., "Research in Hypersonic Airbreathing Propulsion at the NASA
Langley Research Center," *Fifteenth International Symposium on Airbreathing
Engines*, Bangalore, India, Sept. 2001, pp. 1–17.

[71] "Hyper-X at Mach 7," Nov. 2015.

[72] McConnaughey, P. K., Femminineo, M. G., Koelfgen, S. J., Lepsch, R. A., Ryan,
R. M., and Taylor, S. A., "NASA Launch Propulsion Systems Technology Area
Roadmap - TA01," Nov. 2010, pp. 1–32.

[73] Guy, R., Rogers, R., Puster, R., Rock, K., and Diskin, G., "The NASA Langley
Scramjet Test Complex," *32nd Joint Propulsion Conference and Exhibit*, American Institute of Aeronautics and Astronautics, Lake Buena Vista, Florida, July
1996, pp. 1–24.

[74] Kumar, A., Gnoffo, P. A., Moss, J. N., and Drummond, J. P., "Advances
in Computational Capabilities for Hypersonic Flows," Tech. rep., NASA,
Lalaiseau, France, April 1997.

[75] Barthelemy, R., "The National Aero-Space Plane Program," *Maintainablity of
Aerospace Systems Symposium*, American Institute of Aeronautics and Astronautics, Anaheim, California, July 1989, pp. 1–6.

[76] Throckmorton, D., "Enabling Technologies Research and Development for the
National Aero-Space Plane," *National Aerospace Plane Conference*, American
Institute of Aeronautics and Astronautics, Dayton, Ohio, July 1989, pp. 1–6.

[77] McClinton, C., "X-43 - Scramjet Power Breaks the Hypersonic Barrier: Dryden
Lectureship in Research for 2006," *44th AIAA Aerospace Sciences Meeting and
Exhibit*, American Institute of Aeronautics and Astronautics, Reno, Nevada,
Jan. 2006, pp. 1–18.

[78] Engelund, W. C., Holland, S. D., Cockrell, C. E., and Bittner, R. D., "Aerodynamic Database Development for the Hyper-X Airframe-Integrated Scramjet
Propulsion Experiments," *Journal of Spacecraft and Rockets*, Vol. 38, No. 6,
Nov. 2001, pp. 803–810.

[79] Pittman, J. L., Koudelka, J. M., Wright, M. J., and Rock, K. E., "Hypersonics
Project Overview," *Technical Conference*, NASA, Cleveland, Ohio, March 2011,
pp. 1–32.

[80] Rondeau, C. M. and Jorris, T. R., "X-51A Scramjet Demonstrator Program:
Waverider Ground and Flight Test," 2013.

[81] Mutzman, R. and Murphy, S., "X-51 Development: A Chief Engineer's Perspective," *17th AIAA International Space Planes and Hypersonic Systems and Technologies Conference*, April 2011, pp. 1–59.

[82] "X-51A Waverider Fact Sheet," March 2011.

[83] Eklund, D., Baurle, R., and Gruber, M., "Numerical Study of a Scramjet Combustor Fueled by an Aerodynamic Ramp Injector in Dual-Mode Combustion," *39th Aerospace Sciences Meeting and Exhibit*, American Institute of Aeronautics and Astronautics, Reno, Nevada, Jan. 2001, pp. 1–17.

[84] Gicquel, L. Y. M., Givi, P., Jaberi, F. A., and Pope, S. B., "Velocity Filtered Density Function for Large Eddy Simulation of Turbulent Flows," *Physics of Fluids*, Vol. 14, No. 3, March 2002, pp. 1196–18.

[85] Jachimowski, C. J., "An Analytical Study of the Hydrogen-Air Reaction Mechanism With Application to Scramjet Combustion," Tech. Rep. 2791, NASA, 1988.

[86] Lockwood, M., Petley, D., Hunt, J., and Martin, J., "Airbreathing Hypersonic Vehicle Design and Analysis methods," *34th Aerospace Sciences Meeting and Exhibit*, American Institute of Aeronautics and Astronautics, Reno, Nevada, Jan. 1996, pp. 1–15.

[87] Hunt, J. L. and McClinton, C. R., "Scramjet Engine/Airframe Integration Methodology," Vol. 3, No. Sustained Hypersonic Flight, 1997, pp. 1–12.

[88] Shafirovich, E. Y., Shiryaev, A. A., and Goldshleger, U. I., "Magnesium and Carbon Dioxide: A Rocket Propellant for Mars Missions," *Journal of Propulsion and Power*, Vol. 9, No. 2, 1993.

[89] Shafirovich, E. and Varma, A., "Metal-CO2 Propulsion for Mars Missions: Current Status and Opportunities," *Joint Propulsion Conferences*, American Institute of Aeronautics and Astronautics, July 2007, pp. –.

[90] Yuasa, S. and Isoda, H., "Carbon Dioxide Breathing Propulsion for a Mars Airplane," *Joint Propulsion Conferences*, American Institute of Aeronautics and Astronautics, July 1989, pp. –.

[91] King, M. K., "A Simplified Two-Reaction Zone Model of Magnesium Combustion in Carbon Dioxide," *Proceedings of the Combustion Institute*, Vol. 29, 2002, pp. 2931–2938.

[92] Lim, J., Yang, H., and Yoon, W., "Burning and Ignition Characteristics of Single Aluminum and Magnesium Particle," *46th AIAA/ASME/SAE/ASEE Joint Propulsion Conference and Exhibit*, AIAA, American Institute of Aeronautics and Astronautics, Nashville, Tennessee, July 2010, pp. 1–8.

[93] Abbud-Madrid, A., Modak, A., Branch, M. C., and Daily, J. W., "Combustion of Magnesium with Carbon Dioxide and Carbon Monoxide at Low Gravity," *Journal of Propulsion and Power*, Vol. 17, No. 4, June 2001.

[94] Legrand, B., Marion, M., Chauveau, C., Gokalp, I., and Shafirovich, E., "Ignition and Combustion of Levitated Magnesium and Aluminum Particles and Carbon Dioxide," *Combustion Science and Technology*, Vol. 165, No. 1, 2001, pp. 151–174.

[95] Goroshin, S., Higgins, A., and Lee, J., "Powdered Magnesium-Carbon Dioxide Propulsion Concepts for Mars Missions," *Joint Propulsion Conferences*, American Institute of Aeronautics and Astronautics, June 1999, pp. –.

[96] Abbud-Madrid, A., Modak, A., and Branch, M. C., "Combustion of Metals in Reduced Gravity and Extraterrestrial Environments," Tech. Rep. NASA/CP-2003-212376/Rev1, NASA, April 2004.

[97] Wickman, J., "In-situ Mars Rocket and Jet Engines Burning Carbon Dioxide," *Joint Propulsion Conferences*, American Institute of Aeronautics and Astronautics, June 1999, pp. –.

[98] Zubrin, R., Muscatello, T., Birnbaum, B., Caviezel, K., Snyder, G., and Berggren, M., "Progress in Mars ISRU technology," *Aerospace Sciences Meetings*, American Institute of Aeronautics and Astronautics, Jan. 2002, pp. –.

[99] Huff, V. N., Gordon, S., and Morrell, V. E., "General Method and Thermodynamic Tables for Computation of Equilibrium Composition and Temperature of Chemical Reactions," *NACA Report 1037*, Lewis Flight Propulsion Laboratory, National Advisory Committee for Aeronautics, NACA Report 1037, Jan. 1950.

[100] McBride, B. J., Heimel, S., Ehlers, J. G., and Gordon, S., "Thermodynamic Properties to 6000K for 210 Substances Involving the First 18 Elements," *NASA SP-3001*, NASA SP-3001, 1963.

[101] Linnell, J. and Miller, T., "A Preliminary Design of a Magnesium Fueled Martian Ramjet Engine," *Joint Propulsion Conferences*, American Institute of Aeronautics and Astronautics, July 2002, pp. –.

[102] Karlgaard, C., Kutty, P., Shidner, J., Schoenenberger, M., and Munk, M., "Mars Entry Atmospheric Data System Trajectory Reconstruction Algorithms and Flight Results," *Aerospace Sciences Meetings*, American Institute of Aeronautics and Astronautics, Jan. 2013, pp. –.

[103] Benson, T., "Mars Atmosphere Model," June 2014.

[104] Anderson, J. D., *Fundamentals of Aerodynamics (3th ed.)*, McGraw-Hill, New York, NY, 2001.

[105] Van Wylen, G. J. and Sonntag, R. E., "Fundamentals of Classical Thermodynamics," *John Wiley and Sons, Inc.*, 1985, pp. 206–212.

[106] Justus, C. G. and Braun, R. D., "Atmospheric Environments for Entry, Descent and Landing (EDL)," *Fifth International Planetary Probe Workshop*, Bordeaux, France, June 2007.

[107] Candler, G., "Computation of Thermo-Chemical Nonequilibrium Martian Atmospheric Entry Flows," *Fluid Dynamics and Co-located Conferences*, American Institute of Aeronautics and Astronautics, June 1990, pp. –.

[108] Burkhardt, H., Sippel, M., Herbertz, A., and Klevanski, J., "Comparative Study of Kerosene and Methane Propellant Engines for Reusable Liquid Booster Stages," *Proceedings of the Fourth International Conference on Launcher Technology*, Liège, Belgium, Dec. 2002.

[109] Yuasa, S., Sakoda, K., and Fukuchi, A., "An Examination on Some Technical Problems of a CO2-Breathing Turbojet Engine in the Mars Atmosphere," *Joint Propulsion Conferences*, American Institute of Aeronautics and Astronautics, July 2000, pp. –.

[110] JPL, N., "Guided Entry - Mars Science Laboratory," .

[111] Striepe, S. A., Powell, R. W., Desai, P. N., Queen, E. M., Way, D. W., Prince, J. L., Cianciolo, A. M., Davis, J. L., Litton, D. K., Maddock, R. M., Shidner, J. D., Winski, R. G., OKeefe, S. A., Bowes, A. G., Aguierre, J. T., Garrison, C. A., Hoffman, J. A., Olds, A. D., Dutta, S., Brauer, G. L., Engel, M. C., and Marsh, S. M., *Program To Optimize Simulated Trajectories II (POST2)*, NASA Langley Research Cenger, Lockheed Martin Corporation, 31st ed., June 2014.

[112] Lafleur, J. and Cerimele, C., "Angle of Attack Modulation for Mars Entry Terminal State Optimization," *AIAA Atmospheric Flight Mechanics Conference*, American Institute of Aeronautics and Astronautics, Aug. 2009, pp. 1–20.

[113] Lafleur, J. M. and Cerimele, C. J., "Mars Entry Bank Profile Design for Terminal State Optimization," *Journal of Spacecraft and Rockets*, Vol. 48, No. 6, Nov. 2011, pp. 1012–1024.

[114] Wolf, A. A., Tooley, J., Ploen, S., Ivanov, M., Acikmese, B., and Gromov, K., "Performance Trades for Mars Pinpoint Landing," *IEEE Aerospace Conference*, IEEE, Jan. 2006, pp. 1–16.

[115] Laub, B. and Venkatapathy, E., "Thermal Protection System Technology and Facility Needs for Demanding Future Planetary Missions," *International Workshop on Planetary Probe Atmospheric Entry and Descent Trajectory Analysis and Science*, Oct. 2003, pp. 1–9.

[116] Stechman, R. and Allen, R., "History of Ramjet Propulsion Development at the Marquardt Company - 1944 to 1970," *41st AIAA/ASME/SAE/ASEE Joint Propulsion Conference & Exhibit*, American Institute of Aeronautics and Astronautics, Reston, Virigina, June 2012, pp. 1–16.

[117] The Marquardt Corporation Aerojet - General Corporation, "SERJ Subscale Phase 1 Test Program," Tech. rep., The Marquardt Corporation Aerojet - General Corporation, June 1968.